TEMPOROSPATIAL PRECISION OF INTEGRIN RESPONSE TO FIBRONECTIN MATRIKINE: UNVEILING AN OSTEOARTHRITIS-PERPETUATING PATHWAY

Michael Zhe Miao

A dissertation submitted to the faculty at the University of North Carolina at Chapel Hill
in partial fulfillment of the requirements for the degree of Doctor of Philosophy in
Oral and Craniofacial Biomedicine, Adams School of Dentistry

Chapel Hill
2023

Approved by:

William Arendshorst

Roland Arnold

Edward Bahnson

Brian Diekman

Richard Loeser

ABSTRACT

Michael Zhe Miao: Temporospatial precision of integrin response to fibronectin matrikine:
unveiling an osteoarthritis-perpetuating pathway
(Under the direction of Richard F. Loeser)

Integrin endocytosis plays a pivotal role in intracellular signaling, yet its involvement in the remodeling of damaged extracellular matrix remains poorly understood. Matrikines, which are bioactive protein fragments resulting from the degradation of the extracellular matrix, are key contributors to various degenerative diseases, including osteoarthritis.

In the context of osteoarthritis, fibronectin, an extracellular matrix protein, assumes a significant role as it is upregulated in osteoarthritis tissue and subsequently targeted for degradation by several proteases. This proteolytic activity leads to the generation of fibronectin fragments of various sizes. Notably, these fibronectin fragments, including those containing the Arg-Gly-Asp (RGD) attachment site, activate catabolic signaling pathways, resulting in the release of proteases, as well as cytokines and chemokines associated with the innate immune system. Given the limited repair capacity of cartilage, the presence of matrix degradation products such as fibronectin matrikines can fuel a destructive cycle of progressive matrix degradation and joint tissue inflammation, culminating in structural changes accompanied by symptoms of pain and loss of function.

Our research has provided insights into the internalization of a specific fibronectin matrix protein fragment (FN7-10) along with α5β1 integrin by articular chondrocytes, which triggers the formation of signaling redoxosomes. Through a precisely orchestrated temporal and spatial

mechanism, redoxosome formation and the generation of hydrogen peroxide by NADPH oxidase 2 (Nox2) regulate the activation of MAP kinases, subsequently triggering the production of matrix metalloproteinase-13. The redox-regulated tyrosine kinase Src colocalizes with α5 integrin at the Nox2-containing redoxosomes. Furthermore, in vivo studies using human osteoarthritic cartilage have demonstrated the formation of redoxosomes during osteoarthritis pathogenesis, capable of transmitting and sustaining redox signaling that promotes further matrix damage. Consequently, α5β1 integrin signaling, initiated by a fibronectin matrikine, is facilitated by redoxosome formation, perpetuating a self-amplifying cycle of matrix degradation.

By unraveling the intricacies of integrin response and redoxosome formation in a precise temporal and spatial manner, this research provides support for the development of novel therapies for osteoarthritis that specifically target signaling pathways with subcellular precision. Such targeted interventions hold promise for addressing the destructive matrix degradation observed in OA and potentially other related degenerative conditions.

“To teach is to learn twice.”

- Joseph Joubert

“The only time you must not fail is the last time you try.”

- Phil Knight

ACKNOWLEDGEMENTS

To Dr. Richard F. Loeser, I want to express my profound gratitude for the unwavering support you have provided me throughout my journey as your student. Having you as my mentor during my graduate school experience has been an immense privilege. Your impact on each individual mentee has been nothing short of remarkable. The wisdom and guidance you consistently offer have proven invaluable, and I am determined to carry these lessons with me as I embark on my professional career. One lesson stands out among the many invaluable teachings I have received from you—the significance of maintaining an open-door policy and fostering a culture that encourages individuals to challenge their boundaries and take more initiatives. Your creation of an environment that thrives on pushing boundaries and surpassing limitations has been truly inspiring. The collective dedication to excellence and the relentless pursuit of knowledge in your lab have fueled my ambition and instilled in me the belief that I can genuinely make a difference in our field. I sincerely appreciate the countless hours you have devoted to reviewing my work, providing constructive feedback, and offering valuable insights. Your mentorship has not only impacted my academic journey but has also paved the way for my future career in research. Your unwavering support has instilled in me the confidence to explore new avenues of knowledge and has fueled my passion for scientific discovery.

I am also compelled to extend my gratitude to the remarkable individuals who make up the Loeser lab. Kathryn Kelly, Yang Cui, John Collins, Mary Zhao, Phillip Coryell, Jes Bolduc, Michael Cunningham, Kim Mix, Scott Wood, Veronica Ulici, Earnest Taylor, and Priya Gopalakrishnan – you all contributed immeasurably to the vibrant atmosphere of our lab. Not only have you witnessed my personal growth, but you have also been instrumental in the progress of my projects. Your encouragement has played an essential role in shaping me as a physician-scientist.

I would like to express my deepest gratitude to the members of my dissertation committee, Drs. Edward M. Bahnson, Roland Arnold, William Arendshorst, and Brian Diekman. I am truly grateful for your support and commitment throughout my dissertation journey. In particular, I want to acknowledge Dr. Bahnson for chairing the committee and providing exceptional guidance. Your collective dedication, sacrifice of time, and generous contribution of your talents have been instrumental in shaping the trajectory of my research. Your expertise and mentorship have played a pivotal role in my development, enabling me to acquire a strong foundation of knowledge and essential research skills. Your guidance has allowed me to focus my efforts and make significant breakthroughs in my work. I am indebted to you for your contributions.

My thesis project cannot be completed without the invaluable collaborations from individuals worldwide who generously shared their knowledge, pinpointed the direction I should delve into, and provided numerous solutions during our wonderful brainstorming sessions. These collaborations have allowed me to continuously push my own limits and strive for greater achievements. I would like to extend my heartfelt gratitude to several individuals who have played a pivotal role in this process, in particular Drs. Qian Peter Su, Menglin Wang, Pablo Ariel, Di Wu, and Leaf Huang for their exceptional contributions and guidance. Additionally, I would like to acknowledge the numerous others who have contributed to this project, although space does not permit me to mention each name individually.

It is a true honor for me to pursue my doctoral study at the University of North Carolina at Chapel Hill, home to a world-renowned dental school. The unique opportunities I have encountered at this institution are unparalleled and cannot be replicated elsewhere. The knowledge and skills I have acquired during my time in graduate school have prepared me to embark on a transformative journey aimed at leading positive change in society and addressing some of the world's most pressing challenges. I want to thank Dr. Christopher Fox for providing me with the opportunity to pursue my PhD studies in a manner that deviates from the traditional path, allowing me to explore new avenues in my academic journey beyond my clinical dentistry training. Dr. Ronald Strauss, who has been a steadfast supporter and observer of my growth and development, deserves my heartfelt appreciation for his encouragement as I stretched myself beyond my comfort zone, forging my own unique path in my chosen career. Your continuous presence and mentorship have played a pivotal role in shaping the person and professional I have become. I also want to thank faculty, friends, and students that I met at the OCBM program, including Dr. Ceib Phillips, Dr. Eric Everett, and Dr. Roland Arnold (who also served on my doctoral committee), as well as numerous others. Your presence and influence have had a profound impact on my life, molding me into the individual I am today as I embark on this transformative doctoral journey.

I would like to express my heartfelt gratitude for the support, guidance, and mentorship provided by Dr. Kenneth M. Yamada. As a junior apprentice, I could only dream of engaging with someone of your caliber, whose research papers on integrin and fibronectin, two of your favorite molecules, have been instrumental in shaping not only my knowledge but people working in the area worldwide. I consider myself incredibly fortunate to have had the opportunity to discuss my thesis project with you. Your expertise and insights have been instrumental in refining our research and taking it to a more impactful level. Your trust in me in person and your continued willingness to mentor me at the NIH/NIDCR are incredibly meaningful to me. I am grateful for the opportunity to learn from you and further develop my career under your guidance.

I want to thank my parents for their understanding and support in encouraging me to fearlessly explore my own path in life and my career. Their belief in me has been a driving force behind my achievements. To my past advisors and schoolteachers, I am truly grateful for your constant involvement in my educational and professional journey. Whenever I sought assistance, you were always there, ready to provide guidance and support. A special thank you goes to Dr. Jared M. Lowe for accompanying me throughout my PhD journey and beyond. Your presence and support have been invaluable to me. I would also like to extend my appreciation to the Lowe family for embracing me as one of their own, treating me with such warmth and kindness. Additionally, I am grateful to my loyal companion, Rowdy, a chocolate Labrador retriever, whose companionship and support have brought immense joy and comfort to my life. To my friends at Chapel Hill and my wonderful neighbors in the WoodGlen community, thank you for making my journey so much more vibrant and fulfilling.

We must acknowledge that in a world where a significant portion of the population lacks access to comprehensive scientific education, there remains a pressing responsibility to impart knowledge to our current generation and those who will succeed it.

TABLE OF CONTENTS

LIST OF FIGURES

LIST OF ABBREVIATIONS

ADAMTS	a disintegrin and metalloproteinase with a thrombospondin motif
ANGPTL	angiopoietin-like protein
ANOVA	analysis of variance
AP-1	activator protein 1
cCAT	cyctosolic catalase
COX	cyclooxygenase
DMARD	disease-modifying antirheumatic drug
DMEM	Dulbecco's modified Eagle's medium
ECM	extracellular matrix
EGFP	enhanced green fluorescent protein
ERK	extracellular signal-regulated kinase
FAK	focal adhesion kinase
FBS	fetal bovine serum
FN	fibronectin
FN7-10	fibronectin fragment having sequence of type III repeats 7-10
FN-f	fibronectin fragment (general)
GTPase	guanosine triphosphatase
JNK	c-Jun N-terminal kinase
IGF	insulin-like growth factor
IL	interleukin
MAP	mitogen-activated protein
mCAT	mitochondrial-targeted catalase
MMP	matrix metalloproteinase
MWCO	molecular-weight cut off
NF-kB	nuclear factor kappa B
Nox	NADPH oxidase
NO	nitric oxide
n.s.	not significant
NSAID	nonsteroidal anti-inflammatory drug

OA	osteoarthritis
OD	optical density
PBS	phosphate-buffered saline
PCM	pericellular matrix
PGE	prostaglandin E
PKCδ	protein kinase C delta
PRX	peroxiredoxin
PTM	posttranslational modification
PTP	protein tyrosine phosphatase
RA	rheumatoid arthritis
RGD	arginine-glycine-asparagine
ROI	regions of interest
ROS	reactive oxygen species
SDS-PAGE	sodium dodecyl sulfate-polyacrylamide gel electrophoresis
s.e.m.	standard error of the mean
SF	synovial fluid
SOX	Sry-related HMG box
Src	sarcoma, a proto-oncogene tyrosine-protein kinase
TBP	TATA-box binding protein
µg/mL	micrograms per mililiter
µm	micrometer
µM	micromolar

1. CHAPTER 1: INTRODUCTION

1.1. The Growing Burden of Osteoarthritis

Osteoarthritis (OA) stands as the leading joint disorder in the United States, affecting a significant portion of the population, particularly individuals aged 60 and older, with a prevalence of approximately 10% in men and 13% in women.(*1*) The combination of an aging population and the obesity epidemic is anticipated to contribute to a further increase in the number of individuals experiencing symptomatic OA. The high prevalence of OA, notably in major joints like the knee and hip, results in substantial difficulties in performing everyday activities such as walking and climbing stairs, rendering it the primary cause of disability. As the prevalence continues to rise, OA is projected to have an increasingly significant impact on both healthcare and public health systems. By the year 2030, it is estimated that the population of individuals aged 65 and older in the United States will reach a staggering 74 million, accounting for almost 21% of the total population. This demographic shift raises concerns regarding the potential consequences of disability within the US population.(*2*, *3*) Unfortunately, despite its considerable impact, OA often remains overlooked in global health plans, and there is a lack of effective treatments and appropriate care.(*4*) The management of OA can vary greatly, and patients often feel that their needs and concerns are not adequately addressed. Addressing these challenges requires a fresh approach that emphasizes prevention, reduces inappropriate care, improves access to effective interventions, and explores affordable and safe options for pain relief.

1.1.1. Clinical Signs

Pathologic changes in OA joints are marked by gradual degeneration and depletion of the articular cartilage, thickening of the underlying subchondral bone, the emergence of osteophytes, varying degrees of synovial inflammation, deterioration of ligaments and menisci in the knee, and enlargement of the joint capsule.(*5*) Clinical signs often include joint instability, persistent pain, stiffness, and narrowing of the joint space observed in radiographic images. Long-term ramifications of knee OA encompass decreased physical activity, loss of fitness, disrupted sleep, fatigue, depression, decline in function, and disability.(*3*) Interestingly, structural alterations consistent with OA can be found in asymptomatic individuals, and the factors influencing the association between disease severity and reported levels of pain and disability remain unclear.(*6*)

Pain within the joints is a typical presentation of OA. In a one-year study, it was found that 25% of individuals aged over 55 in the United Kingdom and the Netherlands experienced persistent knee pain, with 15% of them seeking medical consultation.(*7*) Only 50% of those individuals had radiographic evidence of knee OA. Plain radiographs, such as X-rays, are more useful in ruling out other diagnoses rather than confirming OA, as they typically confirm severe cases.(*8*) Advanced imaging techniques like magnetic resonance imaging (MRI) are more effective in detecting degenerative changes at an earlier stage. The precise factors that distinguish symptomatic OA from asymptomatic radiographic manifestations are still largely unclear. Around 12% of individuals aged 55 and above experience symptomatic knee OA, characterized by frequent pain and radiographic evidence of OA.(*7*)

Symptomatic joint pain in OA is typically aggravated by activity and relieved by rest. Advanced stages of OA can cause pain even at rest and during the night, leading to sleep disturbances that further exacerbate pain. The pain is often deep, aching, and diffuse, indicating an insidious onset. Other symptoms include reduced joint function, brief stiffness after periods of inactivity (referred to as "gelling"), and joint instability, such as buckling or giving way. Patients may also report joint deformity, swelling without systemic features like fever, crepitus, age-related discomfort, and persistent pain-related psychological distress.(*6*, *9*)

1.1.2. Osteoarthritis Burden and Current Therapy

Current healthcare approaches for OA frequently differ in their approaches, ranging from addressing underlying deficiencies like physical activity, shedding weight, and education, to employing expensive and unverified therapies during the later phases of the ailment. Regrettably, patients often lack awareness regarding the available treatment alternatives.(*4*) These divergent therapeutic choices are frequently provided in a disjointed manner, failing to tackle the multifaceted nature of OA and its accompanying conditions. Consequently, unintended repercussions can emerge, such as the inappropriate use of opioid analgesics. In contrast to rheumatoid arthritis (RA), where disease-modifying antirheumatic drugs (DMARDs) have transformed treatment, the therapeutic landscape for OA predominantly concentrates on pain management, as there is presently no authorized agent for preventing or treating disease progression.(*10*) In an ideal scenario, the management of OA should aim to modify the trajectory of disease advancement and avert long-term disability, but current endeavors primarily focus on patients in advanced stages of the condition.(*11*) At present, besides pain management and surgical intervention in severe instances, effective therapeutic remedies for OA are lacking.(*5*)

1.1.3. Evidence for Development of Disease Modifying Therapies for Osteoarthritis

The available treatment options for knee OA become limited when patients are unable to tolerate nonsteroidal anti-inflammatory drugs (NSAIDs), and uncertainty arises regarding suitable medications. Furthermore, there are currently no approved drugs specifically designated as disease-modifying agents for OA.(*3*) Promising data from randomized, phase 2 trials have indicated potential improvements in joint cartilage thickness over a two-year period with the use of a recombinant human fibroblast growth factor 18 or a cathepsin K inhibitor. However, the clinical significance of these changes remains unclear, necessitating further data and research.(*12*, *13*) While early-stage knee OA may present a valuable "window of opportunity" to intervene and restore joint homeostasis, in-depth studies on the cellular and molecular processes that initiate early disease are required. Moreover, these processes need to be linked to specific triggering events based on the individual patient's profile to gain a comprehensive understanding.(*11*)

1.1.4. Cartilage Loss and Initiation of Osteoarthritis

Chondrocytes, comprising only 1-2% of total cartilage volume, are the sole cell type in cartilage. While cartilage degradation is a central aspect of OA, it is now widely recognized that other joint structures are also affected, including meniscal fibrocartilage, hyaline articular cartilage, subchondral bone, and synovium. The byproducts of cartilage breakdown are detected in synovial fluid, and microfissures emerge prior to detectable degeneration in MRI imaging or arthroscopy.(*14*) The degradation of articular cartilage is driven by well-understood mechanisms involving cartilage matrix catabolic effects, such as metalloproteinases (MMPs) and aggrecanases, as well as anti-anabolic effects mediated by chondrocytes, including increased production of reactive oxygen species or free radicals.(*15*)

OA is a complex condition characterized by abnormal changes in joint tissues, triggered by various inflammatory mediators within the affected joint. While regular wear and tear can contribute, it is important to note that OA is not solely caused by this factor. Several risk factors increase the likelihood of developing OA. Despite the intricate nature of OA, there are common pathological changes observed in osteoarthritic joints. These changes have a significant impact on joint structure, resulting in pain, deformity, and limitations in function.

In OA, the extracellular matrix of the cartilage undergoes pathological alterations. This includes the degradation of crucial components like type II collagen and proteoglycans, loss of tissue hydration, and the production of abnormal fibrous matrix. These changes occur alongside abnormal chondrocyte proliferation, senescence, inflammation, and hypertrophy. Similarly, the remodeling processes in the subchondral bone are dysregulated, leading to alterations in cortical plate thickness and local trabecular bone mass and architecture. The severity of these changes depends on the progression of OA and can be accompanied by the development of osteophytes (bony outgrowths) at the joint margins. However, the exact temporal relationship between bone and cartilage tissue phenomena remains unclear from a pathophysiological perspective.(*16*)

The exact initiation site of the osteoarthritic process, whether in articular cartilage, calcified cartilage, or subchondral bone, is still uncertain.(*17*) Studies have shown a significant association between the loss of cartilage thickness and a slight worsening of pain over a 24-month period. This association between cartilage thickness loss and pain is mediated by changes in synovitis rather than bone marrow lesions. Radiographic evidence of joint damage may indicate the potential for joint pain, but it is evident that the extent of joint damage observed in radiographs does not necessarily correlate with the severity of pain experienced.(*6*)

Extensive population-based studies have provided compelling evidence suggesting that radiographic abnormalities often appear without accompanying pain.(*18*) However, it is important to acknowledge that pain-sensitive aspects within the joint may not be detectable through X-ray imaging. Furthermore, incidental findings of early osteochondral defects and meniscal tears have been identified in middle-aged and elderly individuals through MRI scans, despite the absence of knee pain or related symptoms. These findings emphasize the concept that initial osteoarthritic changes can go unnoticed, with pain, stiffness, and discomfort emerging at a later stage when the pathological progression of OA has significantly advanced.(*19*)

Data obtained from cutting-edge imaging methodologies and firsthand arthroscopic scrutiny substantiate the existence of minor inflammatory activity within OA joints prior to the manifestation of noticeable radiographic alterations.(*10*) This suggests that OA constitutes an inflammatory ailment, even during its initial phases, preceding observable indications of cartilage deterioration. A research investigation employing consecutive arthroscopies on knees afflicted by symptomatic yet pre-radiographic OA unveiled a definitive association between the occurrence of synovitis and subsequent medial cartilage decline.(*20*) These discoveries underscore the significance of inflammation in the advancement of OA and its influence on joint well-being.

1.2. Extracellular Matrix Remodeling in Osteoarthritis

The constant remodeling of the extracellular matrix (ECM) in cartilage is a key feature that drives the OA development. Imbalances in ECM production not only worsen OA but also establish a self-perpetuating cycle of cartilage degeneration.(*21*) To target potential OA treatments, it is essential to understand the key players in the ECM and their interactions with chondrocytes.

In healthy cartilage, the ECM mainly consists of collagen type II, providing tensile support, and aggrecan, a proteoglycan that attracts water and imparts compressive strength.(*22*) Aggrecans fill the spaces within collagen fibrils, forming a network with hyaluronan and link proteins. Aggrecan monomers consist of a core protein attached to chondroitin sulfate and keratan sulfate glycosaminoglycans.(*23*)

However, in OA, an intriguing transformation occurs within the matrix components, characterized by the degradation of collagen type II and aggrecan. This change sets the stage for mechanical issues in cartilage and puts stress on chondrocytes,(*24*, *25*) leading to the formation of chondrocyte clusters.(*22*) Additionally, during OA onset, collagen production shifts from type II to type I, typically found in subchondral bone. Collagen type I has fewer crucial residues for collagen type II and aggrecan interaction, contributing to cartilage fibrillation and lesion development.(*26*) Other ECM components, like Tenascin-C, increase in OA and induce inflammatory mediators, collectively contributing to stiffness in articular cartilage.(*27*) The loss of aggrecan and changes in collagen composition lead to thinner and stiffer cartilage, transmitting increased loads to subchondral bones, contributing to the development of periarticular osteophytes and subchondral bone cysts.(*28*, *29*)

OA is characterized by pathological remodeling of cartilage, involving an imbalance between destructive and constructive processes. Chondrocytes in OA attempt to synthesize matrix components while expressing higher levels of proteases, resulting in greater matrix degradation than deposition.(*30*, *31*) This leads to decreased proteoglycan content and collagen cleavage. As a result, the degraded cartilage ECM releases fragmented ECM proteins, referred to as "bioactive peptides" or "matrikines," into the synovial fluid (SF).(*32*, *33*) These processed ECM components and matrikines can bind to receptors present on various cell types in the joint tissues, including cartilage, the synovial membrane, and the intrapatellar fat pad.(*34*)

The pericellular matrix (PCM) plays a critical role in supporting the metabolic activity of chondrocytes by acting as a mediator or filter for biochemical and biomechanical signals. It consists primarily of type VI collagen, fibronectin, perlecan, and biglycan. In OA, changes occur in the distribution of collagen and proteoglycans within the PCM even before chondrocyte proliferation and cluster formation take place. The cartilage affected by OA shows signs of PCM swelling, loosely organized PCM structures, and elongated cytoplasmic processes of chondrocytes extending into the territorial matrix. Recent research has shed light on the early degradation of the PCM surrounding chondrocytes in OA, highlighting its significance in the development of the disease.(*35*)

Fibronectin is a critical component of the PCM, necessary for its assembly and regulation of cellular functions. In OA, proteases cleave fibronectin, exposing previously concealed sites within matrix proteins called matricryptins.(*32*, *33*) These fibronectin matrikines have been detected in the synovial fluid and cartilage of OA patients.(*36*) Experimental introduction of matrix fragments into joints has been demonstrated to induce cartilage damage.(*37*) Furthermore, treating isolated femoral chondrocytes with fibronectin fragments replicates several characteristics of the OA phenotype.(*38*) Several downstream signaling molecules associated with α5β1 integrin, such as MAP kinases, ROS, Rac1, PKCδ, and Src, have been identified. Treating chondrocytes with fibronectin matrikines has been shown to increase S-sulfenylation levels, including that of Src, and enhance Src activity.(*39*) Activation of PKCδ can trigger the activation of NF-kB and MAPK pathways.(*40*) MAP kinase activation inhibits anabolic signaling, suppresses the production of proteoglycans (PGs), and upregulates the expression of catabolic proteases like MMP-3 and MMP-13. Notably, MMP-13 generates additional matrikines,(*41*) thus perpetuating the destructive cycle of cartilage.

The precise mechanisms that initiate OA remain unclear, and it is likely that multiple factors contribute to its pathogenesis. However, it has been observed that matrikines trigger a pro-catabolic response in arthritic joints, and this process is mediated by integrins. Exploring the role of fibronectin matrikines in OA pathogenesis provides valuable insights into potential therapeutic targets. By targeting the degradation and pro-inflammatory responses caused by these fragments, it is possible to mitigate cartilage degradation and alleviate the symptoms of this debilitating condition.(*42*)

1.3. Osteoarthritis Pathogenesis at the Cellular Level: Focus on Integrin Receptors

Integrins, essential for cell-cell and cell-matrix interactions, are the subject of intensive investigation regarding their role in OA pathogenesis.(*43*) These transmembrane receptors mediate cell adhesion, signaling, and tissue remodeling. Dysregulated expression, activation, and signaling of integrins have been observed in various joint tissues affected by OA, including articular cartilage, subchondral bone, synovium, and ligaments.(*44*) Alterations in integrin function can influence cell behavior, such as chondrocyte metabolism, cartilage homeostasis, and matrix synthesis. Signaling pathways mediated by integrins play a critical role in initiating the catabolic reactions that contribute to joint destruction in OA. Abnormal expression of integrins in OA disrupts the balance of destructive cytokines, while inadequate inhibition of MMP-13, the primary enzymes involved in ECM breakdown, further exacerbates the disease.(*45*)

Integrins exhibit a unique structural composition consisting of two subunits, namely alpha and beta. Within this protein family, there are eighteen alpha subunits and eight beta subunits, which can combine in various configurations to generate twenty-four distinct integrin receptors.(*46*) These integrin receptors can be broadly classified into two groups: Arg-Gly-Asp (RGD)-binding receptors and non-RGD-binding receptors. The non-RGD-binding receptors encompass collagen-binding receptors, laminin-binding receptors, and leukocyte-binding receptors.(*47*, *48*) Functioning as transmembrane proteins, integrins play a critical role in facilitating a wide range of physiological processes within cells. One of their primary functions is mediating adhesion at the interface between the cytoskeleton and the ECM. Through interactions with intracellular proteins such as α-actinin, vinculin, and paxillin, integrins establish connections between the internal cytoskeleton and the ECM, enabling cellular adhesion and signaling.(*49*)

Chondrocytes exhibit a diverse repertoire of integrin protein families, such as α5β1, α1β1, α2β1, α10β, α6β1, αVβ3, and numerous others, allowing them to establish connections with a wide range of cartilage ECM proteins.(*50*) The intricate interactions between integrins and their extracellular ligands underscore the pivotal role of integrins in facilitating chondrocyte adhesion. Adhesion takes place when integrins bind to non-collagenous fibrils, forming elaborate adhesion structures.(*51*)

Mechanical stress experienced by joints plays a pivotal role in influencing and regulating the activity of chondrocytes in vivo.(*52*) Chondrocytes possess mechanisms to respond to mechanical stresses in two ways: "directly" by detecting deformation of the pericellular matrix (PCM) through adhesions with the ECM and sensory structures within the cell, and "indirectly" by responding to growth factors released in response to mechanical stimulation, which interact with cell receptors.(*16*) Integrins, serving as important mechanoreceptors, also possess the capability to influence the physiological functions of chondrocytes through the initiation of the mechanosignal pathway, known as mechanotransduction.(*53*, *54*) It has been demonstrated that mechanical loading induces α5β1-mediated membrane hyperpolarization, which is activated by protein kinase C and the release of IL-4. Additionally, integrin-mediated FAK and Src signaling have been implicated in cell death caused by impact loading.(*55*)

Periodic biomechanical loading has been found to effectively stimulate the connection between fibronectin and integrin α5β1.(*56*) The interaction between fibronectin matrix fragments and α5β1 integrin triggers the expression of inflammatory cytokines and MMPs.(*57*, *58*) As a result, the balance between the anabolic and catabolic activities of chondrocytes is disrupted. Fibronectin matrikines are formed when MMPs degrade fibronectin, and these matrikines possess catabolic properties. Notably, matrikines containing the RGD motif exhibit the highest affinity for binding to α5β1 integrin.(*37*) Exposure to fibronectin matrikines, RGD-containing peptides, or α5β1 antibodies can induce a catabolic response, while intact fibronectin does not elicit such a response.(*59–62*)

α5 integrin is recognized for its potential to provide protective effects by inhibiting hypertrophy, the progression of OA, and chondrocyte dysfunction. Extensive research conducted thus far, including in vivo preclinical studies and recent clinical trials, has demonstrated promising outcomes in targeting α5 integrin as a druggable and targetable approach. Studies conducted on an OA rat model induced by surgery have demonstrated diminished expression of integrin α5 in chondrocytes compared to a normal group. This suggests that alterations in the ECM have the potential to disrupt cartilage homeostasis, impede chondrocyte repair capability, and exacerbate OA-related pathological changes.(*63*, *64*) Antibodies blocking integrins have been employed to study integrin-ECM interactions. Studies using these antibodies to block individual subunits or specifically α5β1 in chondrocytes from chicks and mice have demonstrated reduced survival and differentiation. Dedifferentiation has also been observed in adult chondrocytes when α5β1 antibodies are used.(*43*) Germline knockout studies in mice targeting the α10, α5, or β1 subunits have provided valuable insights into their role, uncovering a variety of abnormalities such as disorganized growth plates and early embryonic lethality.(*65*)

However, recent research employing conditional knockout of α5 integrin specifically in mouse synovial joints has shed new light on its function. Surprisingly, this study revealed normal development in the absence of α5 integrin, and upon surgical induction of OA in mutant mice, a remarkable reduction in cartilage matrix loss was observed, indicating a potential therapeutic avenue.(*66*) In a recent groundbreaking study, a first-in-human phase 1 trial was conducted to evaluate the efficacy of LNA043—a derivative of angiopoietin-like 3 (ANGPTL3)—as a potential disease-modifying drug candidate for OA. LNA043 has demonstrated the ability to regenerate hyaline articular cartilage, a key characteristic of healthy cartilage, in vivo.(*67*) This regenerative effect is believed to be mediated through the binding of LNA043 to the α5β1 integrin. These findings hold significant promise for the development of novel disease-modifying treatment for OA targeting integrin α5.

It is worth mentioning that research has revealed an elevated expression of αvβ3 integrin has been noted in an in vitro OA model resulting from excessive mechanical stress, which leads to phosphorylation of downstream signaling molecules, including FAK and ERK. Inhibiting αvβ3 integrin has shown reduction in catabolic processes, both in vitro and in vivo.(*68*, *69*) Interestingly, studies have indicated that stimulating αvβ3 integrin in the presence of α5β1 antibodies can effectively suppress the production of inflammatory markers such as IL-1β, nitric oxide (NO), and PGE2.(*70*)

Considering the detrimental consequences of targeting specific integrins or integrin subunits, which not only affect cartilage but also overall survival, therapeutic strategies in this area are challenging and require further exploration.(*71*) Therefore, it becomes essential to advance our understanding of the signaling pathways that occur downstream of integrins. This pursuit aims to uncover new targets that have the potential to disrupt the self-perpetuating cycle of cartilage degradation and introduce innovative approaches for the treatment of OA.(*72*)

1.4. Intricacies of Redox Signaling

Posttranslational modifications (PTMs) play a vital role in regulating a wide range of cellular processes, increasing the diversity of the proteome, and influencing protein structure and function. One important aspect of PTMs is their involvement in bidirectional signaling across integrins, which is essential for effective cellular communication. Protein phosphorylation is a common PTM that modulates integrin-mediated signaling. However, recent studies have shown that integrin activation can also trigger the production of reactive oxygen species (ROS),[1] resulting in redox-dependent modifications that significantly impact cell signaling responses.(*73*, *74*)

ROS encompass a variety of molecules, including reactive radicals like superoxide and nonradical species such as hydrogen peroxide (H_2O_2). While ROS are often associated with cellular damage, emerging evidence highlights their central role in determining cell fate and modifying signaling molecules. Among ROS, H_2O_2 is particularly interesting due to its nonradical nature, lower reactivity, and stability. Its small size enables it to travel extended distances within cells and between cells, making it an effective messenger molecule in cellular signaling.(*75*)

The primary mechanism by which H_2O_2 functions as a messenger molecule involves the reversible oxidation of specific cysteine (Cys) residues. Cysteine residues contain highly reactive thiol groups (Cys-SH) that are susceptible to oxidation. This oxidation process plays a crucial role in modulating signaling pathways, particularly at low concentrations of H_2O_2.(*76*)

One important target of H_2O_2-mediated oxidation is the redox-sensitive cysteine residues present in protein tyrosine phosphatases (PTPs). These cysteine residues are located within the catalytic sites of all PTPs and their oxidation results in the inhibition of phosphatase activity.(*77*) This inhibition leads to prolonged and intensified signaling, particularly in tyrosine kinase

---

[1] The term 'ROS' (Reactive Oxygen Species), although widely used, lacks specificity in identifying the actual chemical species involved in biological processes. In this thesis, our objective is to provide precise descriptions of known measurable or specific chemical species associated with biological processes to the fullest extent possible.

signaling cascades, enabling precise modulation of cellular responses. Redox-sensitive cysteine residues can also be found in signaling molecules like transcription factors, including NF-κB and AP-1, within the context of OA pathogenesis.(*78*) The oxidation of these cysteine residues profoundly impacts protein function, activity, or localization, further influencing cellular signaling processes.(*73*, *79*, *80*)

Despite these important findings, a fundamental and persistent question arises regarding the competition between peroxiredoxins (PRXs) and PTPs in redox biology. PRXs exhibit significantly faster reaction rates with H_2O_2 compared to PTPs.(*81*) This raises the intriguing mystery of how H_2O_2 effectively acts upon less reactive targets within PTPs, even in the presence of other competitive agents. The underlying mechanisms of this phenomenon remain to be elucidated in the field of redox biology.(*81–83*)

Maintaining a dynamic equilibrium of cellular ROS levels is crucial under normal physiological conditions. Processes that generate and eliminate ROS tightly regulate this equilibrium. ROS can be generated as byproducts or waste products of essential reactions in biological processes such as mitochondrial oxidative metabolism. They can also be intentionally generated in response to xenobiotics, cytokines, and bacterial invasion as part of signal transduction pathways or cell defense mechanisms.(*84*, *85*)

Differentiating between pathological oxidative signaling and normal physiological signaling mediated by H_2O_2 can be challenging due to their involvement in a wide range of cellular processes. However, recent studies have directed their focus towards localized imbalances in cellular redox state and their potential implications for pathological signaling. This challenges the conventional notion of oxidative stress as a phenomenon that uniformly affects entire cells or tissues.(*86*) Consequently, it has become imperative to identify specific molecular targets that govern redox circuits within cells and gain insights into the compartmentalization of enzymes responsible for ROS generation and degradation. Understanding these regulatory mechanisms is fundamental for comprehending the broader consequences that arise from inhibiting ROS sources, particularly when considering targeted therapies aimed at modulating ROS levels.(*87*)

Furthermore, it is important to acknowledge that the activation of integrins by various stimuli triggers ROS generation, but the underlying mechanism, including the temporal and spatial patterns, is heavily influenced by the specific tissue context. For instance, in chondrocytes during the development of OA, although we now know that the activation of integrin in chondrocytes leads to ROS generation, the precise mechanisms governing ROS generation and regulation in response to integrin activation remain elusive. Unraveling these intricacies and enhancing our understanding of the complex interplay involved is a pressing need, especially within the realm of OA pathogenesis.(*78*, *82*)

Moreover, spatial localization plays a pivotal role in enabling the oxidation of less reactive substrates while more potent scavengers are present.(*88*) This occurs by selectively depleting highly reactive antioxidant targets within specific cellular zones, allowing the oxidants to interact with less reactive targets, such as PTPs, within those localized regions.(*84*) The spatial restriction of ROS within subcellular microdomains is of utmost significance as it determines which proteins and specific cysteine residues undergo oxidation. Understanding this spatial regulation is vital for comprehending the complex interplay between oxidative stress and signaling pathways, shedding light on how ROS influence cellular responses.(*89*, *90*)

Therefore, it is essential to further investigate and elucidate these mechanisms, taking into account the specific contexts of cellular redox state, tissue environment, and intracellular localization. Advancing our understanding of the intricate relationship between ROS, particularly H_2O_2, and the regulation of cellular redox signaling holds great promise. Not only will it enhance our knowledge of pathological conditions, but it will also provide valuable insights for the development of targeted therapeutic strategies focused on modulating ROS levels and restoring redox balance.(*91–93*)

1.5. Objective

OA poses a significant burden on the quality of life for a growing portion of the population, and its current lack of a cure necessitates innovative approaches to identify viable treatment targets. ECM degradation stands as a prominent feature of OA pathology, and α5β1 integrin plays a important role in mediating the signaling cascade for metalloproteinase MMP-13 expression. Notably, MMP-13 is responsible for breaking down the extracellular matrix component fibronectin into fragments, which act as ligands for α5β1 integrin. However, the intracellular mechanism by which integrin transmits signals to induce MMP-13 generation remains unclear, as well as how this process leads to ROS, particularly H_2O_2, generation. Building upon the expanding knowledge of integrin biology, the primary objective of this thesis project is to develop a mechanistic understanding of the regulation of integrin signaling that is responsible for ECM remodeling in OA. By investigating and elucidating this pathway, we aim to uncover novel insights into the process of integrin-mediated MMP-13 generation, ultimately leading to the identification of promising therapeutic targets for OA. To achieve this objective, we propose the following specific aims:

Aim 1: Determine the precise mechanism by which α5β1 integrin transmits an outside-in signal, resulting in the generation of MMP-13 by chondrocytes in response to FN7-10.

Aim 2: Elucidate the underlying mechanism responsible for the selective ROS generation specifically in response to FN7-10, but not intact fibronectin.

Aim 3: Assess whether the signaling mechanism responsible for FN7-10-induced MMP-13 generation is active in OA cartilage.

By addressing these specific aims, we will advance our understanding of the intricate interplay between integrin signaling, ECM remodeling, and ROS generation in OA. This knowledge will contribute to the development of targeted therapeutic strategies aimed at modulating ROS levels and restoring redox balance, thus offering potential avenues for effective treatment approaches in OA and improving the lives of individuals affected by this debilitating condition.

2. CHAPTER 2: REDOXOSOMES MEDIATE ALPHA5 BETE1 INTEGRIN SIGNALING AND REGULATE CHONDROCTE MATRIX METALLOPROTEINASE PRODUCTION IN OSTEOARTHRITIS

2.1. Introduction

Many degenerative diseases, including OA, involve extracellular matrix degradation, in which proteolysis results in the production of bioactive matrix fragments (*32*, *94*–*99*). These disease-related ECM protein fragments interact with integrin transmembrane receptors to alter cell signaling processes relevant to cell migration, tissue development, and matrix remodeling, which contributes to disease progression (*100*–*104*). Recent studies on integrin signaling have provided evidence that integrin function is not restricted to the plasma membrane and that activated integrins can be present in endosomes to further relay extracellular-initiated signals (*105*–*107*). However, it is unclear how cells utilize integrin endocytic signaling to sense and respond to changes in the ECM, in particular matrix damage (*108*–*110*).

OA represents an ideal model system to study how cells function in response to ECM fragments generated by excessive protease activity (*16*, *111*, *112*). Chondrocytes are the sole cell type present in articular cartilage and are responsible for both the synthesis and degradation of cartilage matrix proteins, including fibronectin, proteoglycans, and collagens (*113*). Fragments of fibronectin have been found at micromolar levels in cartilage and synovial fluid obtained from individuals with arthritis, including osteoarthritis and rheumatoid arthritis (*99*, *114*–*116*). Matrix fragments appear to accelerate cartilage destruction, creating a vicious cycle by activating catabolic signaling that results in progressive cartilage loss. In advanced OA, cartilage loss and joint destruction are so severe that the only option is joint replacement (*117*, *118*).

Ligation of integrins with bioactive matrix fragments results in the production of ROS in cells, including chondrocytes (*119*, *120*). ROS serve as second messengers to sustain the signals associated with the activation of various growth factor and cytokine receptors as well as integrins (*121–123*). A prominent mechanism for redox regulation of signaling is through oxidation by hydrogen peroxide of susceptible cysteine thiols in cell signaling proteins, including various kinases and phosphatases (*123–125*). Because of the very short half-life of ROS in the intracellular environment, localized production in close proximity to redox-regulated signaling proteins is necessary for ROS to serve as signaling intermediaries (*88*). The mechanism by which ROS are produced in a temporospatial fashion to control integrin signaling, not only in OA chondrocytes but also more broadly, is unknown.

To develop a mechanistic understanding of the regulation of integrin signaling responsible for ECM remodeling, we used articular chondrocytes to investigate how ROS are generated subcellularly after α5β1 integrin binds to a fibronectin fragment (FN7-10). This fragment contains the Arg-Gly-Asp (RGD) attachment site found in domain 10 of the FN type III module as well as a synergy site DRVPHSRN in domain 9 that together promote opening of α5β1 to the active conformation (*126*, *127*). While activation of α5β1 integrin by FN7-10 can upregulate multiple MMPs and proinflammatory mediators involved in OA, we focused on MMP-13 production as a general measure given its prominent role in OA (*10*, *111*, *128*). MMP-13 has been shown to be a potent MMP for degrading fibronectin, resulting in the generation of bioactive matrix fragments (*129*). By tracking the sub-cellular location of both FN7-10 and α5 integrin, we identified the internalization of the ligand-integrin complex, which induced hydrogen peroxide generation in a temporospatial manner, beginning at the cell membrane and later continuing in NADPH oxidase 2 (Nox2)-containing early endosomes or “redoxosomes”. The spatial and temporal localization of hydrogen peroxide to sites of signaling activity was associated with the early endosomal translocation of Src. We additionally discovered evidence for signaling redoxosomes in human osteoarthritic cartilage at sites where matrix damage occurs, further implicating their role in mediating localized MMP production, which contributes to matrix protein degradation. Together, our findings determined that redoxosomes can transmit and sustain chondrocyte integrin signaling in OA. As redoxosomes have been proven to be pharmaceutically targetable in other disease models (*130*), this study provides support for the development of novel therapies for OA that target signaling in endosomes(*11*).

2.2. Results

2.2.1. Integrin endocytosis mediates the nonphagocytic route of FN7-10 uptake

Recent research has reported that integrin endosomal translocation can transmit signaling beyond the plasma membrane (*105*, *106*). Because of this, we sought to determine whether integrin endocytosis can occur in chondrocytes to transmit signaling in OA. We utilized nucleofection of plasmids to express EGFP-fused α5 integrin (α5 integrin–EGFP) and constitutively active Rab5 GTPase (mCherry–Rab5CA(Q79L)) to mark early endosomes in primary human articular chondrocytes, and generated a three-dimensional rendering of laser scanning microscopy images (*105*, *106*). We observed an increase in the percentage of α5 integrin–EGFP associated with early endosomes compared to the cell membrane within the first 2 hours after FN7-10 treatment (8.6 ± 1.1% at 30 min, 15.3 ± 2.6% at 1 h, 25.5 ± 4.7% at 2 h), followed by a decrease at 4 h (14.2 ± 2.0%) and 6 h (5.8 ± 1.1%) (**Figure 2.1, A and B**). These results were consistent with our live-cell imaging experiments, which showed the translocation of α5 integrin to early endosomes following FN7-10 treatment (**Figure 2.2, A and B**).

To further determine the fate of internalized integrin after entering early endosomes, we co-expressed constitutively active Rab7 GTPase (EGFP–Rab7CA(Q67L)) to mark late endosomes and mCherry-fused α5 integrin (α5 integrin–mCherry) in chondrocytes. The percentage of α5 integrin associated with late endosomal compartments compared to the cell membrane began to increase at 4 hours (25.7 ± 1.6%) after the addition of FN7-10, and similar distributions were observed at later time points, including 6 hours (25.2 ± 2.0%) and overnight

(25.9 ± 1.9%) (**Figure 2.3, A and B**). These findings suggest that during FN7-10-induced integrin endocytosis, α5 integrin enters early endosomes in the first two hours after FN7-10 treatment and then enters late endosomes between 2 and 4 hours after FN7-10 treatment.

While intact FN and FN7-10 both provide RGD sites for integrin binding (*131*), we observed that chondrocyte MMP-13 production (**Figure 2.4, A and B**) and MAP kinase signaling (**Figure 2.4C**) were triggered in response to FN7-10 but not to intact FN. To compare different sorting decisions in response to intact FN and FN7-10, we expressed mCherry–Rab5, mCherry–Rab7, or mCherry–Rab11 in chondrocytes to visualize the α5 integrin–EGFP distribution in early endosomes, late endosomes, and recycling endosomes, respectively. Compared to vehicle controls, both FN7-10 and intact FN-induced α5 integrin–EGFP to enter early endosomes within the first 2 hours after treatment (**Figure 2.5, A and D**). FN7-10 induced α5 integrin to enter late endosomes marked by Rab7 between 2 and 4 hours after the treatment (**Figure 2.5, B and E**). In contrast to FN7-10, intact FN induced α5 integrin to enter Rab11-positive endosomes via a “long loop” recycling pathway starting between 4 and 6 hours after treatment (**Figure 2.5, C and F**) (*132*, *133*).

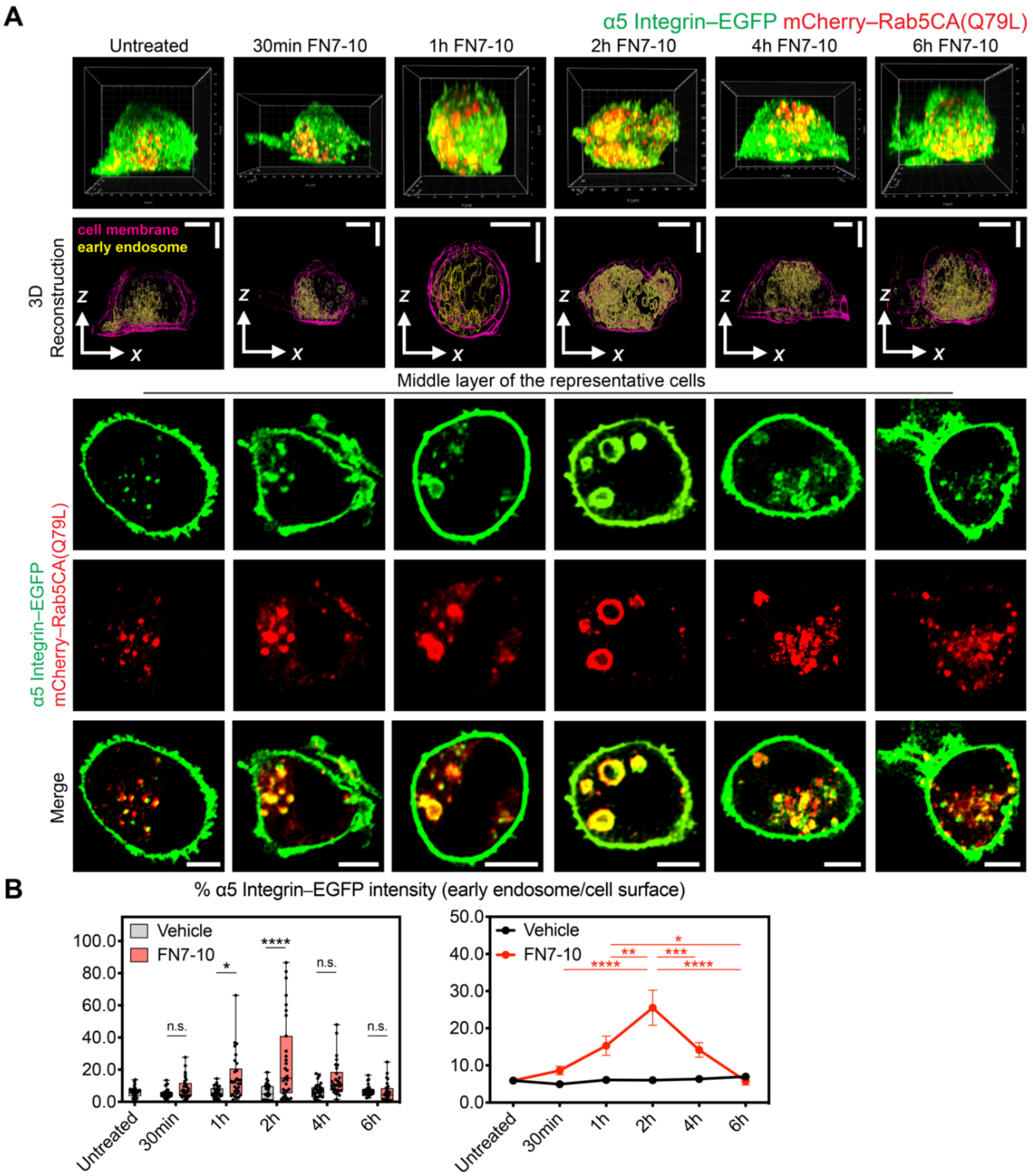

Figure 2.1 Internalization of α5 integrin to early endosomes after FN7-10 binding.

(**A**) Representative laser scanning microscopy images of human chondrocytes nucleofected with plasmids expressing α5 integrin–EGFP (green) and mCherry–Rab5CA(Q79L) (red) and then treated with FN7-10 (1 μM) for the indicated length of time. Panels represent 3D images (top panel) with corresponding reconstruction of the cell membrane (magenta) and early endosomes (yellow) in *x-z* view (middle panel) and images of the middle/ equatorial confocal sections of representative cells (bottom panel). 3D rendering of confocal images was performed using Imaris (Bitplane). (**B**) Quantification of the percentage of α5 integrin intensity (reconstructed from EGFP signal) associated with the early endosomal compartment compared to the cell membrane. Measurements were based on the reconstruction of *z*-stack confocal images from n = 30 or 31 cells per condition pooled from n = 2 independent donors for indicated lengths of vehicle (PBS) or FN7-10 treatments. Boundaries of the boxplot indicate the 25th and 75th percentiles, the horizontal line across the box is the median, and whiskers show the minima and maxima, with each dot representing the percentage in one cell. Data in the line graph are presented as mean ± s.e.m. Two-way ANOVA, considering both time and treatment and their interaction as factors, followed by Tukey's test was employed for multiple group comparisons across all possible pairwise comparisons. $^*P < 0.05$, $^{**}P < 0.01$, $^{***}P < 0.001$, $^{****}P < 0.0001$; n.s., not significant.

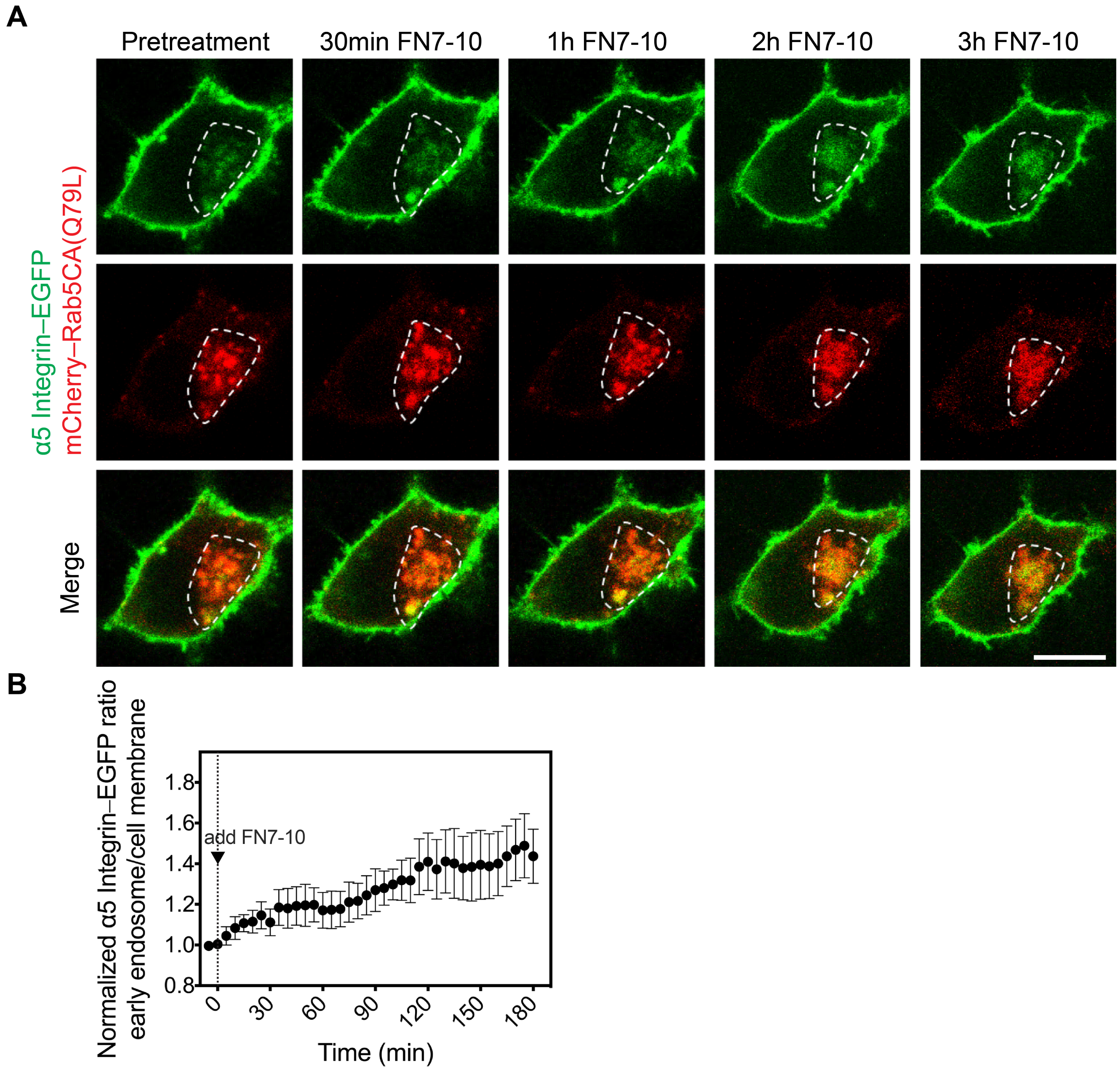

Figure 2.2 Internalization of α5 integrin to early endosomes after treatment with FN7-10.

(**A**) Live-cell images of a human chondrocyte nucleofected with plasmid constructs expressing α5 integrin–EGFP (green) and mCherry–Rab5CA(Q79L) (red) in response to FN7-10 (1 µM), indicating that α5 integrin–EGFP enters early endosomes upon activation by FN7-10. Live-cell imaging was performed at 5 min per frame with FN7-10 being added after the second scan (10 min) and was recorded over the course of 180 min following the treatment for a total of 38 frames. Regions of interest (ROIs) of early endosomes indicated by mCherry–Rab5CA(Q79L) for ratiometric analysis are shown as white dashed circles. (**B**) Ratiometric analysis measuring the mean intensity ratio of α5-integrin–EGFP in the early endosome compared to the cell membrane across 180 min imaging period. The baseline intensity ratio was determined by the average intensity ratio of the first two frames before the treatment and normalized to 1 Measurements were derived from n = 7 cells pooled from n = 4 independent donors. Data are presented as mean ± s.e.m, arbitrary units. Scale bars, 5 µm.

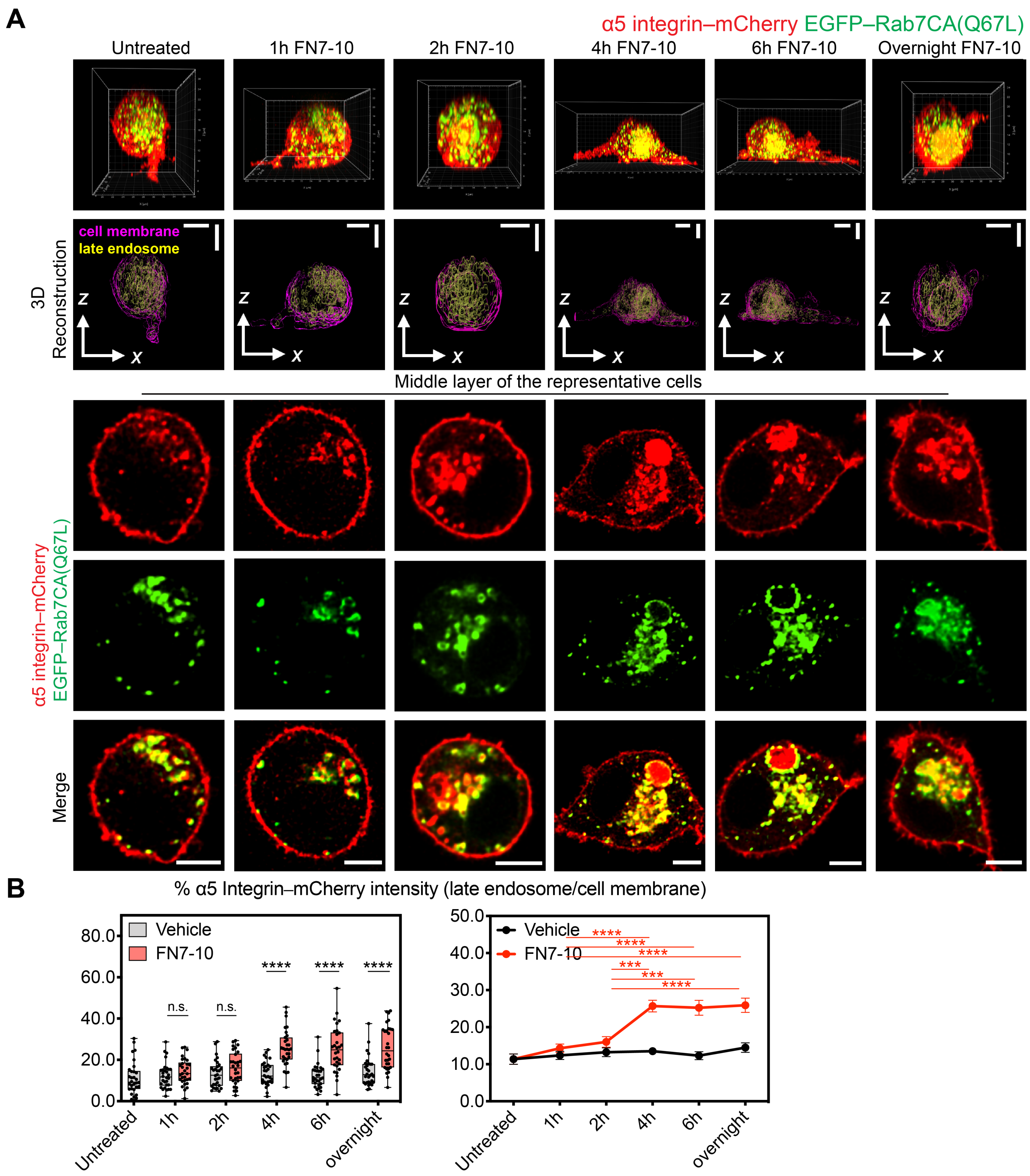

Figure 2.3 FN7-10 induces the internalization of α5 integrin towards late endosomes.

(**A**) Representative laser scanning microscopy images of human chondrocytes nucleofected with plasmid constructs expressing α5 integrin–mCherry (red) and EGFP–Rab7CA(Q67L) (green) treated with FN7-10 (1 μM) for the indicated lengths of time. Panels represent 3D images (top panel) with corresponding reconstruction of the cell membrane (magenta) and late endosome (yellow) in *x*-*z* view (middle panel) and middle layers of representative cells (bottom panel). (**B**) Quantification of the percentage of α5 integrin intensity (reconstructed from mCherry signal) inside the late endosomal compartment compared to the cell membrane. Measurements were based on the reconstruction of *z*-stack confocal images from n = 30 cells per condition and n = 2 independent donors for the indicated lengths of vehicle (PBS) or FN7-10 treatments. Boundaries of the boxplot indicate the 25th and 75th percentiles, the horizontal line across the box is the median, and whiskers show the minima and maxima, with each dot representing the percentage in one cell. Data in the line graph are presented as mean ± s.e.m. Two-way ANOVA, considering both time and treatment and their interaction as factors, followed by Tukey's test was employed for multiple group comparisons across all possible pairwise comparisons. ***$P < 0.001$, ****$P < 0.0001$; n.s., not significant. Scale bars, 5 μm.

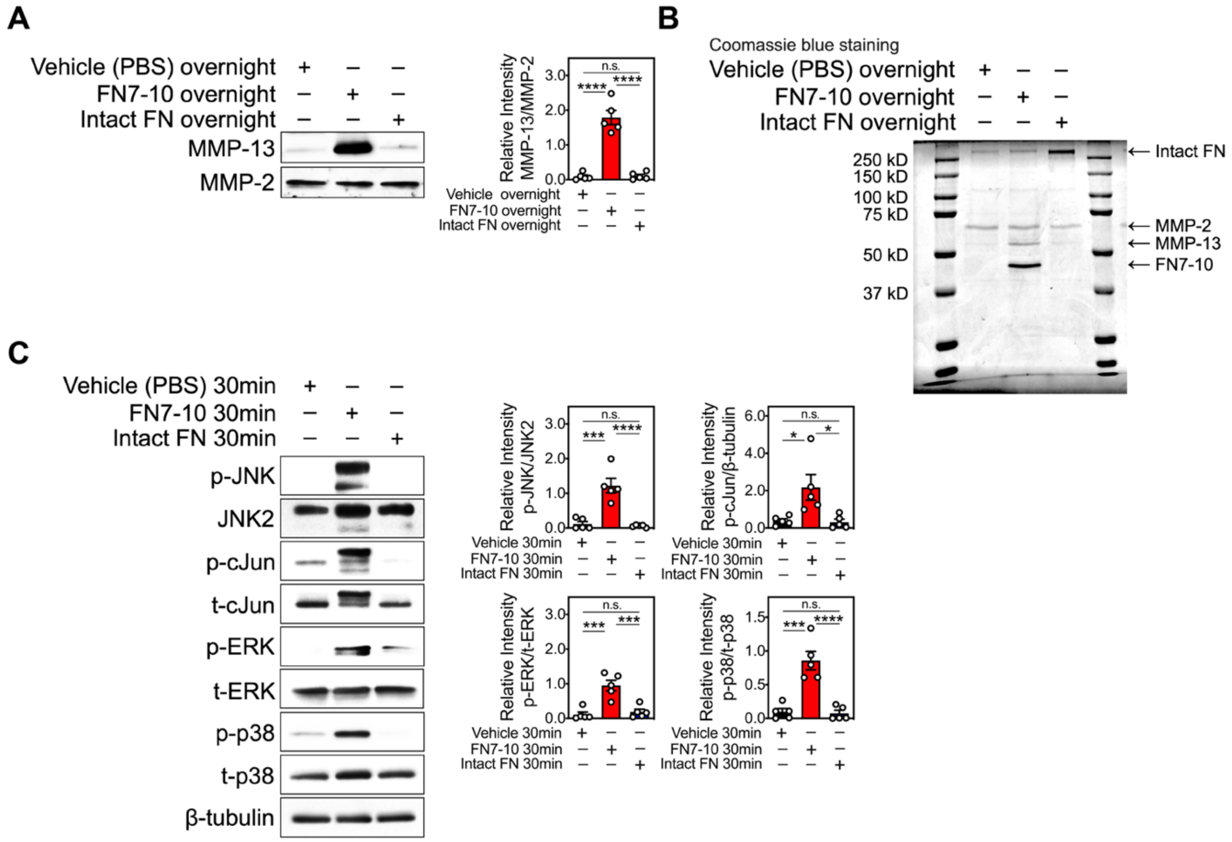

Figure 2.4 α5β1 binding of FN7-10 but not intact FN induces MAP kinase signaling and MMP-13 production.

(**A**) Immunoblot analysis and densitometric quantification of MMP-13 and MMP-2 in the same volume of conditioned medium from human articular chondrocytes in response to PBS vehicle, FN7-10 (1 μM), or intact FN (10 μg/mL) overnight. Measurements were derived from n = 5 independent donors. (**B**) Coomassie blue staining of SDS–PAGE gel showing the molecular weight of intact FN, MMP-13, MMP-2 used as a loading control, and purified recombinant FN7-10 (indicated by arrows, from top to bottom) in the same volume of conditioned medium from human articular chondrocytes in response to PBS vehicle, FN7-10 (1 μM), or intact FN (10 μg/mL) overnight (18 h). (**C**) Immunoblot analysis and densitometric quantification € of MAP kinase phosphorylation in protein lysates in response to PBS vehicle, FN7-10 (1 μM), or intact FN (10 μg/mL) for 30 min. Measurements were derived from n = 5 biologically independent experiments. For media samples, MMP-2 was used as a loading control as it was not altered by the stimuli or inhibitors tested. To quantify proteins from cell lysates, non-phosphorylated proteins were used as controls. Chondrocytes were serum-starved prior to experiments. Data are mean fold change ± s.e.m band relative pixel intensity in arbitrary units. One-way ANOVA followed by Tukey's test was employed for multiple group comparisons. *$P < 0.05$, ***$P < 0.001$, ****$P < 0.0001$; n.s., not significant.

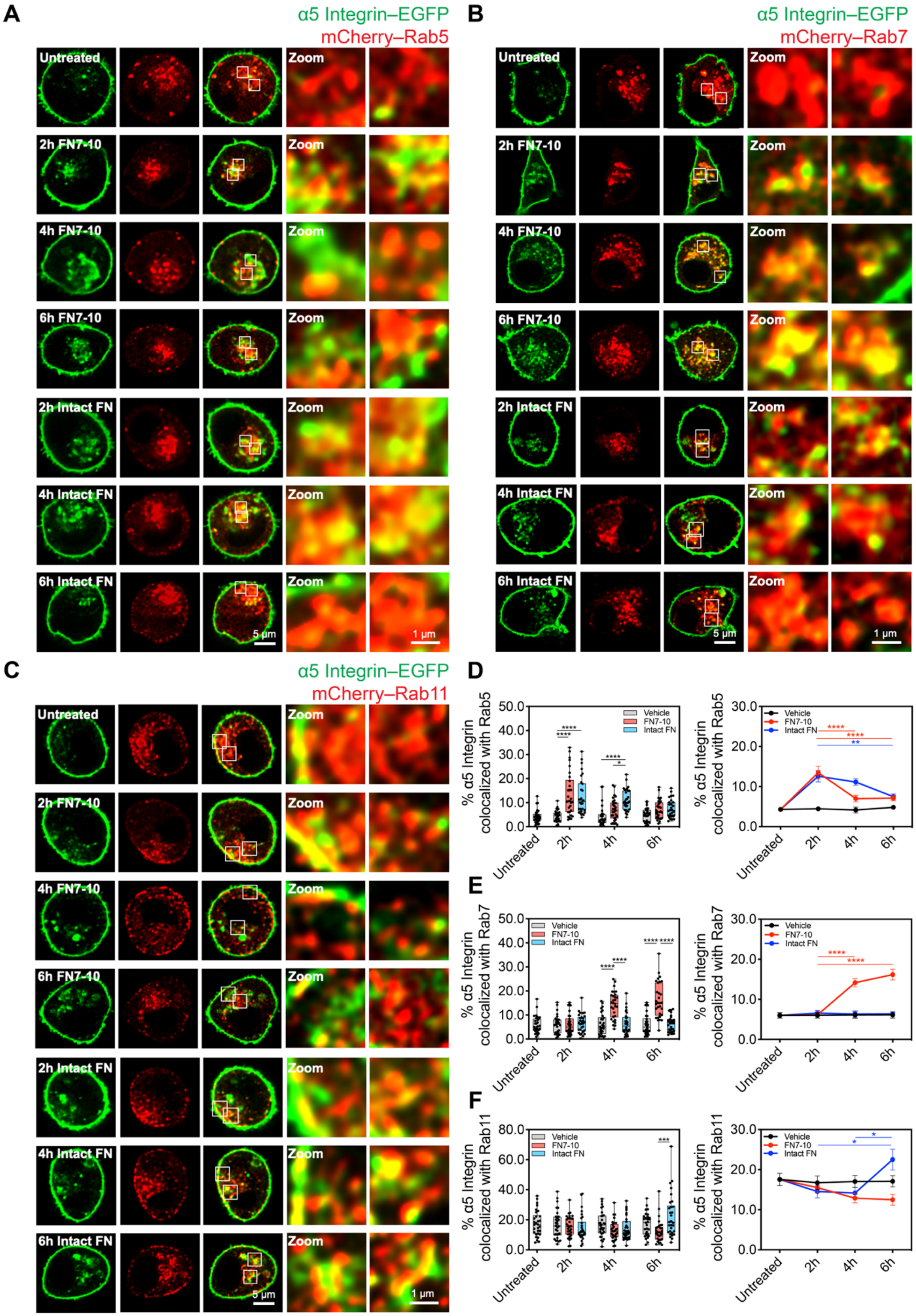
A
α5 Integrin–EGFP
mCherry–Rab5
Untreated
2h FN7-10
4h FN7-10
6h FN7-10
2h Intact FN
4h Intact FN
6h Intact FN
Zoom
5 μm
1 μm
B
α5 Integrin–EGFP
mCherry–Rab7
Untreated
2h FN7-10
4h FN7-10
6h FN7-10
2h Intact FN
4h Intact FN
6h Intact FN
Zoom
5 μm
1 μm
C
α5 Integrin–EGFP
mCherry–Rab11
Untreated
2h FN7-10
4h FN7-10
6h FN7-10
2h Intact FN
4h Intact FN
6h Intact FN
Zoom
5 μm
1 μm
D
% α5 Integrin colocalized with Rab5
50.0
40.0
30.0
20.0
10.0
0.0
Vehicle
FN7-10
Intact FN
****
****
****
*
Untreated
2h
4h
6h
% α5 Integrin colocalized with Rab5
30.0
20.0
10.0
0.0
Vehicle
FN7-10
Intact FN
****
****
**
Untreated
2h
4h
6h
E
% α5 Integrin colocalized with Rab7
50.0
40.0
30.0
20.0
10.0
0.0
Vehicle
FN7-10
Intact FN
****
****
****
****
Untreated
2h
4h
6h
% α5 Integrin colocalized with Rab7
30.0
20.0
10.0
0.0
Vehicle
FN7-10
Intact FN
****
****
Untreated
2h
4h
6h
F
% α5 Integrin colocalized with Rab11
80.0
60.0
40.0
20.0
0.0
Vehicle
FN7-10
Intact FN
***
Untreated
2h
4h
6h
% α5 Integrin colocalized with Rab11
30.0
20.0
10.0
0.0
Vehicle
FN7-10
Intact FN
*
*
Untreated
2h
4h
6h

Figure 2.5 Differential endocytic trafficking of integrin α5 in response to FN7-10 and intact FN.

(**A**, **B**, and **C**) Representative laser scanning microscopy images of human chondrocytes nucleofected with plasmid constructs expressing α5 integrin–EGFP (shown in green) and mCherry–Rab5 (**A**), mCherry–Rab7 (**B**), or mCherry–Rab11 (**C**) (shown in red) to indicate integrin trafficking in response to FN7-10 (1 μM), intact FN (10 μg/mL), as well as PBS vehicle at the indicated time points. (**D**, **E**, and **F**) Quantification of the percentage of α5 integrin colocalized with early (mCherry–Rab5) (**D**), late (mCherry–Rab7) (**E**), or recycling (mCherry–Rab11) (**F**) endosomes. Measurements were based on the reconstruction of *z*-stack confocal images from n = 30 cells per condition pooled from n = 2 independent donors for the indicated lengths of vehicle (PBS), FN7-10, or intact FN treatment. Boundaries of the boxplot (left panel) indicate the 25th and 75th percentiles, the horizontal line across the box is the median, and whiskers show the minima and maxima, with each dot representing the percentage in one cell. Data in the line graph (right panel) are presented as mean ± s.e.m. Two-way ANOVA, considering both time and treatment and their interaction as factors, followed by Tukey's test was employed for multiple group comparisons across all possible pairwise comparisons. *$P < 0.05$, **$P < 0.01$, ***$P < 0.0001$, ****$P < 0.0001$. Scale bars, 1 μm (magnified views) and 5 μm (whole-cell images).

Next, we investigated whether FN7-10 is endocytosed by chondrocytes together with the integrin receptor. For this, we generated FN7-10–EGFP (**Figure 2.6, A to C**), which was found to induce MMP-13 production and MAP kinase signaling (**Figure 2.6D**), in a similar way to unlabeled FN7-10. We treated mCherry–α5 integrin expressing chondrocytes with FN7-10–EGFP. We found that the size of FN7-10–EGFP inside the cell (**Figure 2.7, A and B**), and the colocalization between FN7-10–EGFP and α5 integrin–mCherry (**Figure 2.7, A and C**) both increased following FN7-10–EGFP treatment. Because FN7-10 induced α5 integrin to enter early endosomes, we sought to determine whether FN7-10 was also endocytosed into Rab5-containing endosomes during this time. We treated chondrocytes expressing mCherry–Rab5CA(Q79L) with FN7-10–EGFP and noted that the percentage of FN7-10–EGFP associated with Rab5-containing endosomal compartments increased with time (60.0 ± 5.2% at 30 min, 79.9 ± 4.0% at 1 h, and 90.1 ± 1.3% at 2 h, compared to the control of 7.9 ± 1.2%) (**Figure 2.8, A and F**), demonstrating that FN7-10–EGFP was endocytosed into early endosomes. In line with these findings, live-cell time-lapse imaging also indicated that FN7-10–EGFP was endocytosed into Rab5-containing early endosomes (**Figure 2.8, B and C**) and that endocytosis was accompanied by integrin internalization (**Figure 2.8, D and E**).

The above experiments revealed intriguing differences in the catalytic response (**Figure 2.4**) and α5 integrin trafficking (**Figure 2.5**) when cells were treated with FN7-10 versus intact FN, even though both contain the RGD integrin binding sequence. We next examined whether intact FN undergoes endocytosis in manner similar to or different from FN7-10, and whether their accompanying endocytosed integrin was in the active or inactive conformation. Moreover, we compared (1) the sustained activity/ligand occupancy of the endocytosed integrins in response to FN7-10 versus intact FN and (2) the time-dependent endocytosis patterns of the β1 subunit compared to the α subunit. Human chondrocytes were treated with fluorescently labeled FN7-10 or intact FN. Successful labeling and correct molecular weights were verified by in-gel fluorescence visualization and Coomassie blue staining (**Figure 2.9**). Endocytosis of both FN7-

10 and intact FN was observed (**Figure 2.10**). Accompanying this ligand endocytosis, we observed prominent endocytosis of the active conformation of β1 integrin (identified by 9EG7 antibody staining), as well as total β1 integrin (stained using K20 antibody) within Rab5$^+$ early endosomes following two-hour treatment with either FN7-10 or intact FN (**Figure 2.10, A and B**). Beyond the two-hour time point, however, we observed distinct endocytosis routes for the β1 integrin in response to FN7-10 or intact FN, similar to the α5 subunit results shown above. Specifically, in cells treated with FN7-10, we observed enhanced colocalization between both active and total β1 integrin with Rab7, suggesting that FN7-10 and β1 integrin undergo transit through late endosomes (**Figure 2.10, C and D**). In contrast, when exposed to intact FN, the β1 integrin remained occupied with FN and utilized the long-loop trafficking route through Rab11-containing endosomes (**Figure 2.10, E and F**).

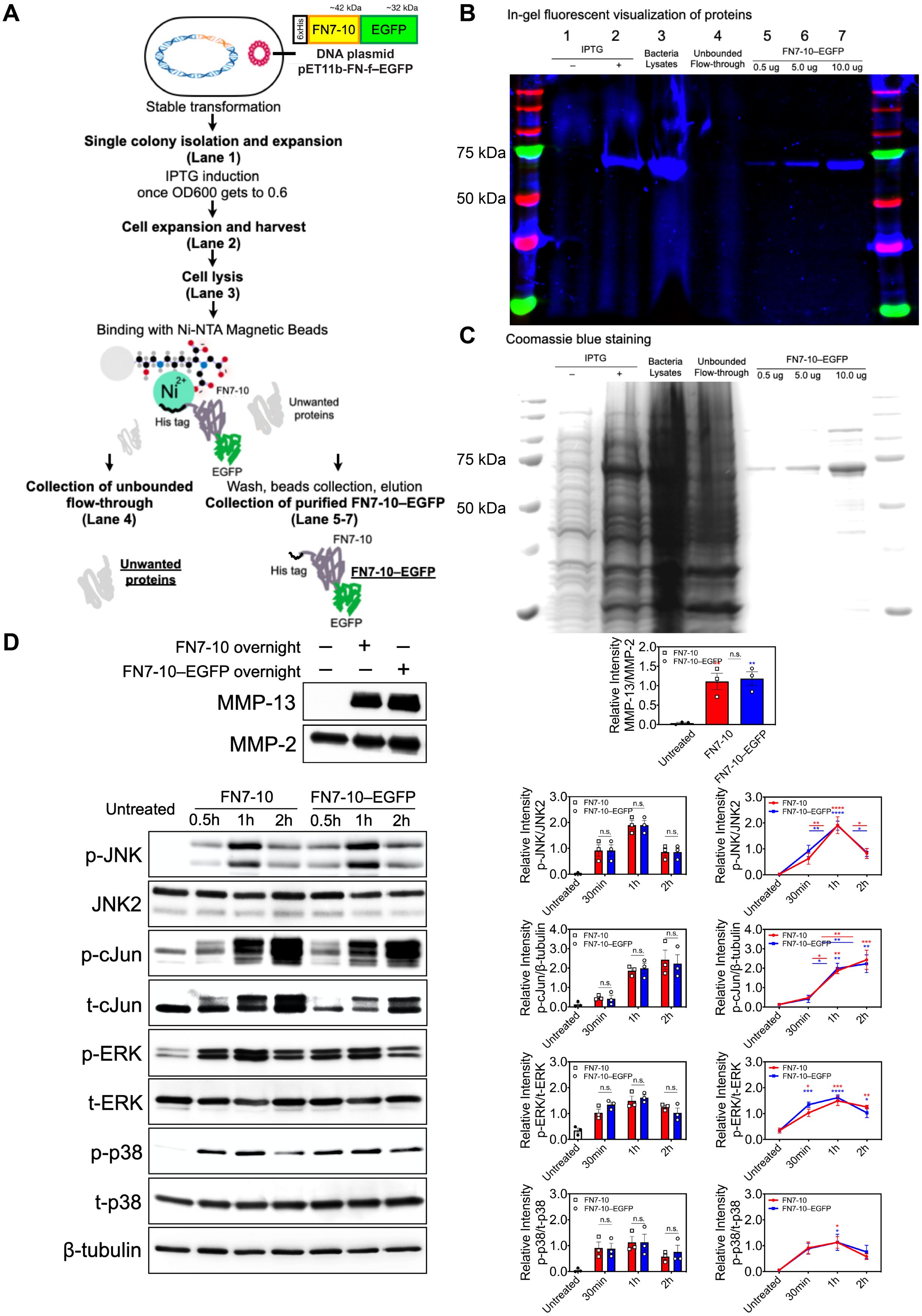
A
~42 kDa
~32 kDa
6xHis
FN7-10
EGFP
DNA plasmid
pET11b-FN-f–EGFP
Stable transformation
Single colony isolation and expansion
(Lane 1)
IPTG induction
once OD600 gets to 0.6
Cell expansion and harvest
(Lane 2)
Cell lysis
(Lane 3)
Binding with Ni-NTA Magnetic Beads
Ni2+
FN7-10
His tag
Unwanted proteins
EGFP
Collection of unbounded flow-through
(Lane 4)
Wash, beads collection, elution
Collection of purified FN7-10–EGFP
(Lane 5-7)
Unwanted proteins
FN7-10
His tag
FN7-10–EGFP
EGFP
B
In-gel fluorescent visualization of proteins
1
2
3
4
5
6
7
IPTG
–
+
Bacteria Lysates
Unbounded Flow-through
FN7-10–EGFP
0.5 ug
5.0 ug
10.0 ug
75 kDa
50 kDa
C
Coomassie blue staining
IPTG
–
+
Bacteria Lysates
Unbounded Flow-through
FN7-10–EGFP
0.5 ug
5.0 ug
10.0 ug
75 kDa
50 kDa
D
FN7-10 overnight – + –
FN7-10–EGFP overnight – – +
MMP-13
MMP-2
Relative Intensity MMP-13/MMP-2
FN7-10
FN7-10–EGFP
n.s.
Untreated
FN7-10
FN7-10–EGFP
Untreated
FN7-10
FN7-10–EGFP
0.5h
1h
2h
0.5h
1h
2h
p-JNK
JNK2
p-cJun
t-cJun
p-ERK
t-ERK
p-p38
t-p38
β-tubulin
Relative Intensity p-JNK/JNK2
Relative Intensity p-cJun/β-tubulin
Relative Intensity p-ERK/t-ERK
Relative Intensity p-p38/t-p38
FN7-10
FN7-10–EGFP
n.s.
Untreated
30min
1h
2h

Figure 2.6 Generation and testing of recombinant EGFP fusion FN7-10.

(**A**) Schematic workflow showing the generation and purification of EGFP fusion FN7-10 (FN7-10–EGFP) recombinant protein. FN7-10–EGFP has an N-terminal His-tag and a C-terminal EGFP with a predicted molecular weight of approximately 74 kDa. The PET11b-FN7-10–EGFP plasmid was transformed into Escherichia coli prior to IPTG induction and purification through His-tag affinity chromatography. (**B, C**) In-gel fluorescent visualization of proteins (**B**), followed by Coomassie blue staining of SDS–PAGE gel (**C**). The sequential approach enables the determination molecular weight of purified recombinant FN7-10–EGFP. From lanes 1–7: Escherichia coli before (lane 1) and after (lane 2) IPTG induction, bacteria lysate containing expressed His-tagged recombinant protein (lane 3), unbound protein fraction from affinity chromatography (lane 4), and different amounts of FN7-10–EGFP (from lanes 5–7). (**D**, **E**) Immunoblot analysis (**D**) and densitometric quantification (**E**) comparing MMP-13 generation in response to FN7-10 (1 μM) or FN7-10–EGFP (1 μM) overnight (18 h). (**F**, **G**) Immunoblot analysis and (**F**) densitometric quantification (**G**) comparing the kinetics of stimulated MAP kinase activation in response to FN7-10 (1 μM) or FN7-10–EGFP (1 μM) for 30 min, 1 h, and 2 h or untreated control. For media samples, MMP-2 was used as a loading control, as it was not altered by the stimuli or inhibitors tested. To quantify proteins from cell lysates, non-phosphorylated proteins were used as controls. Measurements were derived from n = 3 independent donors. Data are presented as the mean fold change ± s.e.m band relative pixel intensity, arbitrary units. Two-way ANOVA, considering both time and treatment and their interaction as factors, followed by Tukey's test was employed for multiple group comparisons across all possible pairwise comparisons. $^{*}P < 0.05$, $^{**}P < 0.01$, $^{***}P < 0.001$, $^{****}P < 0.0001$; n.s., not significant.

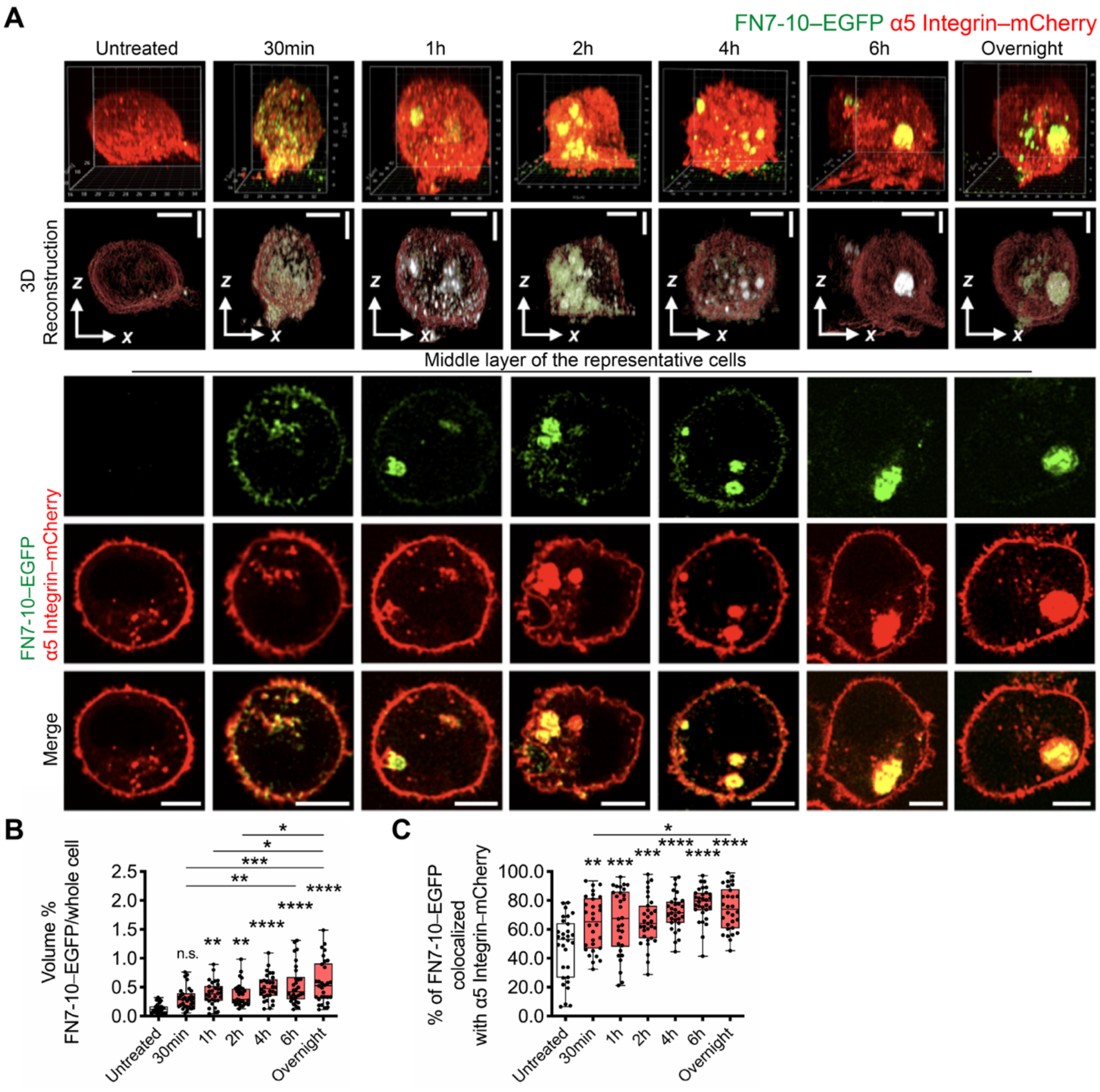

Figure 2.7 α5 integrin mediates the internalization of FN7-10.

(**A**) Representative laser scanning microscopy images of human chondrocytes nucleofected with plasmid constructs expressing α5 integrin–mCherry (red) treated with EGFP fusion FN7-10 (FN7-10–EGFP, 1 μM, green) for the indicated lengths of time. Panels represent three-dimensional images with corresponding reconstruction in *x*-*z* view (top panel) and middle layers of representative cells (bottom panel). Colocalization of FN7-10–EGFP with α5 integrin–mCherry is shown in white. (**B**) Quantification of the volume percentage of FN7-10–EGFP associated with the cell compared to the volume of the whole cell. (**C**) Quantification of the percentage of FN-7-10–EGFP colocalized with α5 integrin–mCherry. Measurements were performed based on the reconstruction of *z*-stack confocal images from n = 30 or 31 cells per condition pooled from n = 2 independent donors. Boundaries of the boxplot indicate the 25th and 75th percentiles, the horizontal line across the box is the median, and whiskers show the minima and maxima, with each dot representing the percentage in one cell. One-way ANOVA followed by Tukey's test was employed for multiple group comparisons. *$P < 0.05$, **$P < 0.01$, ***$P < 0.001$, ****$P < 0.0001$; a single asterisk indicates a significant difference from controls; n.s, not significant. Scale bars, 5 μm.

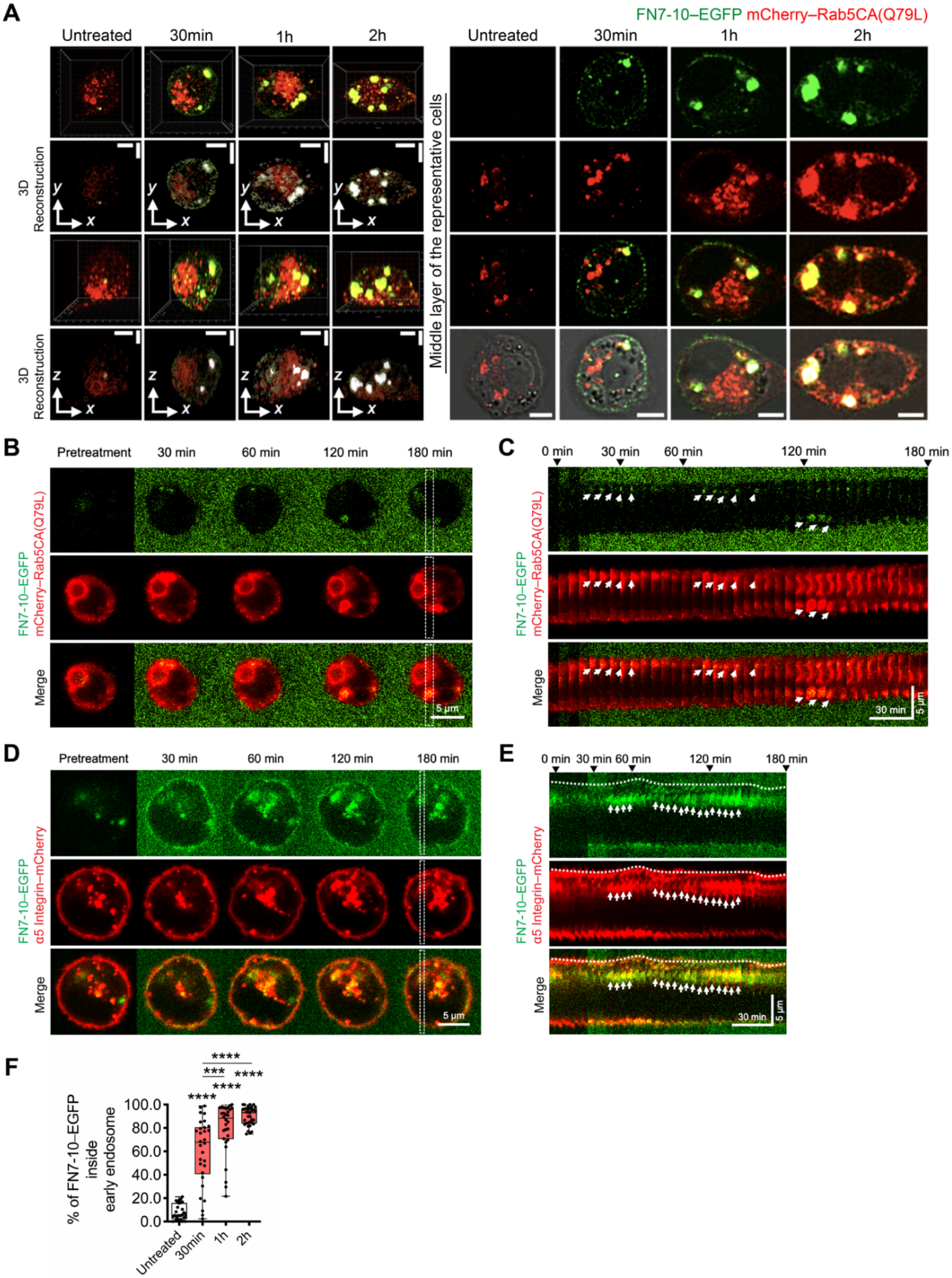
A
FN7-10–EGFP mCherry–Rab5CA(Q79L)
Untreated
30min
1h
2h
3D Reconstruction
y
x
z
Middle layer of the representative cells
B
Pretreatment
30 min
60 min
120 min
180 min
FN7-10–EGFP
mCherry–Rab5CA(Q79L)
Merge
5 μm
C
0 min
30 min
60 min
120 min
180 min
30 min
5 μm
D
α5 Integrin–mCherry
E
F
% of FN7-10–EGFP inside early endosome
100.0
80.0
60.0
40.0
20.0
0.0
Untreated
30min
1h
2h
****
***

Figure 2.8 The internalization of FN7-10 to early endosomes mediated by α5 integrin.

(**A**) Representative laser scanning microscopy images of human chondrocytes nucleofected with plasmids expressing mCherry–Rab5CA(Q79L) (red) treated with EGFP fusion FN7-10 (FN7-10–EGFP) (1 μM, green) for the indicated lengths of time. Panels represent three-dimensional images with corresponding reconstruction in the *x*-*y* and *x*-*z* view (left panel) and middle layers of representative cells (right panel). FN7-10–EGFP inside the early endosomal compartment is shown in white. (**B**) Live-cell images of human chondrocyte transfected with plasmids expressing mCherry–Rab5CA(Q79L) (red, middle panel) treated with FN7-10–EGFP (1 μM, green, top panel) and merged images (bottom panel) at different time points. (**C**) Kymograph of the dashed rectangle area in (**B**) to demonstrate the internalization of FN7-10–EGFP (shown in green) and mCherry–Rab5CA(Q79L) (shown in red) indicated by the arrows. (**D**) Live-cell images of human chondrocyte transfected with plasmids expressing α5 integrin–mCherry (red, middle panel) treated with FN7-10–EGFP (1 μM, green, top panel) and merged images (bottom panel) at different time points. (**E**) Kymograph of the dashed rectangle area in (**D**) to demonstrate the internalization of FN7-10–EGFP (shown in green) and α5 integrin–mCherry (shown in red) indicated by the arrows. (**F**) Quantification of the percentage of FN7-10–EGFP associated with early endosomal compartments based on the reconstruction of *z*-stack confocal images (vehicle, n = 30 cells; 30 min, n = 30 cells; 1 h, n = 30 cells; 2 h, n = 35 cells pooled from n = 2 independent donors). Boundaries of the boxplot indicate the 25th and 75th percentiles, the horizontal line across the box is the median, and whiskers show the minima and maxima, with each dot representing the percentage in one cell. One-way ANOVA followed by Tukey's test was employed for multiple group comparisons. $^{***}P < 0.001$, $^{****}P < 0.0001$; a single asterisk indicates a significant difference from controls. Scale bars, 5 μm in (**A**, **B**, and **D**) 30 min (horizontal axis) and 5 μm (vertical axis) in (**C** and **E**).

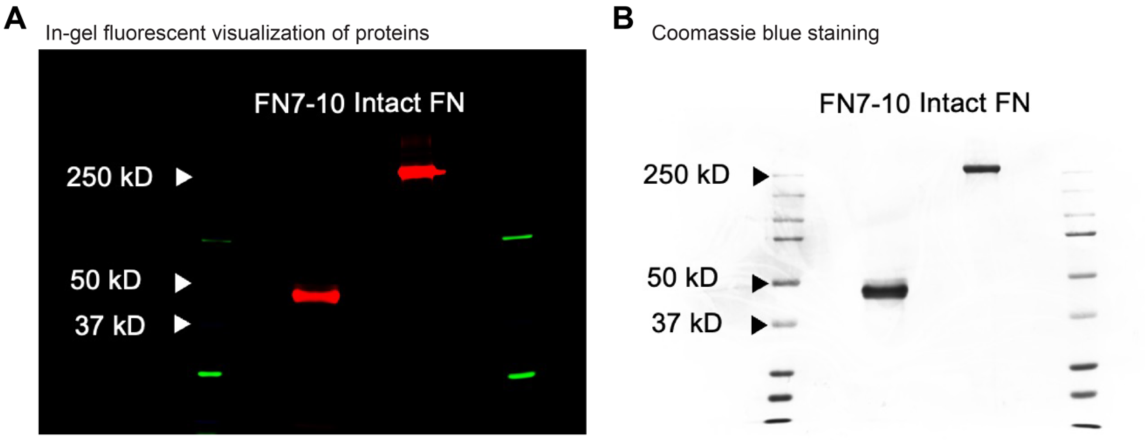

Figure 2.9 Fluorescent labeling of FN7-10 and intact FN.

Purified FN7-10 and intact FN proteins were fluorescently labeled with Alexa Fluor 647. In-gel fluorescent visualization of fluorescently labeled proteins (**A**), followed by Coomassie blue staining of SDS–PAGE gel (**B**). The sequential approach enables the determination of the molecular weights of labeled proteins.

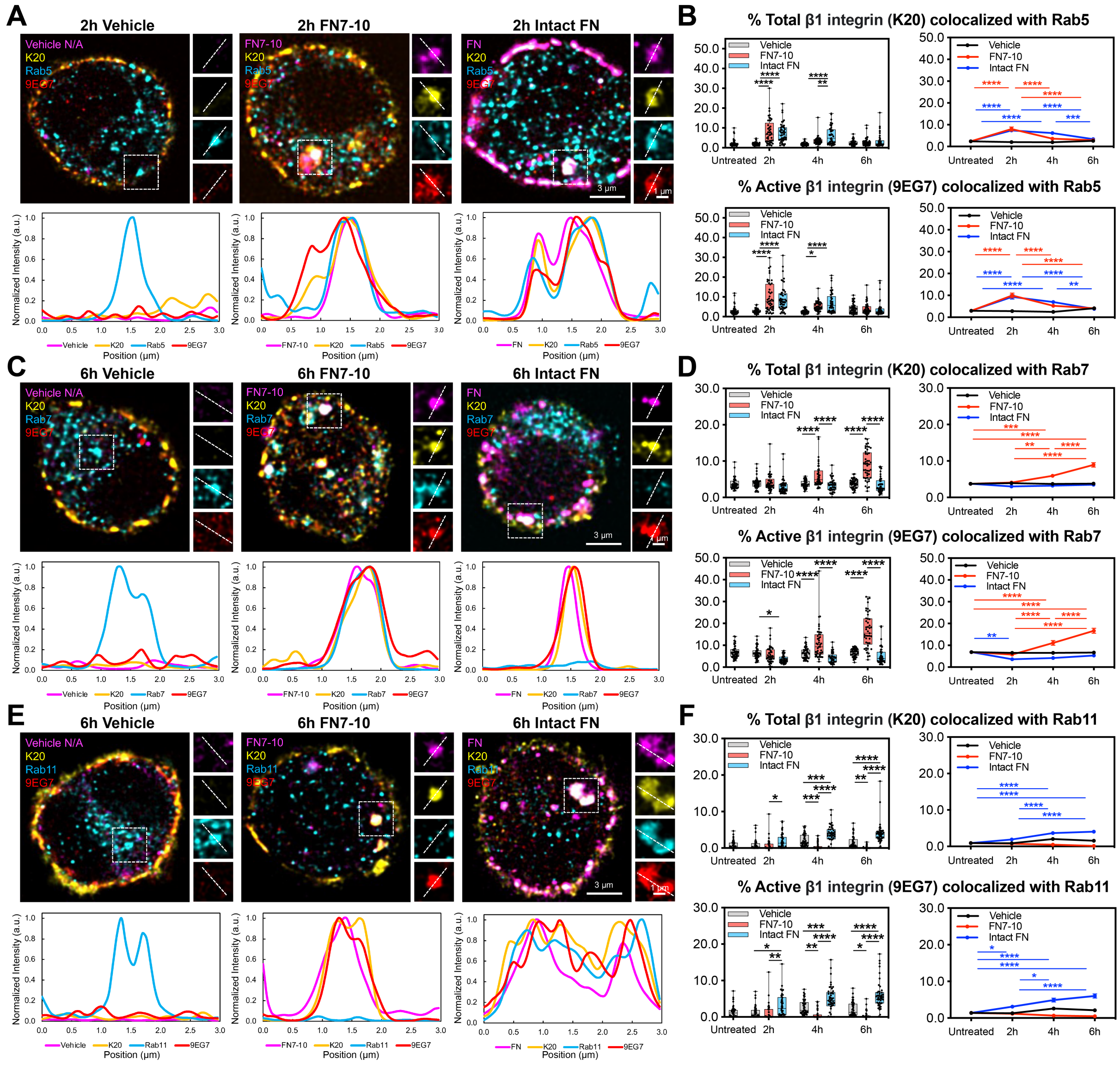

Figure 2.10 Differential endosomal trafficking of β1 integrin in response to FN7-10 and intact FN.

Serum-starved human chondrocytes were subjected to various treatments for the indicated lengths of time as follows: vehicle (PBS) treatment (left panel), treatment with Alexa Fluor 647-labelled FN7-10 (1 μM, shown in magenta) (middle panel), or treatment with Alexa Fluor 647-labelled intact FN (10 μg/mL, shown in magenta) (right panel). Subsequently, the cells were fixed, permeabilized, and subjected to staining using specific antibodies against total β1 integrin (K20, shown in yellow) and active β1 integrin (9EG7, shown in red) and the different small Rab-GTPases (shown in cyan) Rab5 (**A, B**), Rab7 (**C, D**), and Rab11 (**E, F**), which allowed for the investigation of β1 integrin trafficking pathways. (**A, C, and E**) The graphs presented display the middle (equatorial) layers of selected laser scanning microscopy images depicting human chondrocytes under indicated treatment conditions. Fluorescence intensity profiling along dashed lines of white boxed regions indicating the localization of Alexa Fluor 647-labelled FN7-10 or intact FN, β1 integrin (both total and active forms), as well as different small Rab-

GTPases. (**B, D, and F**) Quantitative analysis was performed to determine the percentage of β1 integrin (both total and active forms) that exhibited colocalization with early endosomes (Rab5) (**B**), late endosomes (Rab7) (**D**), and recycling endosomes (Rab11) (**F**) in response to indicated treatments for specified durations. Measurements were based on the reconstruction of *z*-stack confocal images from n = 45 cells per condition pooled from n = 2 independent donors. Boundaries of the boxplot indicate the 25th and 75th percentiles, the horizontal line across the box is the median, and whiskers show the minima and maxima, with each dot representing the percentage in one cell. Data in the line graph are presented as mean ± s.e.m. Two-way ANOVA, considering both time and treatment and their interaction as factors, followed by Tukey's test was employed for multiple group comparisons across all possible pairwise comparisons. $^{*}P < 0.05$, $^{**}P < 0.01$, $^{***}P < 0.0001$, $^{****}P < 0.0001$. Scale bars, 1 μm (magnified views) and 3 μm (whole-cell images).

2.2.2. Integrin endocytosis is required for the activation of chondrocyte catabolic signaling and matrix metalloproteinase production

We then investigated whether endocytosis plays a role in α5β1 signaling and MMP production induced by FN7-10. Chondrocytes were pretreated with Dynasore, a dynamin inhibitor, prior to FN7-10 stimulation. This treatment blocked α5 integrin–EGFP and FN7-10–EGFP internalization into early endosomal compartments, as shown by a significant decrease in the distribution of α5 integrin–EGFP (**Figure 2.11, A and C**) and FN7-10–EGFP (**Figure 2.11, B and D**) in Rab5-positive endosomes. There was also a dose-dependent inhibition of FN7-10-induced MMP-13 production and MAP kinase signaling (**Figure 2.11E**). In line with the pharmacological inhibition of endocytosis with Dynasore, the expression of a dominant-negative mutant of Rab5 (Rab5(S34N)) also inhibited endocytosis (**Figure 2.11, A to D**) and attenuated FN7-10-induced MMP-13 production (**Figure 2.11F**) and MAP kinase signaling (**Figure 2.11G**).

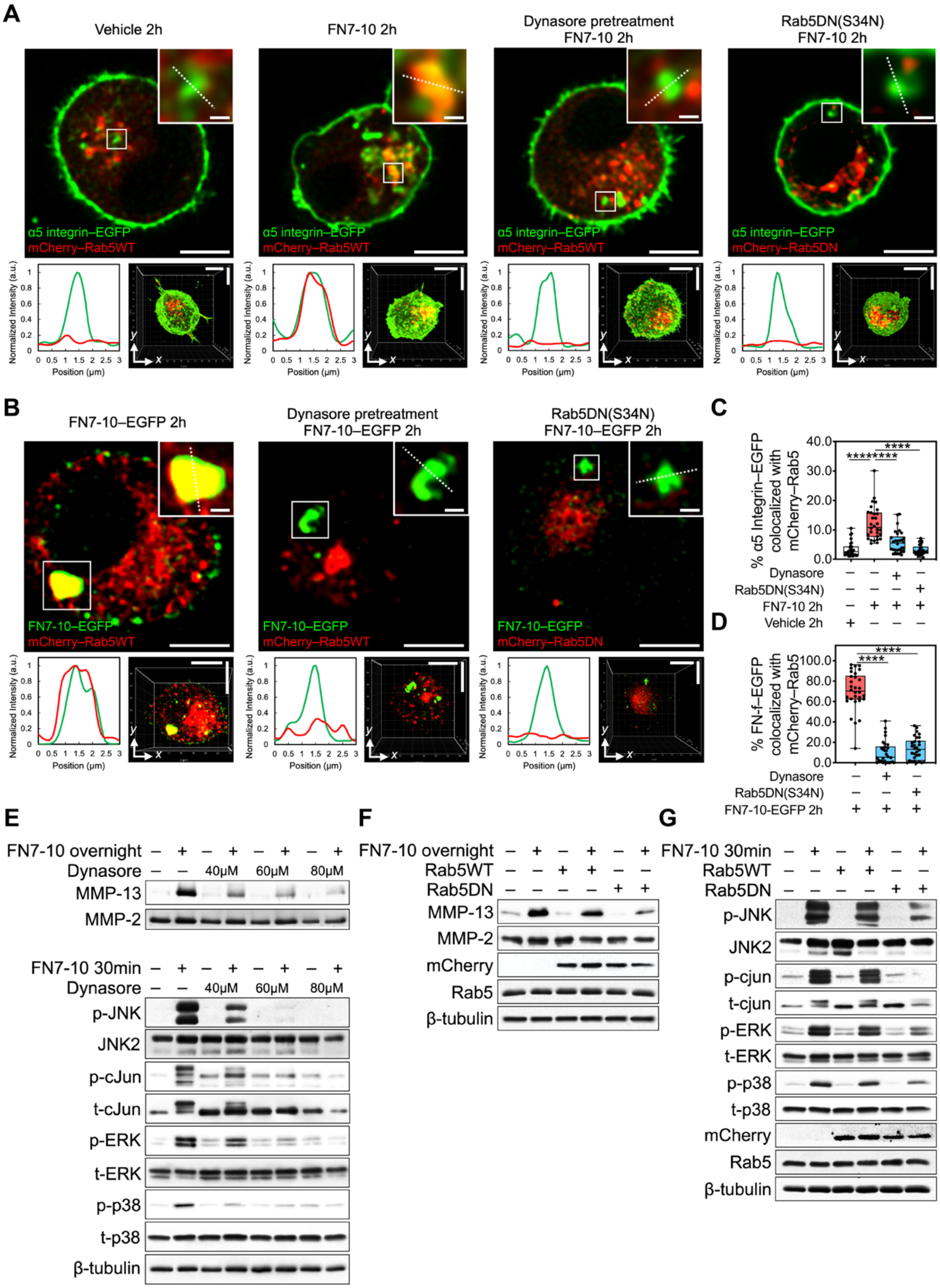
A
Vehicle 2h
FN7-10 2h
Dynasore pretreatment FN7-10 2h
Rab5DN(S34N) FN7-10 2h
α5 integrin–EGFP
mCherry–Rab5WT
mCherry–Rab5DN
Normalized Intensity (a.u.)
Position (μm)
0 0.5 1 1.5 2 2.5 3
0 0.2 0.4 0.6 0.8 1
y
x
B
FN7-10–EGFP 2h
Dynasore pretreatment FN7-10–EGFP 2h
Rab5DN(S34N) FN7-10–EGFP 2h
FN7-10–EGFP
mCherry–Rab5WT
mCherry–Rab5DN
C
% α5 Integrin–EGFP colocalized with mCherry–Rab5
0.0 10.0 20.0 30.0 40.0
****
****
Dynasore – – + –
Rab5DN(S34N) – – – +
FN7-10 2h – + + +
Vehicle 2h + – – –
D
% FN-f–EGFP colocalized with mCherry–Rab5
0.0 20.0 40.0 60.0 80.0 100.0
****
****
Dynasore – + –
Rab5DN(S34N) – – +
FN7-10-EGFP 2h + + +
E
FN7-10 overnight – + – + – + – +
Dynasore – – 40μM 60μM 80μM
MMP-13
MMP-2
FN7-10 30min – + – + – + – +
Dynasore – – 40μM 60μM 80μM
p-JNK
JNK2
p-cJun
t-cJun
p-ERK
t-ERK
p-p38
t-p38
β-tubulin
F
FN7-10 overnight – + – + – +
Rab5WT – – + + – –
Rab5DN – – – – + +
MMP-13
MMP-2
mCherry
Rab5
β-tubulin
G
FN7-10 30min – + – + – +
Rab5WT – – + + – –
Rab5DN – – – – + +
p-JNK
JNK2
p-cjun
t-cjun
p-ERK
t-ERK
p-p38
t-p38
mCherry
Rab5
β-tubulin

Figure 2.11 Integrin endocytosis regulates MAP kinase signaling and MMP-13 production in response to FN7-10.

(**A**) Representative laser scanning microscopy images of human chondrocytes nucleofected with plasmids expressing α5 integrin–EGFP (green) and mCherry–Rab5WT or dominant-negative mutant mCherry–Rab5DN(S34N) (red) treated with vehicle (PBS) or FN7-10 (1 µM) for 2 h, indicating that FN7-10-induced α5 integrin endocytosis is inhibited with Dynasore pretreatment (a dynamin inhibitor, 60 µM) or the expression of the dominant-negative mutant Rab5DN(S34N). Panels represent middle layers of representative cells (top panel), fluorescence intensity profiling (bottom left panel) along dashed lines of indicated regions (white boxed insets, top panel) showing the localization of α5 integrin–EGFP and mCherry–Rab5 under different conditions, and 3D images in *x*-*y* view (bottom right panel) (**B**) Representative laser scanning microscopy images of human chondrocytes nucleofected with plasmids expressing mCherry–Rab5WT or dominant-negative mutant mCherry–Rab5DN(S34N) (red) treated with EGFP fusion FN7-10 (FN7-10–EGFP, 1 µM, green) for 2 h, indicating that the internalization of FN7-10 is inhibited using Dynasore (60 µM) pretreatment or the expression of Rab5DN(S34N). Panels represent middle layers of representative cells (top panel), fluorescence intensity profiling (bottom left panel) along dashed lines of indicated regions (white boxed insets, top panel) showing the localization of FN7-10–EGFP and mCherry–Rab5 under different conditions, and three-dimensional images in *x*-*y* view (bottom right). (**C**) Quantification of the percentage of α5 integrin–EGFP colocalized with α5 integrin–mCherry. (**D**) Quantification of the percentage of FN7-10–EGFP colocalized with mCherry–Rab5. (**C** and **D**) Measurements were based on the reconstruction of *z*-stack confocal images from n = 30 cells per condition pooled from n = 2 independent donors. Boundaries of the boxplot indicate the 25th and 75th percentiles, the horizontal line across the box is the median, and whiskers show the minima and maxima, with each dot representing the percentage in one cell. One-way ANOVA followed by Tukey's test was employed for multiple group comparisons. $^{****}P < 0.0001$. (**E**) Immunoblot analysis of the dose-dependent inhibition of FN7-10-induced (1 µM) MAP kinase phosphorylation (30 min) and MMP-13 production (overnight, 18 h) using Dynasore (40, 60, or 80 µM, 1 h pretreatment). (**F**) Immunoblot analysis of the reduction in FN7-10-induced (1 µM) MMP-13 (overnight, 18 h) production with dominant-negative mutant Rab5DN(S34N) overexpression. (**G**) Immunoblot analysis of the reduction in FN7-10-induced (1 µM) MAP kinase phosphorylation (30 min) with dominant-negative mutant Rab5DN(S34N) overexpression. (**E**, **F**, and **G**) Data are representative of experiments using n = 4 independent donors. For media samples, MMP-2 was used as a loading control, as it was not altered by the stimuli or inhibitors tested. To quantify proteins from cell lysates, non-phosphorylated proteins were used as controls. PBS was used as the vehicle control. Scale bars, 1 µm (insets in **A and B**); otherwise, 5 µm.

2.2.3. Activation of α5β1 induces temporospatial ROS generation in chondrocytes as a result of redoxosome formation

To study the source of ROS downstream to the binding of α5β1 integrin to FN7-10, we first found that the membrane-permeable free radical scavenger Tempol (4-hydroxy-2,2,6,6-tetramethylpiperidine-1-oxyl) inhibited FN7-10-induced MMP-13 production and MAP kinase signaling in a dose-dependent manner (**Figure 2.12A**), consistent with previous studies showing a requirement for ROS in FN7-10-induced signaling (*39*, *134*).

Considering that mitochondria and Noxes are common endogenous sources of hydrogen peroxide, which plays a regulatory role in redox signaling, we employed adenoviral overexpression of antioxidant enzymes specifically targeted to peroxide production in the cytosol or in mitochondria. Our aim was to determine the site of hydrogen peroxide production induced by α5β1 activation. Expression of PRX2 which localizes to the cytosol (**Figure 2.12B)** or catalase also in the cytosol (cCAT) (**Figure 2.12C**) both inhibited FN7-10-induced MAP kinase signaling, whereas catalase that contains a mitochondrial targeting sequence (mCAT) showed no inhibition (**Figure 2.9D**). These observations suggest that a cytosolic source, rather than a mitochondrial source, of hydrogen peroxide is required for the activation of MAP kinase signaling in response to α5β1 activation by FN7-10.

These findings led to the hypothesis that Noxes are responsible for α5β1-induced ROS generation. The expression pattern of Nox isoforms is tissue dependent and can vary widely by cell type (*135*, *136*). We sought to determine whether a specific Nox isoform is responsible for α5β1 integrin mediated redox signaling. To this end, we first measured the expression of Nox isoform components in human chondrocytes and found that Nox2 and Nox4 were the most abundant Nox isoforms. Nox2 subunits, including p67phox (activator of the Nox2 complex), p47phox (organizer of the Nox2 complex), p40phox, and p22phox, were expressed in human chondrocytes (**Figure 2.13A**). In response to FN7-10, we also observed increased phosphorylation of p47phox (p-p47phox) in chondrocytes, indicating Nox2 activation (**Figure**

2.13B). We then used several pharmacological Nox inhibitors to determine whether Nox inhibition blocks α5β1-induced MMP-13 production and MAP kinase signaling in response to FN7-10. We found that the pan-Nox inhibitor VAS2870 (**Figure 2.13C**) and the Nox2-specific inhibitor gp91ds-tat (**Figure 2.13D**) prevented α5β1-induced MMP-13 production and signaling activation, whereas the dual Nox1 and Nox4 inhibitor GKT 137831 (**Figure 2.13E**) exhibited no effect, indicating that Nox2 was necessary to generate hydrogen peroxide for α5β1 integrin-mediated redox signaling.

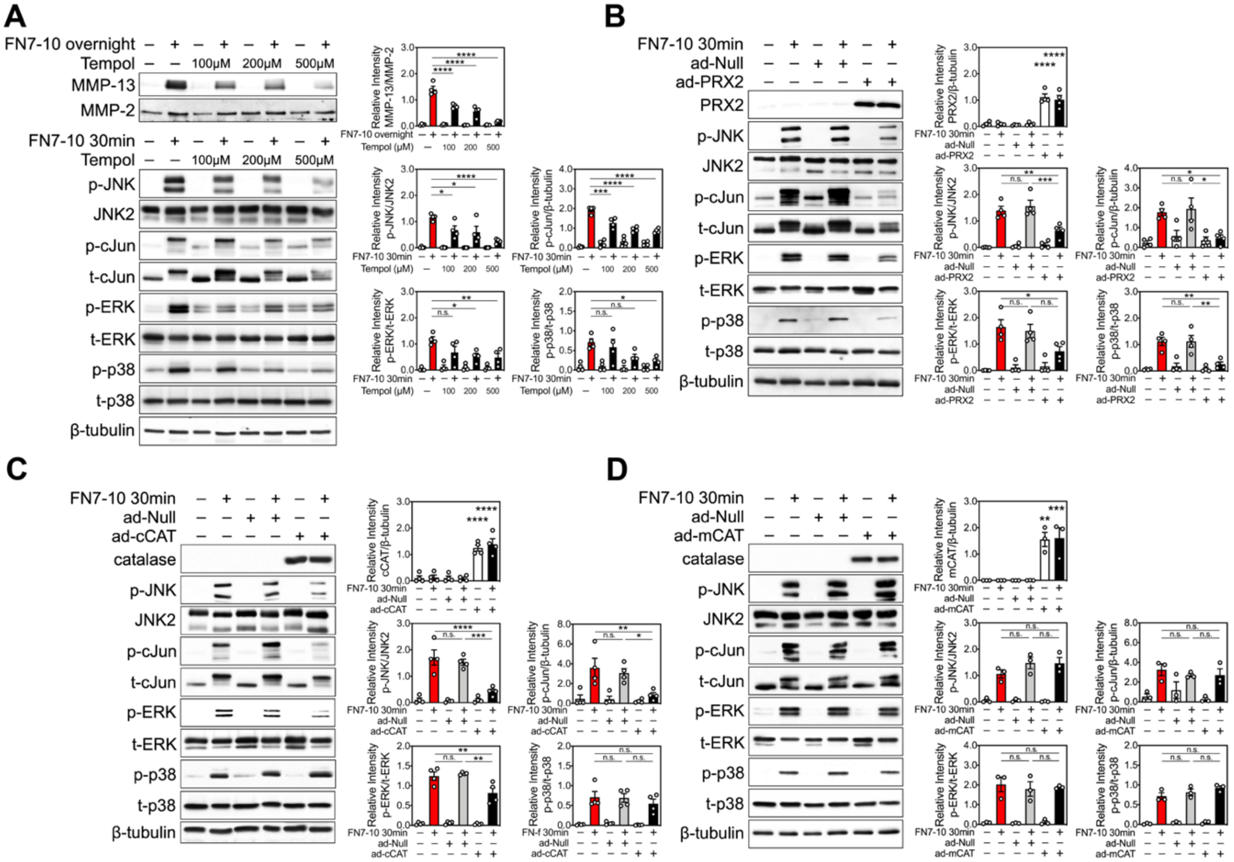

Figure 2.12 α5β1 activation that induces MMP-13 production and MAP kinase signaling requires cytosolic hydrogen peroxide.

(**A**) Immunoblot analysis and densitometric quantification of the dose-dependent inhibition of α5β1-mediated MMP-13 production and MAP kinase phosphorylation induced by FN7-10 (1 μM) using a membrane permeable antioxidant scavenger Tempol (100, 200, or 500 μM, 1 h pretreatment). Measurements were derived from n = 4 independent donors. (**B, C, and D**) Immunoblot analysis of the inhibition of α5β1-mediated MAP kinase phosphorylation using adenoviral vectors to overexpress PRX2 (**B**) or cytosolic catalase (cCAT) (**C**), while the overexpression of mitochondrial catalase (mCAT, (**D**) using an adenoviral vector had no effect. No virus and a null empty vector (ad-Null) transduction were used as controls. Densitometric quantification of the effect of adenoviral overexpression of PRX2 (**B**), cCAT (**C**), or mCAT (**D**) on α5β1-mediated MAP kinase phosphorylation. Measurements were derived from (**B** and **C**) n = 4 or (**D**) n = 3 independent donors. For media samples, MMP-2 was used as a loading control as it was not altered by the stimuli or inhibitors tested. Non-phosphorylated proteins were used as controls to measure MAP kinase activation. Data are mean fold change ± s.e.m band relative pixel intensity, arbitrary units. One-way ANOVA followed by Tukey's test was employed for multiple group comparisons. *$P < 0.05$, **$P < 0.01$, ***$P < 0.001$, ****$P < 0.0001$; n.s, not significant.

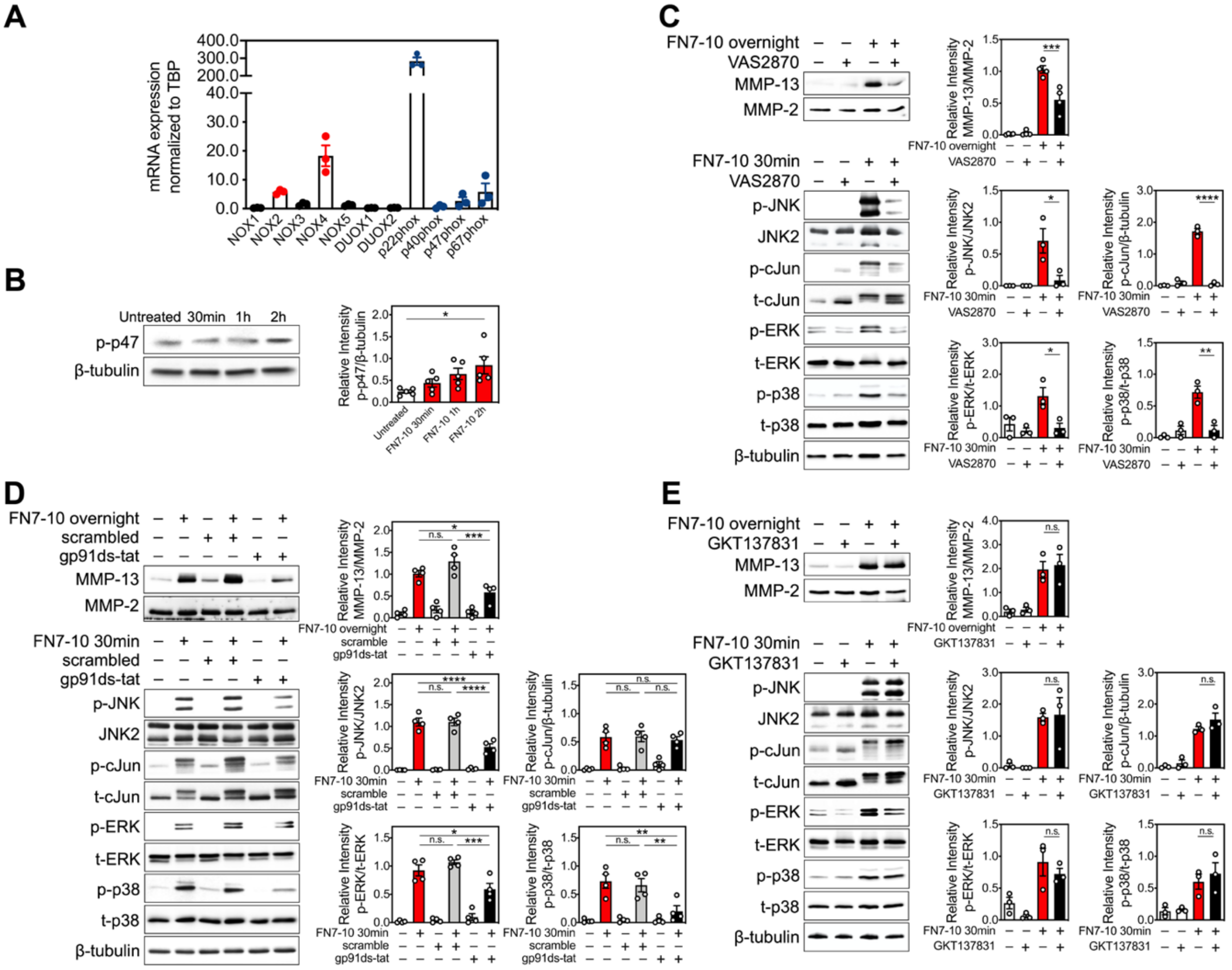

Figure 2.13 Integrin mediated stimulation of MAP kinases and MMP-13 production requires Nox2.

(**A**) qRT–PCR of Nox isoforms and Nox2 subunits in human articular chondrocytes. Gene expression was normalized to TATA-box binding protein (TBP) as a housekeeping control. Measurements were derived from n = 3 independent donors. (**B**) Immunoblot analysis and densitometric quantification show that α5β1 signaling in response to FN7-10 (1 µM) results in the phosphorylation of p47phox on Ser345 compared to the untreated control. Measurements were derived from n = 5 independent donors. (**C**) Immunoblot analysis and densitometric quantification of the reduction in α5β1-mediated MAP kinase phosphorylation (30 min) and MMP-13 production (overnight, 18 h) using the pan Nox inhibitor VAS2870 (VAS, 2 µM for MMP studies and 10 µM for cell signaling studies). Measurements were derived from independent donors, n = 4 for MMP studies and n =3 for cell signaling studies. (**D**) Immunoblot analysis and densitometric quantification of the reduction in α5β1-mediated-induced MAP kinase phosphorylation (30 min) and MMP-13 production (overnight, 18 h) using the Nox2-specific inhibitor gp91ds-tat (2 µM). Measurements were derived from n = 4 independent donors. (**E**) Immunoblot analysis and densitometric quantification of the reduction in α5β1-mediated MAP kinase phosphorylation (30 min) and MMP-13 production (overnight, 18 h) using the dual Nox1 and Nox4 inhibitor GKT137831 (20 µM). Measurements were derived from n = 3 independent donors. For media samples, MMP-2 was used as a loading control, as it was not altered by the stimuli or inhibitors tested. To quantify proteins from cell lysates, non-phosphorylated proteins were used as controls. PBS was used as the vehicle control. Data are presented as mean fold change ± s.e.m band relative pixel intensity, arbitrary units, compared by one-way ANOVA with Tukey's multiple comparisons test. $^{*}P < 0.05$, $^{**}P < 0.01$, $^{***}P < 0.001$, $^{****}P < 0.0001$; n.s., not significant.

Next, we sought to determine whether Nox2 is also localized to early endosomes during the course of integrin endocytosis in response to FN7-10. We hypothesized that the formation of redoxosomes, early endosomes that contain Noxes, would only occur in response to α5β1 binding of FN7-10 but not intact FN, and would correlate with the localization of hydrogen peroxide generation during integrin endocytosis. Chondrocytes co-transfected with α5 integrin–mCherry and EGFP–Nox2 were treated with vehicle, FN7-10, or intact FN followed by endogenous Rab5 immunolabelling to determine the colocalization of EGFP–Nox2 with $\text{Rab5}^{+}\alpha5$ integrin^{+} vesicles. We found that the colocalization of EGFP–Nox2 with $\text{Rab5}^{+}\alpha5$ integrin^{+} vesicles increased one hour after FN7-10 treatment and became more evident after two hours (**Figure 2.14, A and B**). To better visualize the temporospatial localization of Nox2 to early endosomes in response to α5β1 activation, chondrocytes were co-transfected with mCherry–Rab5CA(Q79L), together with EGFP–Nox2. We found that EGFP–Nox2 (**Figure 2.14C**) was gradually recruited to early endosomal compartments in response to FN7-10 but not vehicle or intact FN.

As indicated above, Nox4 is another major Nox isoform capable of producing hydrogen peroxide and is highly expressed in human chondrocytes. We co-transfected chondrocytes with α5 integrin–mCherry and Nox4–EGFP to determine whether Nox4-EGFP would also be recruited to $\text{Rab5}^{+}\alpha5$ integrin^{+} vesicles in chondrocytes. We found that neither FN7-10 nor intact FN promoted the colocalization of Nox4–EGFP with $\text{Rab5}^{+}\alpha5$ integrin^{+} vesicles (**Figure 2.15, A and B**), indicating that Nox4 is not present in FN7-10-induced redoxosomes. In chondrocytes co-transfected with Nox4–EGFP and mCherry–Rab5CA(Q79L), we did not observe recruitment of Nox4–EGFP to early endosomal compartments in response to FN7-10 (**Figure 2.15C**). This is consistent with the finding from the inhibitor studies that Nox4 was not required for α5β1-induced MMP-13 production or MAP kinase signaling in response to FN7-10.

Using antibodies to label endogenous Rab5 and the Nox2 component p67phox, we further confirmed that Nox2 containing early endosomes (redoxosomes) were formed following α5β1 integrin activation by FN7-10–EGFP (**Figure 2.14D**).

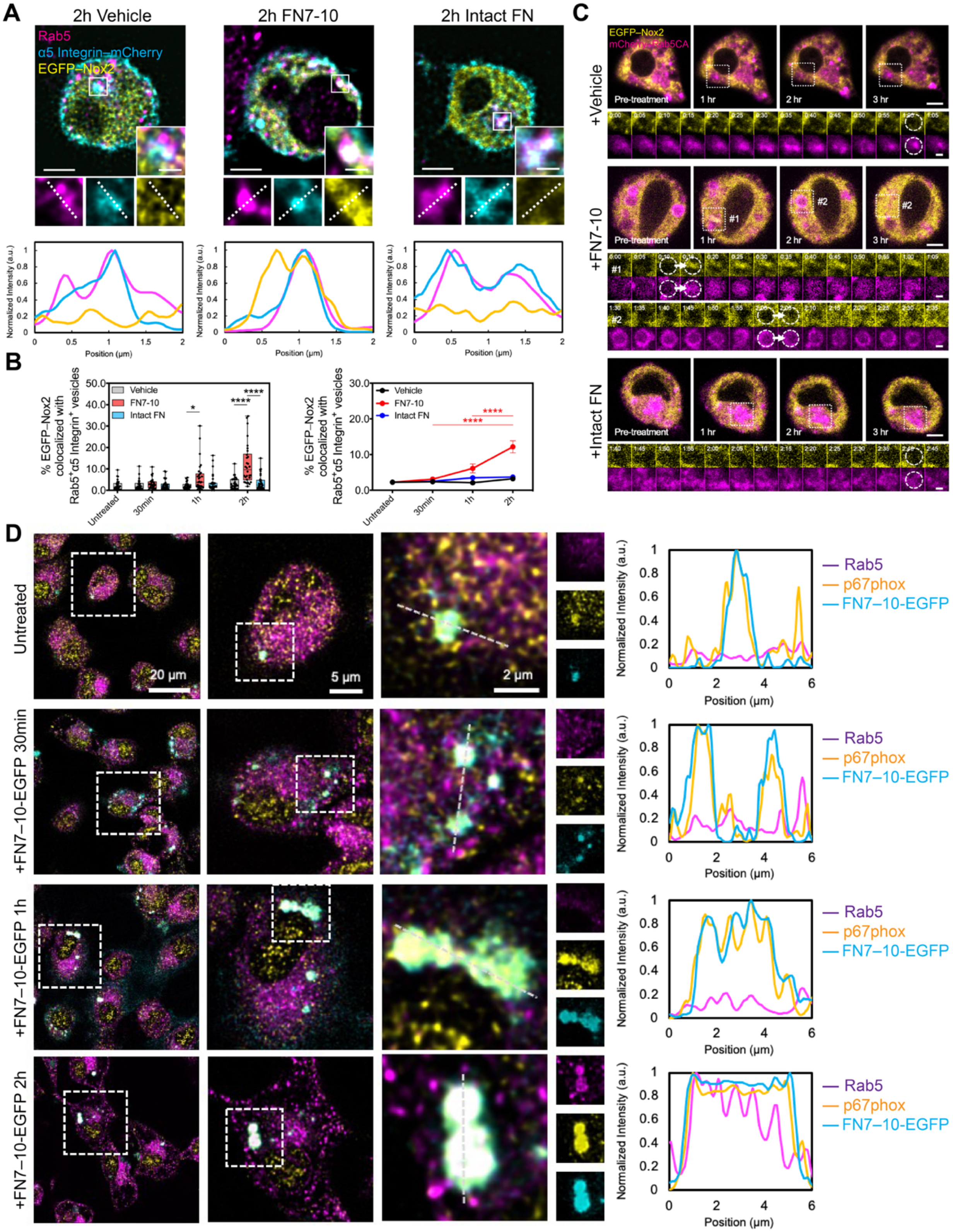
A
2h Vehicle
2h FN7-10
2h Intact FN
Rab5
α5 Integrin–mCherry
EGFP–Nox2
Normalized Intensity (a.u.)
Position (μm)
B
% EGFP–Nox2 colocalized with Rab5⁺α5 Integrin⁺ vesicles
Vehicle
FN7-10
Intact FN
Untreated
30min
1h
2h
*
****
C
EGFP–Nox2
mCherry–Rab5CA
+Vehicle
+FN7-10
+Intact FN
Pre-treatment
1 hr
2 hr
3 hr
#1
#2
D
Untreated
+FN7–10-EGFP 30min
+FN7–10-EGFP 1h
+FN7–10-EGFP 2h
20 μm
5 μm
2 μm
Normalized Intensity (a.u.)
Position (μm)
Rab5
p67phox
FN7–10-EGFP

Figure 2.14 α5β1 integrin activation by FN7-10 evokes redoxosomes formation containing Nox2.

(**A**) Representative laser scanning microscopy images of human chondrocytes nucleofected with plasmids expressing α5 integrin–mCherry (cyan) and EGFP–Nox2 (yellow) treated with vehicle (PBS, left panel), FN7-10 (1 μM, middle panel), or intact FN (10 μg/ml, right panel) for 2 h, followed by endogenous Rab5 immunolabeling (magenta). Magnification of the indicated regions (white boxed insets) and fluorescence intensity profiling along dashed lines showing that EGFP–Nox2 colocalizes with $Rab5^{+}α5$ $integrin^{+}$ vesicles in response to α5β1 activation by FN7-10 but not vehicle or intact FN. (**B**) Quantification of the percentage of EGFP–Nox2 colocalized with $Rab5^{+}α5$ $integrin^{+}$ vesicles was based on the reconstruction of *z*-stacks of confocal images from n = 30 cells per condition pooled from n = 2 independent donors. Boundaries of the boxplot (left panel) indicate the 25th and 75th percentiles, the horizontal line across the box is the median, and whiskers show the minima and maxima, with each dot representing the percentage in one cell. Data in the line graph (right panel) are presented as the mean ± s.e.m. Two-way ANOVA, considering both time and treatment and their interaction as factors, followed by Tukey's test was employed for multiple group comparisons across all possible pairwise comparisons. $^{*}P < 0.05$, $^{****}P < 0.0001$. (**C**) Live-cell images showing that in human chondrocytes nucleofected with plasmids expressing α5 integrin–mCherry (cyan) and EGFP–Nox2 (yellow), EGFP–Nox2 (yellow) is recruited to early endosomal compartments (indicated by mCherry–Rab5CA(Q79L) (magenta) in magnified white boxed regions of representative cells in response to FN7-10 (1 μM, middle panel), while no interaction between EGFP–Nox2 and early endosomal compartments was observed in response to either vehicle (PBS, top panel) or intact FN (10 μg/mL, bottom panel). Scale bars (**A and C**) represent 1 μm (insets in (**A**) or magnified images in (**C**)); otherwise, 5 μm. (**D**) Representative confocal images of immunostaining for endogenous Rab5 (magenta) and the Nox2 component p67phox (yellow) in human chondrocytes after indicated lengths of FN7-10–EGFP (1 μM, cyan) treatment. Fluorescence intensity profiling along dashed lines of indicated regions, showing that Nox2 containing redoxosomes are induced by FN7-10–EGFP. Scale bars in **D** represent 20 μm, 5 μm, and 2 μm as indicated.

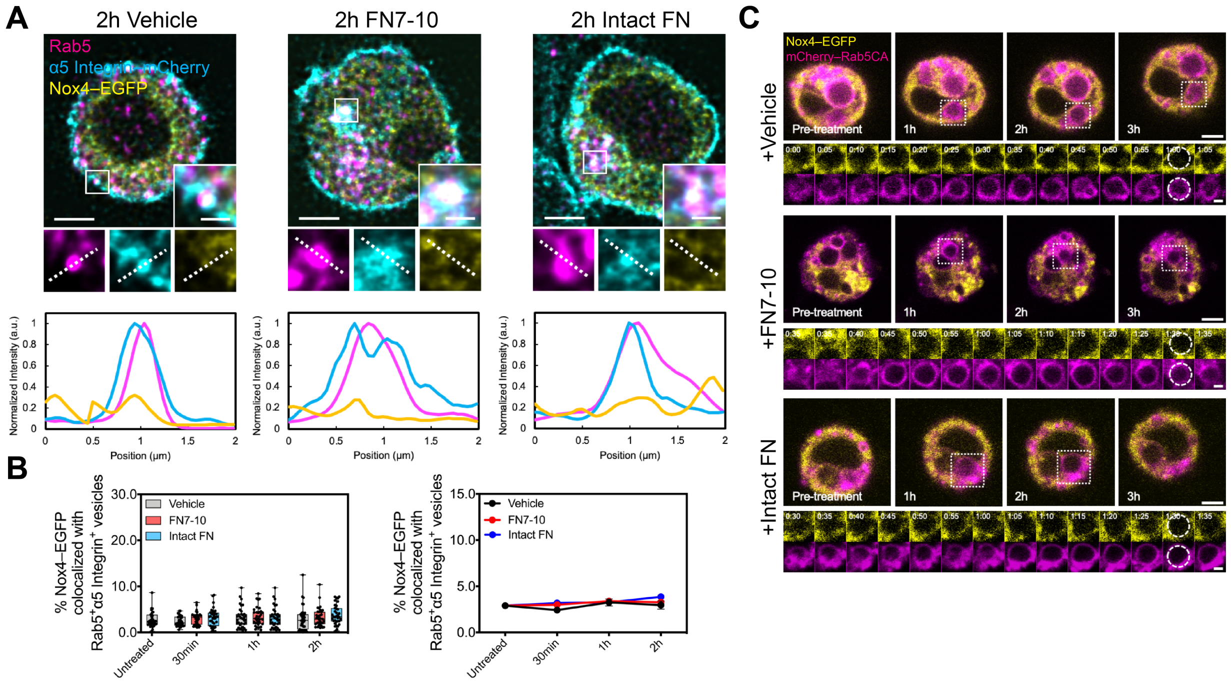

Figure 2.15 Nox4 is not recruited to early endosomes during integrin endocytosis in response to FN7-10.

(**A**) Representative laser scanning microscopy images of human chondrocytes nucleofected with plasmid constructs expressing α5 integrin–mCherry (cyan) and Nox4–EGFP (yellow) treated with vehicle (PBS, left panel), FN7–10 (1 µM, middle panel), or intact FN (10 µg/mL, right panel) for 2 h, followed by endogenous Rab5 immunolabelling (magenta). Magnification of the indicated regions (white boxed insets) and fluorescence intensity profiling along dashed lines indicating the absence of colocalization of Nox4–EGFP with Rab5$^+$α5 integrin$^+$ vesicles in all three conditions. (**B**) Quantification of the percentage of Nox4–EGFP colocalized with Rab5$^+$α5 integrin$^+$ vesicles was based on the reconstruction of *z*-stacks of confocal images from n = 35 cells per condition pooled from n = 2 independent donors. Boundaries of the boxplot (left panel) indicate the 25th and 75th percentiles, the horizontal line across the box is the median, and whiskers show the minima and maxima, with each dot representing the percentage in one cell. Data in the line graph (right panel) are presented as the mean ± s.e.m. Two-way ANOVA, considering both time and treatment and their interaction as factors, followed by Tukey's test was employed for multiple group comparisons across all possible pairwise comparisons. (**C**) Live-cell images showing that Nox4–EGFP (yellow) is not recruited to early endosomes (indicated by mCherry–Rab5CA(Q79L) (magenta) in response to vehicle (PBS, top panel), FN7-10 (1 µM, middle panel), or intact FN (10 µg/mL, right panel. Scale bars represent 1 µm (insets in (**A**) or magnified images in (**C**)); otherwise, 5 µm.

We then utilized three constructs, HyPer3–tk (contains a KRAS C-terminal sequence fusion of HyPer3 that localizes to the plasma membrane), cytoplasmic HyPer3, and HyPer3–Rab5 (contains a Rab5 sequence fused to the C-terminus of HyPer3 that localizes to the early endosome), to detect hydrogen peroxide generation at the plasma membrane, cytosol and early endosome (*122*). Live-cell, time-lapse imaging indicated that H_2O_2 was detected initially at the plasma membrane within 10 minutes of α5β1 integrin activation with FN7-10 (**Figure 2.16A and movie S1**), followed by detection of cytosolic (**Figure 2.16B**) and early endosomal H_2O_2 generation (**Figure 2.16C**). Intact FN, however, did not increase the intensity of either biosensor (**Figure 2.17**), indicating that α5β1 binding of intact FN does not evoke H_2O_2 generation, consistent with its lack of stimulation of MMP-13 production (**Figure 2.4, A and B**) and MAP kinase signaling (**Figure 2.4C**). Together, these observations suggest that Nox2-containing redoxosomes are formed in response to α5β1 integrin activation to localize and sustain intracellular redox signaling that begins at the plasma membrane and then becomes localized to redoxosomes.

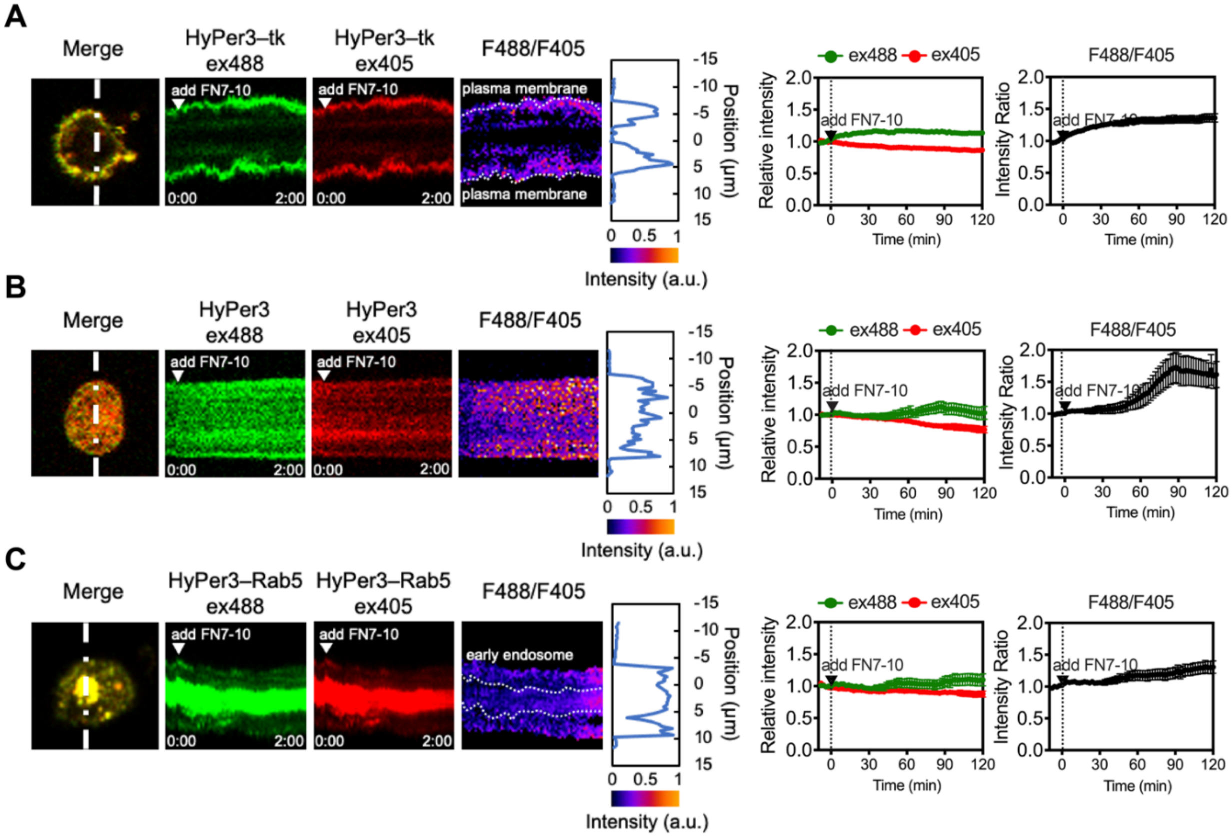

Figure 2.16 Temporospatial hydrogen peroxide generation induced after α5β1 activation by FN7-10.

Human chondrocytes were transfected with plasmid constructs expressing Hyper3–tk (Hyper3 fusion with the minimal KRAS C-terminal membrane anchor) (**A**), Hyper3 (**B**), or HyPer3–Rab5 (Hyper3 fusion with Rab5, a small GTP-binding protein localized on early endosomes) (**C**) and were subjected to live-cell, time-lapse imaging to measure hydrogen peroxide generation from the plasma membrane, cytosol, and early endosomes in response to α5β1 activation by FN7-10. Kymographs indicate the fluorescence intensity change for each Hyper3 construct at 488 nm excitation (ex488, green), 405 nm excitation (ex405, red), and pseudocolored ratio F488/F405 along the white dashed line. Arrows indicate the addition of FN7-10. The line profile (blue curve, right) corresponds to the F488/F405 intensity ratio across the dashed line on the last frame (120 min after the addition of FN7-10). The graphs show the means of relative fluorescence intensity at 488 nm excitation (green curve) and 405 nm excitation (red curve) and F488/F405 after the addition of FN7-10. Measurements to monitor hydrogen peroxide from the plasma membrane using HyPer3–tk were derived from n = 75 cells from n = 3 independent donors. (**A**). Measurements to monitor hydrogen peroxide from the cytosol using HyPer3 were derived from n = 38 cells from n = 3 independent donors (**B**). Measurements to monitor hydrogen peroxide from the cytosol using HyPer3–Rab5 were derived from n = 48 cells from n = 3 independent donors (**C**). Live-cell time-lapse imaging was performed at 2 min per frame with FN7-10 being added after the fifth scan (10 min) and was recorded over the course of 120 min following the treatment for a total of 65 frames. The baseline intensity or intensity ratio was determined by the average intensity of the first five frames before the treatment and normalized to 1. Data are presented as mean ± s.e.m arbitrary units.

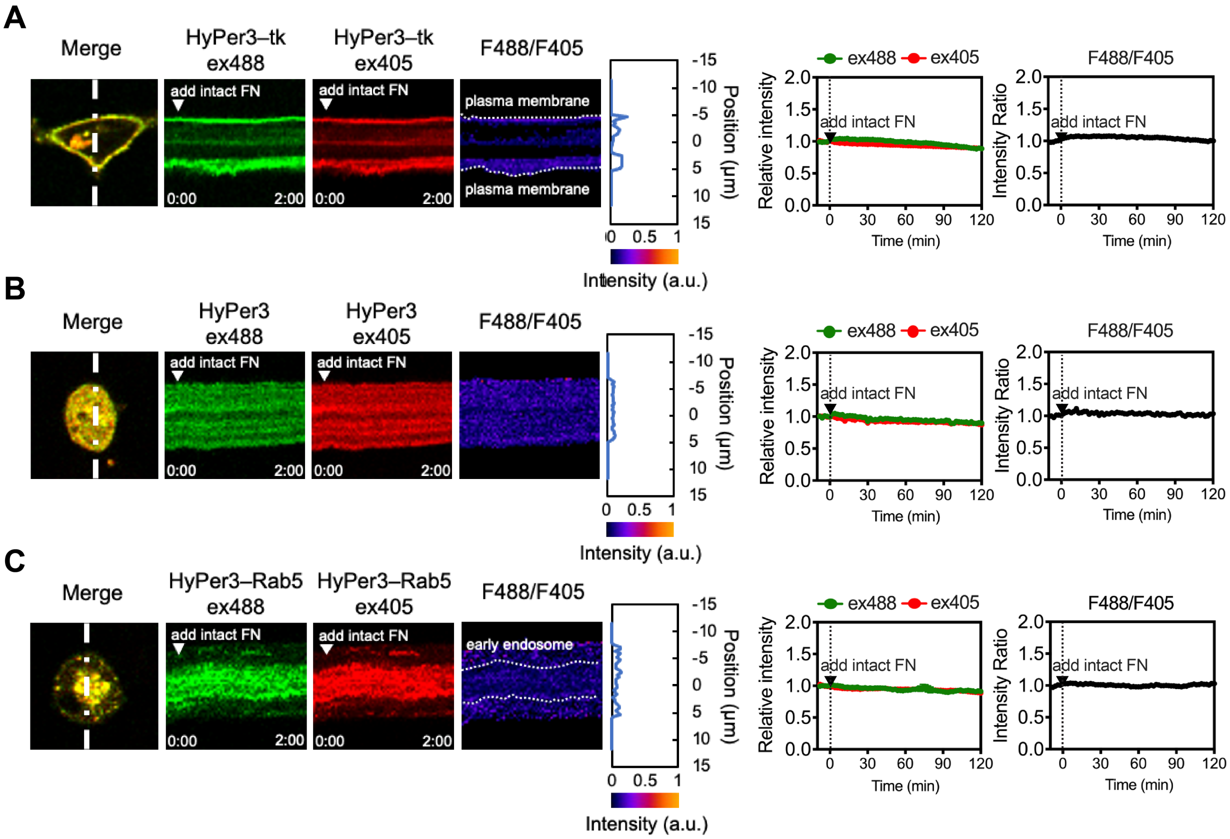

Figure 2.17 α5β1 binding of intact FN does not evoke hydrogen peroxide generation.

Human chondrocytes expressing Hyper3–tk (Hyper3 fusion with the minimal KRAS C-terminal membrane anchor) (**A**), Hyper3 (**B**), HyPer3–Rab5 (Hyper3 fusion with Rab5, a small GTP-binding protein localized on early endosomes) (**C**) were subjected to live-cell, time-lapse imaging to measure hydrogen peroxide generation from the plasma membrane, cytosol, and early endosome in response to intact FN (10 µg/ml), respectively. Kymographs indicate the fluorescence intensity change for each Hyper3 construct at 488 nm excitation (ex488, green), 405 nm excitation (ex405, red), and pseudocolored ratio F488/F405 along the white dashed line. Arrows indicate the addition of FN7-10. The line profile (blue curve, right) corresponds to the F488/F405 intensity ratio across the dashed line on the last frame (120 min after the addition of FN7-10). The graphs show the means of relative fluorescence intensity at 488 nm excitation (green curve) and 405 nm excitation (red curve) and F488/F405 after the addition of intact FN. Measurements to monitor hydrogen peroxide from the plasma membrane using HyPer3–tk were derived from n = 83 cells from n = 2 independent donors. (**A**). Measurements to monitor hydrogen peroxide from the cytosol using HyPer3 were derived from n = 40 cells from n = 2 independent donors (**B**). Measurements to monitor hydrogen peroxide from the cytosol using HyPer3–Rab5 were derived from n = 41 cells from n = 2 independent donors (**C**). Live-cell time-lapse imaging was performed at 2 min per frame with intact FN being added after the fifth scan (10 min) and was recorded over the course of 120 min following the treatment for a total of 65 frames. The baseline intensity or intensity ratio was determined by the average intensity of the first five frames before the treatment and normalized to 1. Data are presented as mean ± s.e.m arbitrary units.

2.2.4. Signaling redoxosomes transmit and sustain integrin redox signaling in osteoarthritis

Our previous studies demonstrated that α5β1 activation by FN7-10 increases Src activation through cysteine thiol oxidation, which is required for MMP-13 production (*39*). Src activation is tightly coupled with its sub-cellular location (*137*, *138*). Since redox signaling is strongly dependent on spatial confinement, we sought to determine whether Src is localized to redoxosomes in response to α5β1 integrin activation with FN7-10 (*123*). We treated chondrocytes co-expressing mCherry–Rab5CA(Q79L) and α5 integrin–EGFP with vehicle, FN7-10, and intact FN. Endogenous c-Src was then immunolabelled to determine whether Src endosomal relocation is associated with α5 integrin endocytosis. We observed that Src colocalized with α5 integrin–EGFP associated with early endosomes after FN7-10 treatment, while vehicle or intact FN had no effect (**Figure 2.18, A to C**), indicating that Src is recruited to early endosomes to further transmit and sustain integrin signaling during the course of FN7-10-induced integrin endocytosis. To further confirm Src endosomal translocation in response to α5β1 activation by FN7-10, we co-transfected chondrocytes with c-Src–EGFP and mCherry–Rab5CA(Q79L) to visualize the temporospatial translocation of Src via live-cell imaging. The addition of the fluorescence tag on the c-Src fusion protein was previously reported to retain key features of endogenous Src, including its spatial distribution, activation, and protein interactions (*138*, *139*). We found that c-Src–EGFP gradually translocated to the early endosomal compartment in response to α5β1 integrin activation with FN7-10, whereas far fewer interactions between Src and early endosomal compartments were observed for the cells treated with vehicle or intact FN (**Figure 2.18, D and E**).

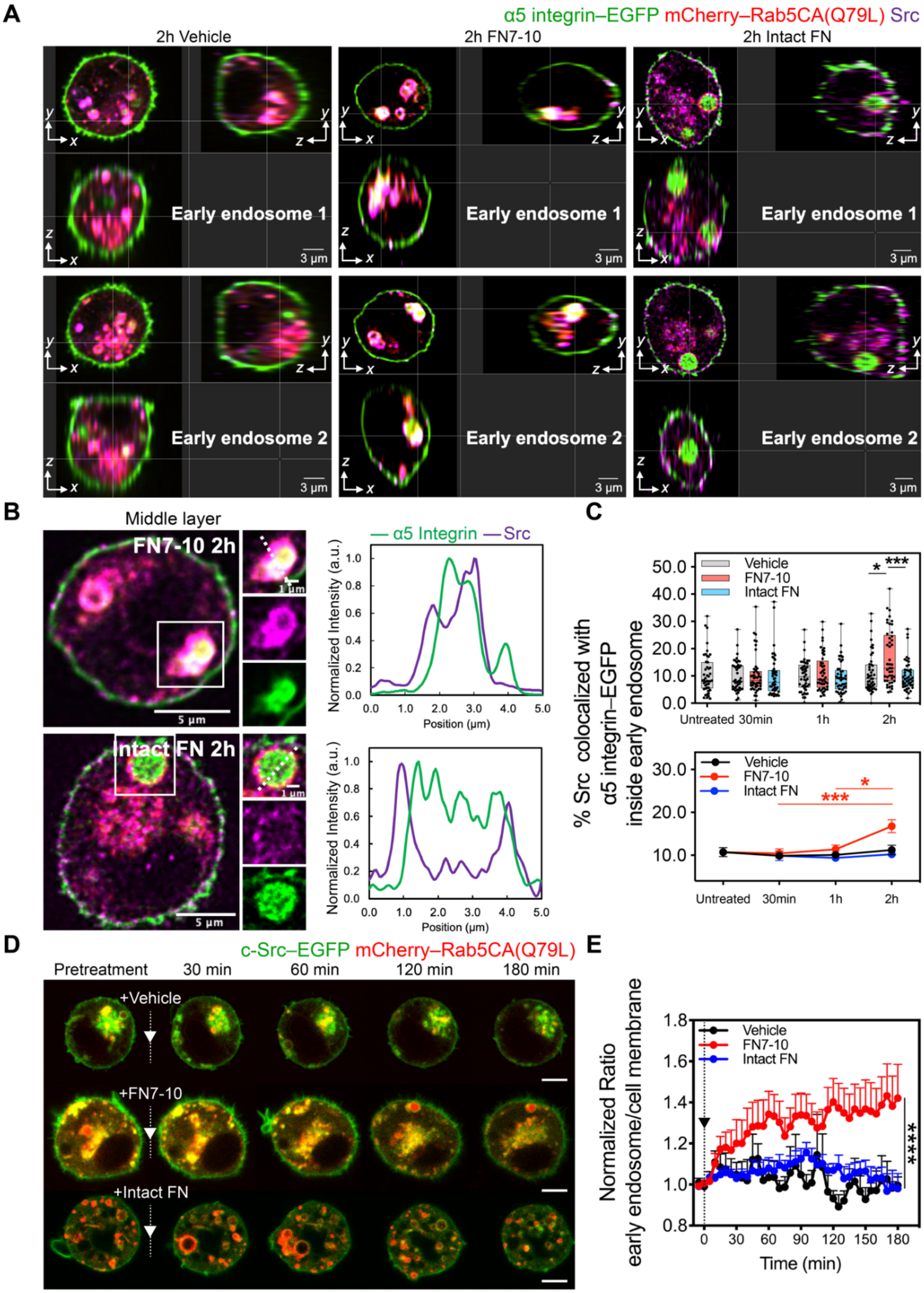
A
α5 integrin–EGFP mCherry–Rab5CA(Q79L) Src
2h Vehicle
2h FN7-10
2h Intact FN
Early endosome 1
Early endosome 2
y
x
z
3 μm
B
Middle layer
FN7-10 2h
Intact FN 2h
5 μm
1 μm
— α5 Integrin — Src
Normalized Intensity (a.u.)
Position (μm)
C
Vehicle
FN7-10
Intact FN
% Src colocalized with α5 integrin–EGFP inside early endosome
Untreated
30min
1h
2h
*
***
D
c-Src–EGFP mCherry–Rab5CA(Q79L)
Pretreatment
30 min
60 min
120 min
180 min
+Vehicle
+FN7-10
+Intact FN
E
Normalized Ratio early endosome/cell membrane
Time (min)
Vehicle
FN7-10
Intact FN
****

Figure 2.18 Endosomal trafficking of Src in response to α5β1 activation by FN7-10.

(**A**) Orthogonal view of representative laser scanning microscopy images of human chondrocytes nucleofected with plasmid constructs expressing α5 integrin–EGFP (green) and mCherry–Rab5CA(Q79L) (red) treated with vehicle (PBS, left panel), FN7-10 (1 μM, middle panel), or intact FN (10 μg/mL, right panel) for 2 h followed by endogenous Src immunolabelling (magenta). (**B**) Middle layers of representative laser scanning microscopy images of human chondrocytes expressing α5 integrin–EGFP (green) and mCherry–Rab5CA(Q79L) (red) treated with FN7-10 (1 μM, top panel) or intact FN (10 μg/mL, bottom panel) for 2 h followed by endogenous Rab5 immunolabelling (magenta). Fluorescence intensity profiling along dashed lines of white boxed regions indicating the localization of Src and α5 integrin–EGFP inside early endosomal compartments. (**C**) Quantification of the percentage of Src colocalized with α5 integrin inside mCherry–Rab5(Q79L) early endosomes was based on the reconstruction of *z*-stacks of confocal images from n = 45 cells per condition and n = 2 independent donors. Boundaries of the boxplot indicate the 25th and 75th percentiles, the horizontal line across the box is the median, and whiskers show the minima and maxima, with each dot representing the percentage in one cell. Two-way ANOVA, considering both time and treatment and their interaction as factors, followed by Tukey's test was employed for multiple group comparisons across all possible pairwise comparisons. $^{*}P < 0.05$, $^{**}P < 0.01$, $^{***}P < 0.001$. (**D**) Live-cell images of human chondrocytes nucleofected with plasmid constructs expressing c-Src–EGFP (green) and mCherry–Rab5CA(Q79L) (red) in response to vehicle (PBS, top panel), FN7-10 (1 μM, middle panel), or intact FN (10 μg/mL, bottom panel), indicating that c-Src–EGFP enters early endosomes in response to FN7-10 but not PBS vehicle or intact FN. Scale bars, 5 μm. (**E**) Ratiometric analysis measuring the mean intensity ratio of c-Src–EGFP in the early endosome compared to the cell membrane across the 180 min imaging period. The baseline intensity ratio was determined by the average intensity ratio of the first two frames before the treatment and normalized to 1. Measurements were derived from n = 3 cells from n = 2 independent donors for vehicle; n = 7 cells from n = 3 independent donors for FN7-10; n = 5 cells from n = 2 independent donors for intact FN. Data are presented as mean ± s.e.m arbitrary units, compared by one-way ANOVA followed by Tukey's test for multiple group comparisons. $^{****}P < 0.0001$. Scale bars, 3 μm in **A**; 1 μm in magnified images in **B**; otherwise, 5 μm as indicated.

We then used human cartilage samples to examine whether signaling redoxosomes are present in chondrocytes in vivo in areas of matrix damage. We first performed immunohistochemical staining to compare Rab5, p67phox, and Src levels among normal cartilage and osteoarthritic cartilage, including damaged and less damaged sites. Safranin O/fast green staining, which detects matrix damage and loss, was performed to confirm the differences in the severity of matrix damage in the tissue being analyzed (**Figure 2.19A**). We found that approximately 40% of the cells stained positively for Rab5 in normal cartilage, compared to 87% in lesion sites and 57% in adjacent non-lesion sites in osteoarthritic cartilage (**Figure 2.19, B and E**). Regarding the presence of p67phox, approximately 38% of the cells stained positively in normal cartilage, compared to 77% in lesion sites and 53% on adjacent non-lesion sites in osteoarthritic cartilage (**Figure 2.19, C and F**). There was also increased Src staining observed in osteoarthritic cartilage, as approximately 27% of the cells stained positively in normal cartilage, compared to 60% in lesion sites and 30% on adjacent non-lesion sites in osteoarthritic cartilage (**Figure 2.19, D and G**).

We further assessed bulk RNA-seq data from two published studies GSE114007 (*140*), which included 18 normal and 20 OA human knee cartilage tissues, and GSE168505 (*141*), which included 3 samples of normal cartilage and 4 samples of OA cartilage. Gene set enrichment analysis (GSEA) showed that, compared with normal cartilage, differential gene expression in OA samples was related to ECM-receptor interaction, highlighting the potential role of integrins in mediating the interaction between cartilage matrix and chondrocytes during the development of OA (**Figure 2.19, H and I**). In both bulk RNA-seq datasets, *RAB5C* and *CYBB* (codes for Nox2) were significantly higher in OA samples. *NCF2* (codes for p67phox) was highly expressed in OA samples in GSE114007; a similar expression pattern was found in GSE168505, although the difference was not significant (**Figure 2.19, H and I**). This might be due to the small sample size of the latter dataset. From a single-cell RNA-seq dataset that included 10 OA patients in GSE104782 (*142*), we observed consistent high-expression profiles for *RAB5C* and *NCF2* in chondrocytes from late-stage OA compared to early-stage OA (**Figure 2.19, J and K**). Finally, immunofluorescence staining confirmed that in osteoarthritic cartilage, especially at damaged sites where chondrocytes typically exist in clusters, the colocalization of both p67phox (**Figure 2.20A**) and Src (**Figure 2.20B**) with Rab5 was significantly greater. These results indicate that redoxosomes are formed during osteoarthritis pathogenesis that are capable of transmitting and sustaining redox signaling that can promote further matrix damage (**Figure 2.20C**).

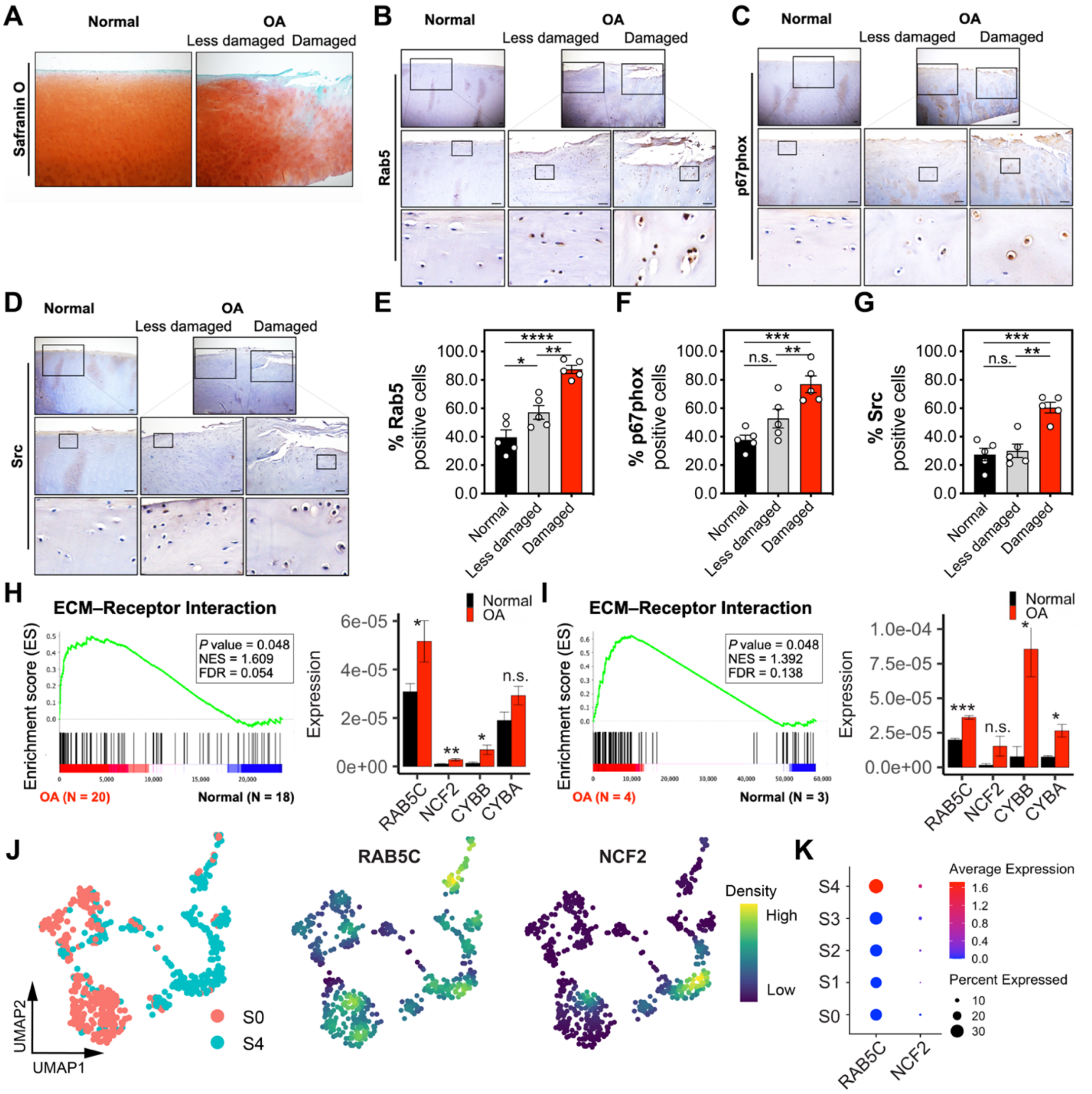

Figure 2.19 Increased Rab5, p67phox, and Src levels in human osteoarthritic cartilage.

(A) Safranin orange and fast green staining of human cartilage tissue from the femoral condyle indicating the difference in cartilage matrix loss among normal cartilage from tissue donors (left) and damaged and less damaged areas of cartilage from the same OA donor removed during arthroplasty (right). (**B**–**D**) Immunohistochemistry staining of Rab5 **(B)**, p67phox (**C**), and Src (**D**). Panels present low-magnification (4 ×, top) and high-magnification images of the boxed area above (10 ×, middle; 20 ×, bottom). Images are representative of n = 5 independent donors for both normal and OA. (**E**–**G**) Quantification of immunohistochemistry staining. There were n = 9 randomly selected distinct fields at 10 × magnification per donor assessed for different conditions, across normal and less damaged or damaged osteoarthritic cartilage, from at least three sections (30 μm apart). Image analysis was performed in a blind manner. Data are the mean ± s.e.m, with each dot representing the percentage in one donor. Two-sided Student’s t-tests were used to compare the difference between normal and OA cartilage. Paired t-tests were used to compare the difference between less damaged and damaged areas. (**H** and **I**) In both bulk RNA-seq datasets GSE114007 (**H**) and GSE168505 (**I**), gene set enrichment analysis (GSEA) showing that, compared with normal cartilage, OA samples possess gene expression related to ECM-receptor interaction (left); bar plots showing that *RAB5C* and *CYBB* (codes for Nox2) expression were significantly higher in OA samples compared to normal (right). Statistic test: two-sided Student's t-tests. (**J**) UMAP plots showing stage information (S) and expression density of *RAB5C* and *NCF2* (codes for p67phox) of OA chondrocytes in a single-cell RNA-seq dataset (GSE104782). (**K**) Dot plot showing *RAB5C* and *NCF2* (codes for p67phox) expression in different stages of OA chondrocytes from GSE104782. Consistent high-expression profiles for *RAB5C* ($P = 0.045$, comparing S4 to S0) and *NCF2* (codes for p67phox; $P = 0.044$, comparing S4 to S0) in late-stage OA chondrocytes were observed. Statistical test: Wilcoxon rank sum test. *$P < 0.05$, **$P < 0.01$, ***$P < 0.001$, ****$P < 0.0001$; n.s., not significant. Scale bar, 100 μm.

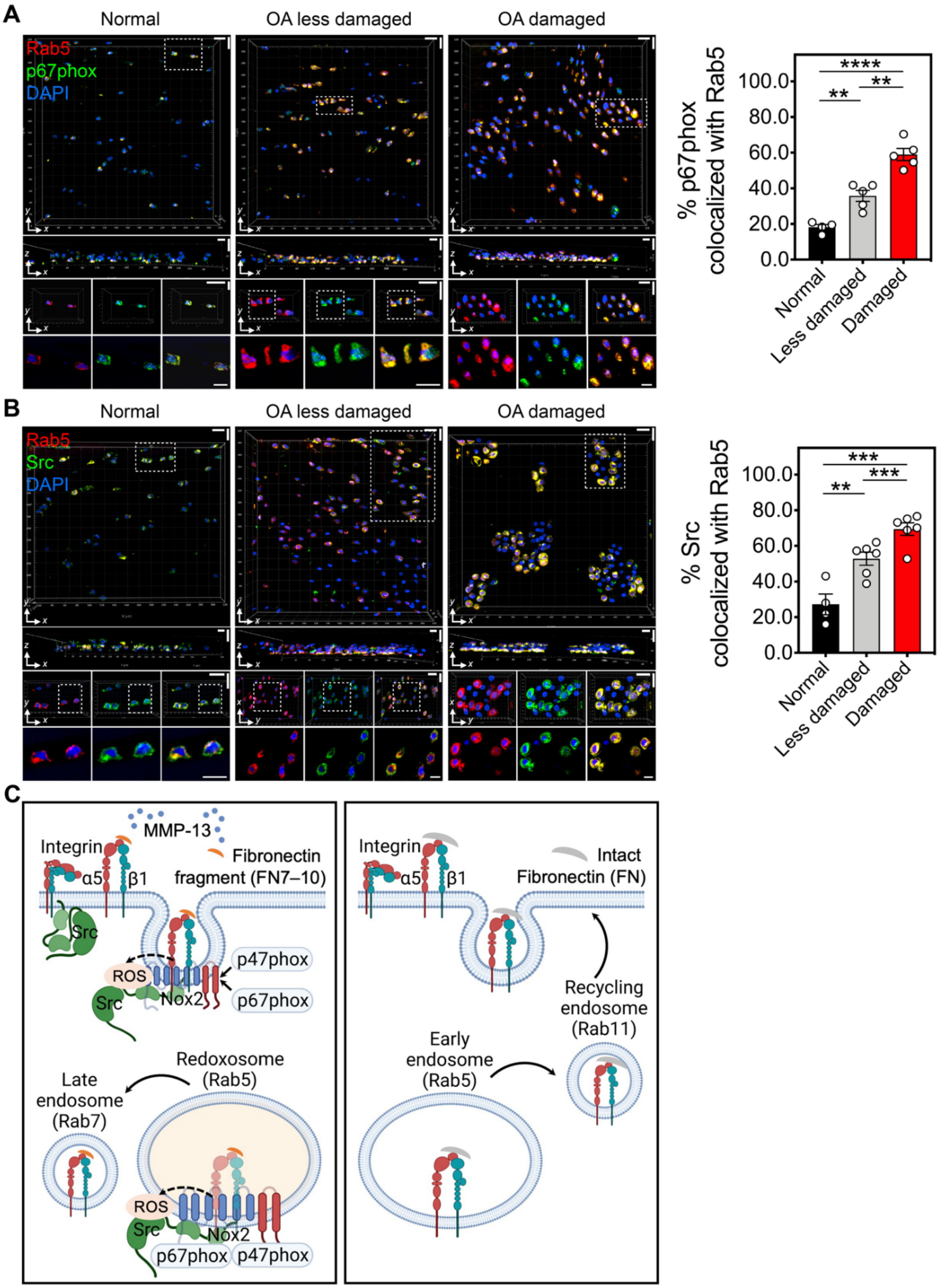
A
Normal
OA less damaged
OA damaged
Rab5
p67phox
DAPI
% p67phox colocalized with Rab5
100.0
80.0
60.0
40.0
20.0
0.0
****
**
**
Normal
Less damaged
Damaged
B
Normal
OA less damaged
OA damaged
Rab5
Src
DAPI
% Src colocalized with Rab5
100.0
80.0
60.0
40.0
20.0
0.0
***
***
**
Normal
Less damaged
Damaged
C
MMP-13
Integrin
α5
β1
Fibronectin fragment (FN7–10)
Src
p47phox
ROS
Nox2
p67phox
Src
Redoxosome (Rab5)
Late endosome (Rab7)
ROS
Src
Nox2
p67phox
p47phox
Integrin
α5
β1
Intact Fibronectin (FN)
Recycling endosome (Rab11)
Early endosome (Rab5)

Figure 2.20 Formation of signaling redoxosomes in human osteoarthritic cartilage.

Immunofluorescence images showing the presence of Rab5 (red) and p67phox (green) (**A**) and Rab5 (red) and Src (green) (**B**) in normal (left panel), less damaged (middle panel), and damaged (right panel) OA human cartilage. Nuclei were stained with DAPI, as shown in blue. Panels represent a planar view of the *x*–*y* projection together with an axial view of the *x*–*z* projection (top panel), magnified regions of white dashed boxes on the *x*–*y* projection (middle panel), and middle layers of magnified regions (bottom panel). Quantification of the percentage of p67phox (**A**) or Src (**B**) colocalized with Rab5. Measurements were derived from independent donors, n = 4 for normal cartilage and n = 5 (**A**) or n = 6 (**B**) for osteoarthritic cartilage. Data are mean ± s.e.m, with each dot representing the mean percentage in each donor, compared by two-sided Student's t-tests to determine the difference between normal and osteoarthritic cartilage and paired t-tests to determine the difference between less damaged and damaged areas. Scale bars, 30 μm in top panels and 10 μm in middle and bottom panels in **A** and **B**. $^{**}P < 0.01$, $^{***}P < 0.001$, $^{****}P < 0.0001$. (**C**) Schematic summary depicting that the formation of Nox2- and Src- containing redoxosomes mediates α5β1 integrin signaling in response to FN7-10 and illustrating the different integrin intracellular trafficking routes induced in response to FN7-10 or intact FN. Schematic is not to scale.

2.3. Discussion

This study provides evidence that the α5β1 integrin utilizes redoxosomes to transmit and sustain signals that regulate MAP kinase and Src activation that leads to chondrocyte MMP production. The redoxosomes provide for temporospatial production of hydrogen peroxide via Nox2. Although integrin trafficking through endosomes has been shown to regulate a number of biological processes including cell signaling relevant to cell migration and tissue development (*103*, *108*), this study demonstrates a role for the formation of redoxosomes (redox-active endosomes) in response to integrin activation. Importantly, the formation of redoxosomes occurred when α5β1 was activated by FN7-10 and not intact FN which allowed for a differential response to the two α5β1 integrin ligands. This finding provides a new mechanism by which cells may sense and respond to a damaged matrix, represented by the presence of a FN fragment (FN7-10). Furthermore, trafficking of the α5 integrin-FN7-10 complex to Rab7-containing late endosomes, which would be capable of merging with lysosomes for degradation, could serve to both terminate the signaling and remove the fragmented matrix protein. Intact FN also stimulated α5 integrin endocytosis and, like FN7-10, was endocytosed into Rab5-positive early endosomes along with the β1 integrin subunit in the active conformation. This finding was consistent with a prior study in cancer cell lines that found FN7-10 was co-endocytosed with active β1 integrin (*143*). In contrast to FN7-10, we found intact FN was trafficked to Rab11-containing endosomes, which would be expected to recycle the integrin back to the plasma membrane (summarized in **Figure 2.20C**).

The localization of signaling complexes is of particular importance to sustain redox signaling. The abundance and rapid kinetics of intracellular antioxidants require ROS, such as hydrogen peroxide, to be produced within close proximity to redox-regulated signaling proteins (*88*, *125*). We observed that hydrogen peroxide generation occurred first at the plasma membrane and then was localized to the cytosol and Rab5 positive redoxosomes. In addition to Nox2, its subunit p67phox was localized to Rab5$^+$α5 integrin$^+$ vesicles in response to FN7-10 stimulation but not to intact FN. This is consistent with previous findings that Nox1 and Nox2 are the two major Nox isoforms present in redoxosomes (*130*, *135*, *144–147*) although in chondrocytes we found that Nox2 was much more abundant. Our inhibitor studies, which included the highly specific Nox2 inhibitor gp91ds-tat, combined with imaging of Nox2 components in endosomes also containing the α5 integrin, are consistent with Nox2 serving as the source of hydrogen peroxide in chondrocytes when α5β1 integrin is activated by FN7-10. The tyrosine kinase Src was also localized to the site of hydrogen peroxide production by Nox2. Src kinase activity is well known to be redox-regulated (*124*) and a prior study (*39*) identified that Src oxidation was induced in articular chondrocytes by FN7-10 and Src activation was required for the increased production of MMP-13.

3D imaging of human cartilage samples is challenging due to the dense matrix that contains collagen fibers that autofluorescence. Despite this we were able to use confocal imaging to detect redoxosomes in normal and osteoarthritic human cartilage which is a major advance. The finding that signaling redoxosomes containing Nox2 and Src were found at increased levels in human osteoarthritic cartilage, especially at sites of damaged matrix, supports a role for redox regulation of Src in OA. The importance of Src in OA is supported by previous studies demonstrating that Src inhibition reduced OA severity in a preclinical animal models (*148–150*).

Previously, degradation of FN at the cell surface by MT1-MMP (MMP-14) was found to promote its endocytosis by myofibroblasts (*151*). In that study, the nature of the FN fragments generated by MT1-MMP was not determined but, similar to the present study using FN7-10, endocytosis was found to be mediated by the α5β1 integrin. MMP-14, as well as MMP-1, MMP-3, MMP-13, and other proteases, including HtrA1, can degrade FN to form various sized fragments, some of which would be expected to contain the RGD cell binding sequence recognized by α5β1 (*116*, *129*). Fibronectin fragments have been shown to act as matrikines stimulating the chemotaxis of prostate cancer cells to the bone marrow via α5β1, and fragments including a 29 kDa N-terminal fragment of FN that promotes proteolytic cartilage degradation were also shown to bind to α5β1 integrin (*152*, *153*). A role for α5β1 integrin signaling in OA was further established by work demonstrating that conditional deletion of the α5 integrin subunit in joint tissues protected mice from surgically-induced cartilage damage and OA (*66*).

The ability of resident cells to remodel their extracellular matrix is critical to the repair of matrix damage. This requires removal and replacement of damaged matrix proteins with an intact matrix. One mechanism for the removal of damaged matrix is through further proteolytic digestion followed by phagocytosis by scavenger cells such as macrophages. (*100*, *151*, *154*, *155*). Articular cartilage, however, is well known to have poor intrinsic repair capacity (*156*). Cartilage lacks resident macrophages and does not have blood vessels by which macrophages can travel to the tissue. This poses a unique challenge for the removal of damaged matrix proteins in cartilage which could allow the build-up of matrix degradation products such as fibronectin fragments found in OA as well as RA cartilage (*99*, *111*, *116*, *128*, *157*). Although chondrocytes themselves may be capable of phagocytosis, they have been found to have limited phagocytic capacity, including when tested with fibronectin fragments, when compared to chondrogenic progenitor cells which are limited in number in adult cartilage (*158*). It is not clear if endocytosis would be sufficient to remove significant amounts of matrix protein fragments making it likely that accumulation of fragments in the pericellular environment that generate additional fragments through the upregulation of proteases would promote a feed-forward loop of matrix destruction as seen in OA. This is consistent with our finding that genes associated with ECM-receptor interactions are increased in OA cartilage as well as genes expressing components of redoxosomes.

A limitation of the present study was the focus on a single fibronectin fragment and a single cell type. The FN7-10 fragment was chosen because of its well-established binding to α5β1 integrin (*110*, *131*), which allowed us to study the role of integrin signaling. Additional studies would be needed to determine if other fibronectin fragments that bind to α5β1 follow a similar pathway, which seems likely. Articular chondrocytes were chosen because they are responsible for both the synthesis and degradation of cartilage extracellular matrix. They are the key cell type in which activation of catabolic activity contributes to cartilage destruction in osteoarthritis, a condition where new therapeutic targets are needed to halt the progression of this painful and disabling condition.

Taken together, our results identify that the non-phagocytic uptake of α5β1 integrin by chondrocytes after binding of the FN7-10 ligand leads to the formation of redoxosomes that serve to localize and sustain signaling that results in the production of MMP-13. This finding demonstrates how the production of hydrogen peroxide necessary for redox-mediated signaling in response to matrix damage is regulated and sustained with temporal and spatial precision. The presence of redoxosomes at increased levels in OA cartilage suggests they have a mechanistic role in vivo in the pathogenesis of OA. These findings, and studies demonstrating that endocytosis of pain receptors can be targeted therapeutically (*159*, *160*), indicate that selective delivery of endosomal-specific antioxidants or selective disruption targeting endosomal signaling may provide exciting therapies for osteoarthritis and many other degenerative diseases, which are beyond the reach of conventional therapies.

2.4. Materials and methods

2.4.1. Primary human articular chondrocyte isolation and cell culture

Normal human ankle joints (tali) from tissue donors who did not have a history of arthritis were provided by the Gift of Hope Organ and Tissue Donor Network (Itasca, IL, USA) through an agreement with Rush University Medical Center (Chicago, IL, USA). The tali were visually inspected for gross morphologic changes and graded using a modified Collins score of 0–4 (*161*). Only normal-appearing tali (grade = 0 or 1) were used. Cartilage dissection was performed without taking either adjacent tissues or the underlying bone. A sequential digestion was then conducted to isolate human articular chondrocytes, in which cartilage slices were first incubated with Dulbecco's modified Eagle's medium (DMEM)/Ham's F-12 medium (Thermo Fisher, cat. no. 11330) containing 0.2% (w/v) pronase (Millipore Sigma, cat. no. 53702) for 1 h. It was followed by an overnight digestion with continuous agitation using DMEM/Ham's F-12 supplemented with 5% fetal bovine serum (FBS, VWR Seradigm, cat. no. 97068-085) and 0.036% (w/v) collagenase P (Roche, cat. no. 54684821). Following sequential digestion, isolated primary human articular chondrocytes were counted and plated as high-density monolayers. The cells were cultured in DMEM/F12 supplemented with 10% FBS, 100 U/mL penicillin/streptomycin (Gibco, cat. no. 15140-122), 2.5 µg/mL amphotericin B (Millipore Sigma, cat. no. A2942), and 4 µg/mL gentamicin (Gibco, cat. no. 15750060) at 37 ℃ and 5% CO_2 for 5–7 days. Prior to experiments, the cells were serum-starved overnight.

2.4.2. Recombinant FN7-10 and FN7-10–EGFP generation

For the production of hexahistidine (6 × His) fusion recombinant human FN7-10 or EGFP tagged FN7-10 (FN7-10–EGFP) proteins, a single colony of pET15b-FN7-10 (obtained from Dr. Harold Erickson, Duke University, Durham, NC, USA) or pET11b-FN7-10–EGFP (produced by the UNC Animal Models Core, The University of North Carolina, Chapel Hill, NC, USA) transformed BL21(DE3) Escherichia coli competent cells (Thermo Fisher, cat. no. C601003) were inoculated and cultured overnight at 37 °C with shaking at 225 rpm in 5 mL of LB medium containing 100 µg/mL ampicillin (Millipore Sigma, cat. no. 171254). The overnight culture was then diluted in 500 mL of LB medium containing 100 µg/mL ampicillin and cultured at 37 °C with shaking at 225 rpm until the optical density (OD_{600}) reached 0.6, followed by 1 mM IPTG (Thermo Fisher, cat. no. PR-V3955) induction at 22 ℃ overnight with shaking at 225 rpm. Broth culture was then pelleted by centrifugation in a pre-cooled Beckman JLA–16.250 fixed-angle aluminum rotor (Beckman Coulter, product no. 363934) at 4,000 rpm for 10 min at 4 ℃. The pellet was resuspended in B-PER™ Bacterial Protein Extraction Reagent (10 mL per 250 mL LB medium, Thermo Fisher, cat. no. 78248) followed by high-speed centrifugation at 13,000 rpm for 30 min at 4 ℃ using a Beckman JA 30.50 Ti fixed-angle titanium rotor (Beckman Coulter, product no. 363420). The supernatant extract was kept cold and purified immediately. To purify recombinant protein samples, 1 mL Ni–NTA beads (Qiagen, cat. no. 30210) were prepared per 10 mL extract. After three cold 1 × PBS washes with 10 mM imidazole (10 × bead volumes, PBS and imidazole were diluted from 8 × phosphate buffer and 2.0 M imidazole stock supplemented by His Buffer Kit, Millipore Sigma, cat. no. GE11-0034-00), Ni–NTA beads were then mixed with supernatant extract and incubated at 4 ℃ for 2 h with rocking. This was followed by protein elution, in which recombinant FN7-10 or FN7-10–EGFP was released from Ni–NTA beads by competition with 500 mM imidazole (diluted from 2.0 M imidazole kit stock) incubation at 4 ℃ for 10 min with rocking, followed by two bead washes using cold 1 × PBS and one 70% isopropanol wash (Thermo Fisher, cat. no. BP2618500). After elution, the supernatant recombinant protein eluent was collected by centrifugation at 1,000 rpm for 2 min at 4 ℃. Dialysis was performed immediately to remove imidazole and other unwanted molecules from purified protein samples, in which Slide-A-Lyzer™ G2 Dialysis 3.5K molecular-weight cut off (MWCO) cassettes (Thermo Fisher, cat. no. 87724) were used, as recombinant human FN7-10 has a molecular weight of approximately 42 kDa. Endotoxin was then removed using Pierce™

High-Capacity Endotoxin Removal Spin Columns (Thermo Fisher, cat.no. 88276). After 2 h of end-over-end mixing with purified recombinant protein at 4 ℃, the column was centrifuged at 1,600 rpm for 1 min at 4 ℃ to collect the sample. Sodium dodecyl sulfate–polyacrylamide gel electrophoresis (SDS–PAGE) was performed followed by Coomassie blue staining (Bio-Rad, cat. no. 1610436 and 1610438) to assess the purity of the protein samples. The concentration of recombinant FN7-10 or FN7-10–EGFP was determined by the BCA method. Endotoxin-free recombinant protein samples were stored at −80 °C prior to use. The cells were treated with 1 μM FN7-10 overnight to analyze matrix metalloproteinase secretion in conditioned medium and with 1 μM FN7-10 or FN7-10–EGFP for the indicated period of time in signaling or endocytosis studies.

2.4.3. Intact fibronectin and chemical compounds

Purified fibronectin (FN) from human plasma used as intact FN (cat. no. F0895), TEMPO (2,2,6,6-tetramethylpiperidine 1-oxyl, cat. no. 214000), and VAS2870 (7-(1,3-benzoxazol-2-ylsulfanyl)-3-benzyl-3H-[1,2,3]triazolo[4,5-d]pyrimidine, cat. no. SML0273) were purchased from Millipore Sigma. Sgp91ds-tat, scrambled (H-YGRKKRRQRRRCLRITRQSR-NH2, cat. no. AS-63821) and gp91ds-tat (H-YGRKKRRQRRRCSTRIRRQL-NH2, cat. no. AS-63818) were purchased from Eurogentec. GKT137831 (2-(2-chlorophenyl)-4-[3-(dimethylamino)phenyl]-5-methyl-1H-pyrazolo[4,3-c]pyridine-3,6(2H,5H)-dione, cat. no. 17764) was purchased from Cayman Chemical Company. Dynasore (3-hydroxynaphthalene-2-carboxylic acid, Cat. No. 2897) was purchased from Tocris Bioscience. Chondrocytes were treated with serum-free cell culture medium containing the indicated concentrations of inhibitors for 1 h prior to FN7-10 stimulation.

2.4.4. Constructs

Expression vectors for the hydrogen peroxide reporter HyPer3, HyPer3–tk containing KRAS C-terminal sequence, and HyPer3–Rab5 containing RAB5A were generated and generously sent to us as gifts from R. Tsutsumi (Tohoku University, Sendai, Miyagi, Japan) and B. Neel (New York University, New York, NY, USA). The EGFP–Nox2 and Nox4–EGFP constructs were generated and generously provided as gifts from J.D. Van Bull (University of Amsterdam, Amsterdam, Netherlands), in which the full-length cDNAs encoding human NOX2 (EGFP–Nox2) or NOX4 (Nox4–EGFP) were subcloned into the pE-GFP–C1 or pE-GFP–N1 vector, respectively. c-Src–EGFP was generated by N. Yamaguchi (Chiba University, Chiba, Japan) and sent to us as a gift, in which cDNA encoding human c-Src was c-terminally tagged with EGFP into the pcDNA4/TO vector. The following plasmids were purchased from Addgene: α5 integrin–EGFP (cat. no. 15238, gift from R. Horwitz), α5 integrin–mCherry (cat. no. 54970, gift from M. Davidson), active Rab5 mutant mCherry–Rab5CA(Q79L) (cat. no. 35138, gift from S. Grinstein), active Rab7 mutant EGFP–Rab7CA(Q67L) (cat. no. 28049, gift from Q. Zhong). Expression vectors of mCherry-fused RAB5A (mCherry-Rab5, cat. no. 55126), RAB7A (mCherry–Rab5, cat. no. 55127), and RAB11A (mCherry–Rab11, cat. no. 55124) were deposited as gifts from M. Davidson, and mCherry-labelled dominant negative mCherry–Rab5DN(S34N) (cat. no. 35139, a gift from S. Grinstein). All constructs used in this study were verified by DNA sequencing.

2.4.5. Nucleofection

For nucleofections, isolated primary human articular chondrocyte monolayers were first cultured in 10 cm dishes (Corning, cat. no. 430167) seeded at high density for 2–3 days. Then, chondrocytes were digested in 10% FBS DMEM/Ham's F12 medium that contained 0.1% (w/v) pronase and 0.1% (w/v) collagenase P at 37 °C/5% CO_2 until all cells were dislodged, which resulted in a single cell suspension with no visible cell clumps or clusters. Pronase/collagenase digestion was facilitated by pipetting the cell suspension once per hour. The cells were centrifuged for 8 min at 688 rpm and washed once with 1 × PBS (Thermo Fisher, cat. no. 14190144). After PBS wash, 1.0e+06 chondrocytes per electroporation were resuspended with 100 µL of P3 Primary Cell 4D-Nucleofector X Kit S reagent (Lonza, cat. no. S-8904), in which nucleofector supplement (Lonza, cat. no. S-08962), and plasmid constructs were added and mixed by pipetting. Nucleofections were performed in Nucleocuvette cartridges provided by the P3 Primary Cell 4D-Nucleofector L Kit (Lonza, cat. no. V4XP-3024), in which samples covered the bottom of the cuvette with no air bubbles. After electroporation, human chondrocytes were cultured in DMEM/F12 media supplemented with 20% FBS at 37 °C/5% CO_2 in an incubator for 48 h before changing to serum-free conditions for the experiments.

2.4.6. Adenoviral transduction

The adenoviral construct encoding cytosolic catalase (cCAT) was purchased from the University of Iowa Viral Vector Core lab. The adenoviral construct encoding catalase targeted to the mitochondria (mCAT) was generously provided as a gift from Dr. Douglas Spitz (University of Iowa, Iowa City, IA, USA). The adenoviral construct encoding PRX2 was purchased from Vector Biolabs (cat. no. ADV-219769). An empty vector (ad-Null) (Cell Biolabs, cat. no. ADV-001) was used as a control to test the non-specific effects of adenoviral transduction. Upon reaching 60–70% confluency, primary human articular chondrocyte monolayers were incubated with serum-free DMEM/Ham's F-12 medium (Thermo Fisher, cat. no. 11330) media containing adenovirus (4.0e+08 viral particles/mL) and 1 M calcium chloride (25 µL/mL media) for 2 h at 37 °C/5% CO_2. Chondrocytes were then washed twice using serum-free DMEM/Ham's F-12 medium and cultured in 10% FBS DMEM/Ham's F-12 medium at 37 °C/5% CO_2 for 48 h, followed by experimental treatments. Transduction was confirmed through immunoblotting using total protein extracts from cultured cells.

2.4.7. Quantitative PCR

Total RNA was isolated from primary human articular chondrocytes using a QIAgen RNeasy mini kit (QIAgen, cat. no. 74004) and converted to cDNA using iScript™ Reverse Transcription Supermix for RT–qPCR (Bio-Rad, cat. no. 1708840) supplemented with oligo (dT) and random hexamer primers. RT–qPCR was performed on a QuantStudio 6 Flex Real-time PCR System (Thermo Fisher Applied Biosystems) using Bio-Rad iTaq™ Universal SYBR® Green Supermix (cat. no. 1725121). The following primers were used: TBP, 5’-TGCACAGGAGCCAAGAGT-3’ (forward) and 5’-CACATCACAGCTCCCCAC-3’ (reverse); NOX1, 5’- TTCAACAATTCCCAGGATTGAAGTGGATGGTC-3’ (forward) and 5’ GACCTGTCACGATGTCAGTGGCCTTGTCAA-3’ (reverse); NOX2, 5‘-GTCACACCCTTCGCATCCATTCTCAAGTCAGT-3’ (forward) and 5’-CTGAGACTCATCCCAGCCAGTGAGGTAG-3’ (reverse); NOX3, 5’-: ATGAACACCTCTGGGGTCAGCTGA-3’ (forward) and 5’-GGATCGGAGTCACTCCCTTCGCTG-3’ (reverse); NOX4, 5’-TCGCAGAAGGTTCCAAGCAG-3’ (forward) and 5’-ACTGAGAAGTTGAGGGCATTC-3’ (reverse); NOX5, 5’-ACTATCTGGCTGCACATTCG-3’ (forward) and 5’-ACACTCCTCGACAGCCTCTT-3’ (reverse); DUOX1, 5’-CGACATTGAGACTGAGTTGA-3’ (forward) and 5’- CTGGAATGACGTTACCTTCT-3’ (reverse); DUOX2, 5’-AACCTAAGCAGCTCACAACT-3’ (forward) and 5’-CAGAGAGCAATGATGGTGAT-3’ (reverse); p22phox, 5’-GGCGCTTCACCCAGTGGTACTTTGG-3’ (forward) and 5’-TAGGTAGATGCCGCTCGCAATGGC-3’ (reverse); p40phox, 5’-GCTTCACCAGCCACTTTGTT-3’ (forward) and 5’-TCCTGTTTCACACCCACGTA-3’ (reverse); p47phox, 5’-AGTCCTGACGAGACGGAAGA-3’ (forward) and 5’-GGACGGAAAGTAGCCTGTGA-3’ (reverse); p67phox, 5’- GGAGTGTGTCTGGAAGCAG-3’ (forward) and 5’-AGTGTGTAGGGCATGGGAA -3’ (reverse). The mRNA levels were normalized to those of TATA-box binding protein (TBP).

2.4.8. Immunoblotting

After aspirating the media from the cultures, the cells were washed twice with cold 1 × PBS on ice and lysed with lysis buffer (Cell Signaling Technology, cat. no. 9803) containing 20 mM Tris–HCl (pH 7.5), 150 mM NaCl, 1 mM Na_2EDTA, 1 mM EGTA, 1% Triton, 2.5 mM sodium pyrophosphate, 1 mM beta-glycerophosphate, 1 mM Na_3VO_4, and 1 µg/mL leupeptin, supplemented with phenylmethylsulfonyl fluoride (PMSF, Millipore Sigma, cat. no. 93482), and Halt™ Protease and Phosphatase Inhibitor Cocktail (Thermo Fisher, cat. no. 78440). The cells were scraped using pre-cooled plastic cell scrapers and collected in microfuge tubes followed by end-over-end rotation for 30 min at 4 °C. Tubes were then centrifuged at 15,000 rpm for 10 min at 4 °C to remove insoluble fractions. The concentration of soluble protein fractions collected from the supernatant was determined using the BCA method (Pierce™ BCA Protein Assay Kit, Thermo, cat. no. 23225). Samples with equal amounts of total protein (10–20 µg) combined with 4 × Laemmli Sample Buffer (Bio-Rad. cat. no. 1610747) containing 5% 2-mercaptoethanol (β-ME, Bio-Rad, cat. no. 1610710) were boiled for 5 min at 95 °C and cooled on ice before microcentrifugation for 5 min. Proteins and molecular weight markers (Precision Plus Protein™ Kaleidoscope™ Prestained Protein Standards, Bio-Rad, cat. no. 1610375) were then separated by 10% SDS–PAGE in Tris–glycine SDS running buffer (diluted from 10 × stock, Bio-Rad, cat. no. 1610772) for 90 min at 120 V and electrotransferred from the gel to a nitrocellulose membrane (Cytiva, cat. no. 10600001) in transfer buffer that contained 25 mM Tris (Thermo Fisher, cat. no. BP152-500), 192 mM glycine (Thermo Fisher, cat. no. BP381-500), 20% (v/v) methanol (Thermo Fisher, cat. no. A412P-4), and 0.1% (w/v) SDS (Bio-Rad, cat. no. 1610416) in deionized water for 70 min at 120 V. The membranes were blocked with 5% bovine serum albumin or nonfat dry milk in Tris-buffered saline with 0.1% Tween (TBST) for 1 h at room temperature and incubated with primary antibodies overnight at 4 °C. The membranes were then rinsed three times for 5 min each in TBST. Following HRP-linked secondary antibody incubation for 1 h at room temperature, membranes were developed with

ECL substrates (Azure Biosystems, cat. no. 190716) and visualized using an Azure Biosystems c600 imager (Azure Biosystems). To assess protein phosphorylation, immunoblotting was performed using phospho-specific antibodies. Blots were then stripped and re-probed with antibodies to target total proteins or β-tubulin as controls. For extracellular MMP-13 secretion analysis, conditioned medium was collected after overnight stimulation and used for immunoblotting. MMP-2 levels were not altered by the stimuli or inhibitors tested and so were used as a loading control for media samples. Densitometric analysis was performed using ImageJ/Fiji. The following antibodies for immunoblotting were used at diluted concentrations: antibodies against phospho-JNK (Thr183/Tyr185) (81E11) (1:1000, cat. no. 4668), JNK2 (56G8) (1:1000, cat. no. 9258), phospho-c-Jun (Ser73) (D47G9) (1:1000, cat. no. 3270), total c-Iun/c-Jun (60A8) (1:1000, cat. no. 9165), phospho-p44/42 MAPK (ERK1/2) (Thr202/Tyr204) (1:1000, cat. no. 9101), total ERK/p44/42 MAPK (ERK1/2) (1:1000, cat. no. 9102), phospho-p38 MAPK (Thr180/Tyr182) (1:1000, cat. no. 9211), total p38/p38 MAPK (1:1000, cat. no. 9212), mCherry (E5D8F) (1:1000, cat. no. 43590), Rab5 (C8B1) (1:1000, cat. no. 3547), and β-tubulin (1:1000, cat. no. 2146) were purchased from Cell Signaling Technology; antibodies against PRX2 (1:1000, cat. no. ab191535) and catalase (1: 1000, cat. no. ab48613) were purchased from Abcam; the antibody against phospho-p47phox (Ser345) (cat. no. PA5-37806) was purchased from Thermo Fisher; antibodies against MMP-2 (1:1000, cat. no. MAB3308) and MMP-13 (1:2000, cat. no. MAB3321) were purchased from Millipore Sigma; and HRP-conjugated secondary antibodies anti-rabbit IgG HRP-linked antibody (1:1500, cat. no. 7074) and anti-mouse IgG HRP-linked antibody (1:1500, cat. no. 7076) were purchased from Cell Signaling Technology. Densitometric analysis was performed using ImageJ/Fiji.

2.4.9. Fluorescent labeling of FN7-10 and intact FN

To fluorescently label FN7-10 and intact FN, we utilized the Alexa Fluor 647 Fluorescent Protein Labeling Kit (Invitrogen, cat. no. A20173) following the instructions provided with the kit.

Following the labeling procedure, SDS-PAGE analysis was conducted, and the protein samples were subsequently subjected to Coomassie blue staining (Bio-Rad, cat. no. 1610436 and 1610438) to evaluate their purity. For the experimental treatments, separate mixtures of labeled:unlabeled FN7-10 and intact FN were prepared in a 1:5 ratio. To ensure accurate dosing for the corresponding experiments, the concentration of labeled proteins was measured using NanoDrop (Thermo Fisher).

2.4.10. Immunofluorescence staining

The cells were washed with 1 × PBS, fixed in 4% paraformaldehyde (PFA, purchased from Thermo Fisher, cat. no. 43368; 16% PFA stock was diluted in 1 × PBS to 4% upon addition) for 15 min at room temperature and rinsed three times in PBS for 5 min each. Next, the cells were blocked and permeabilized in blocking buffer containing 5% normal donkey serum and 0.05% saponin (Thermo Fisher, cat. no. J63209) in 1 × PBS. Then, the cells were incubated overnight at 4 ℃ with primary antibodies in antibody dilution buffer containing 1% BSA and 0.05% saponin. After three rinses in 1 × PBS for 5 min each, the cells were incubated with Alexa Fluor-conjugated secondary antibodies for 1 h in the dark at room temperature. For the immunofluorescence staining of human articular cartilage cryosections, dissected human articular cartilage tissues of the knee (normal or arthritic) were immersion-fixed with 4% PFA in PBS overnight at 4 °C. Following fixation, tissues were then transferred to 30% (w/v) sucrose solution for dehydration overnight at 4 °C. Dissected tissues were next embedded in Tissue-Plus™ O.C.T. Compound (Thermo Fisher, cat. no. 23-730-571) at –80 °C before all other processing. When ready for sectioning, embedded tissues were moved directly into a cryostat microtome (OTF 5000 Cryostat, Hacker-Bright) with O.C.T. medium to mount tissues on the cryostat chuck to allow tissue to equilibrate with the cryostat temperature (–20 °C). Frozen cartilage tissues were sectioned into 20-μm-thick slices and then mounted onto warm Fisherbrand™ Superfrost™ Plus Microscope Slides (Thermo Fisher, cat. no. 12-550-15). Slides were stored at –80 °C until ready for staining. To begin staining, slides were thawed to room temperature and rehydrated twice with PBS for 10 min each. A circle was drawn around the tissue using a hydrophobic barrier pen (Vector Laboratories, cat. no. H-4000). Blocking for 1 h at room temperature was then performed using the above-mentioned blocking buffer. Next, primary antibodies were diluted in the antibody dilution buffer mentioned above and incubated overnight at 4 ℃. Following 1 × PBS wash three times for 10 min each, cryosections were incubated with Alexa Fluor-conjugated secondary antibodies for 2 h in the dark at room temperature. Nuclei were counterstained using diluted DAPI solution (1:1000, Thermo Fisher, cat. no. 62248). The following primary antibodies were used at diluted concentrations: rabbit monoclonal antibody against Rab5(C8B1) (1:200, Cell Signaling Technology, cat. no. 3547), mouse monoclonal antibody against Rab5(E6N8S) (1:200, Cell Signaling Technology, cat. no. 46449), rabbit monoclonal antibody against Rab7 (D95F2, 1:200, Cell Signaling Technology, cat. no. 9367), rabbit monoclonal antibody against Rab11 (D4F5, 1:50, Cell Signaling Technology, cat. no. 5589), rat monoclonal antibody anti-CD29 (clone:9EG7, 1:50, BD Pharmingen, cat. no. 553715), mouse monoclonal antibody anti-CD29(clone: K20, 1:200, Novus Biologicals, cat. no. NBP2-52708), rabbit monoclonal antibody against Src(36D10) (1:400, Cell Signaling Technology, cat. no. 2109), and rabbit polyclonal antibody against p67phox (1:40, Thermo Fisher, cat. no. PA5-52244). Alexa Fluor-conjugated secondary antibodies were obtained from Thermo Fisher, Alexa Fluor 405 donkey anti-rat IgG (H+L) (Thermo Fisher, cat. no. A-48268), Alexa Fluor 488 donkey anti-rabbit IgG (H+L) (Thermo Fisher, cat. no. A-32790), Alexa Fluor 568 donkey anti-mouse IgG (H+L) (Thermo Fisher, cat. no. A-10037), including Alexa Fluor 568 goat anti-mouse IgG (H+L) (Thermo Fisher, cat. no. A-11004) and Alexa Fluor 647 goat anti-rabbit IgG (H+L) (Thermo Fisher, cat. no. A-21245). Alexa Fluor-conjugated secondary antibodies were used at a 1:1000 dilution for cell staining and 1:500 for cryosection staining. Following the completion of immunofluorescence staining, autofluorescence was quenched using a Vector® TrueVIEW® Autofluorescence Quenching Kit (Vector Laboratories, cat. no. SP-8400-15) after draining excess washing buffer from tissue cryosections according to the manufacturer's instructions. Cryosections were mounted using ProLong™ Diamond Antifade Mountant (Thermo Fisher, cat. no. P36961) prior to imaging.

2.4.11. Confocal microscopy and image analysis

Dual-color and three-color confocal images of fluorescently labelled cell samples were obtained using a Zeiss LSM 710 confocal microscope system (Carl Zeiss), which was equipped with 488 nm, 543 nm, 594 nm and 633 nm laser lines, a Plan-Apochromat 40 × NA1.4 Oil DIC M27 objective, standard alkali photomultiplier tubes, and ZEN acquisition software (Zen 2.3 SP1 FP3 black, 64 bit, release version 14.0.0.0). For dual-color images, the EGFP signal was acquired using the 488 nm excitation laser line and detected in the 498-560 nm wavelength range. The mCherry signal was acquired using the 594 nm laser line and detected in the 604-700 nm wavelength range. Images were captured in 636 × 636 pixel format with 2 × line-averaging settings. The pixel size of the *x-y* plane was set as 0.08 μm/pixel. The distance between image planes in the *z*-direction was set as 0.20 μm/step during three-dimensional (3D) *z*-stack recording. For three-color images, the EGFP signal was acquired using the 488 nm excitation laser line and detected in the 504-543 nm wavelength range, the mCherry signal was acquired using the 543 nm excitation laser line and detected in the 572-621 nm wavelength range, and the Alexa Fluor 647 signal was excited using the 633 nm laser line and detected in the 643-700 nm wavelength range. Images were captured in 1024 × 1024 pixel format with 2 × line-averaging settings. The pixel size of the *x-y* plane was set as 0.05 μm/pixel. The distance between image planes in the *z*-direction was set as 0.46 μm/step during the 3D *z*-stack recording. Four-color confocal images of fluorescently labelled cell samples were obtained using a Zeiss LSM 900 confocal microscope system (Carl Zeiss), which was equipped with 405 nm, 488 nm, 561 nm and 640 nm laser lines, a Plan-Apochromat 40 × NA1.4 Oil DIC M27 objective, GaAsP photomultiplier tubes, and ZEN acquisition software (Zen 2.3 SP1 FP3 black, 64 bit, release version 14.0.0.0). The Alexa Fluor 405 signal was acquired using the 405 nm excitation laser line and detected in the 410-470 nm wavelength range, the Alexa Fluor 488 signal was acquired using the 488 nm excitation laser line and detected in the 500-550 nm wavelength range, the Alexa Fluor 568 signal was excited using the 561 nm excitation laser line and detected in the 575-645 nm wavelength range, and the Alexa Fluor 647 signal was excited using the 640 nm laser line and detected in the 645-700 nm wavelength range. Images were captured in 453 × 453 pixel format, without averaging. The pixel size of the *x*-*y* plane was set as 0.071 μm/pixel. The distance between image planes in the *z*-direction was set as 0.20 μm/step during three-dimensional (3D) *z*-stack recording. Confocal images of human cartilage tissues were captured using a Zeiss LSM 700 confocal microscope system (Carl Zeiss) equipped with 405 nm, 555 nm, and 639 nm laser lines, a Plan-Apochromat 20 ×/0.8 M27 objective, standard alkali photomultiplier tubes, and ZEN acquisition software (Zen 2011 SP7 FP3 black, 64 bit, release version 14.0.0.0). The Alexa Fluor 405 signal was acquired using the 405 nm excitation laser line and detected in the 300-483 nm wavelength range, the Alexa Fluor 568 signal was acquired using the 555 nm excitation laser line and detected in the 493-600 nm wavelength range, the Alexa Fluor 647 signal was acquired using the 640 nm excitation laser line and detected in the 644-800 nm wavelength range. Images were captured in 2048 × 2048 pixel format with 2 × line-averaging settings. The pixel size of the *x*-*y* plane was set as 0.16 μm/pixel. The distance between image planes in the *z*-direction was set as 1.00 μm/step during the 3D *z*-stack recording. The 1 AU pinhole size was set on the longest wavelength fluorophore with the same size for the rest of the images in the same dataset. Images in the same dataset were acquired with the same settings and all channels had intensities below saturation. Fields of view were selected randomly. *Z*-stack images were deconvolved using AutoQuant X3 (Media Cybernetics) using default settings. Image analysis was performed in ImageJ/Fiji (the National Institutes of Health, for format transformation, region of interest selection, montage, and kymograph presentation), Matlab (MathWorks, for ratiometric demonstration) and Excel (Microsoft, for line profiling). 3D rendering was performed in Imaris (Bitplane).

To determine the distribution of α5 integrin associated with the early or late endosome compared to the cell membrane in **Figure 2.1** and **Figure 2.3**, we created two types of 3D objects: those that enclosed all the endosomes and others that enclosed only the surface membrane of cells. Because our endosomal markers were on the surfaces of endosomes but not inside them, we took a multi-step approach to create 3D objects that enclosed all of the endosome, including their interior volume and not just their labelled membranes. A corresponding workflow diagram is presented in **Figure 2.21**. First, we used automatic thresholding in Imaris's "surface" tool to create a 3D object based on either the mCherry channel to recognize constitutively active early endosomes (mCherry–Rab5CA(Q79L) in **Figure 2.1**), or the EGFP channel to recognize constitutively active late endosomes (EGFP–Rab7CA(Q67L) in **Figure 2.3**). Second, using the masking function in Imaris, these 3D objects were used to create a binary data channel with the masked signal set as "255" (white) and the non-masked signal set as "0" (black). Third, multi-channel images were then imported into ImageJ/Fiji, where a custom macro was used to "fill" hollow centers of constitutively active endosomes in the binary channel. The result was a channel where the inside and membrane of an endosome had a constant value of 255. Fourth, the resulting data was converted back into the Imaris file format using Imaris File Converter and imported into Imaris. Fifth, within Imaris, we used the "surface" tool to create a 3D object on the now "filled" (without a hollow interior) endosome binary channel created by the ImageJ/Fiji macro. The result was 3D objects that enclosed each endosome (membrane and interior), which could be used for further analysis. To generate a 3D object enclosing the cell membrane, we used the "surfaces" tool in Imaris based on either the EGFP (**Figure 2.1**) or mCherry (**Figure 2.3**) channel, depending on the form of fluorescent α5-integrin fusion being used. A manual threshold was performed to only include the cell membrane in a manner blind to the experimental treatment. The percentage of α5-integrin fluorescence intensity associated with the early endosome (**Figure 2.1**) or late endosome (**Figure 2.3**) compared to the cell membrane was determined using the following equation:

$$\frac{F_c endosome}{F_c cell\ membrane} = \frac{\sum F_{endosome} - F_{back} \times \#Voxel_{endosome}}{\sum F_{cell\ membrane} - F_{back} \times \#Voxel_{cell\ membrane}} \tag{1}$$

where $\mathrm{F_c endosome}$ is the corrected α5-integrin fluorescence intensity associated with the early endosome (**Figure 2.1**) or late endosome (**Figure 2.3**), $\mathrm{F_c cell\ membrane}$ is the corrected α5 integrin fluorescence intensity associated with the cell membrane, $\mathrm{F_{back}}$ is the background fluorescence intensity that was measured in ImageJ/Fiji at cell-free positions of middle layers, $\sum F_{endosome}$ is the sum of α5-integrin fluorescence intensity associated with the early endosome (**Figure 2.1**) or late endosome (**Figure 2.3**), $\sum F_{cell\ membrane}$ is the α5 integrin fluorescence intensity associated with the cell membrane, $\#Voxel_{endosome}$ is the number of voxels on the endosome, and $\#Voxel_{cell\ membrane}$is the number of voxels associated with the cell membrane. $\sum F_{endosome}$, $\sum F_{cell\ membrane}$, $\#Voxel_{endosome}$, and $\#Voxel_{cell\ membrane}$ were automatically determined by Imaris.

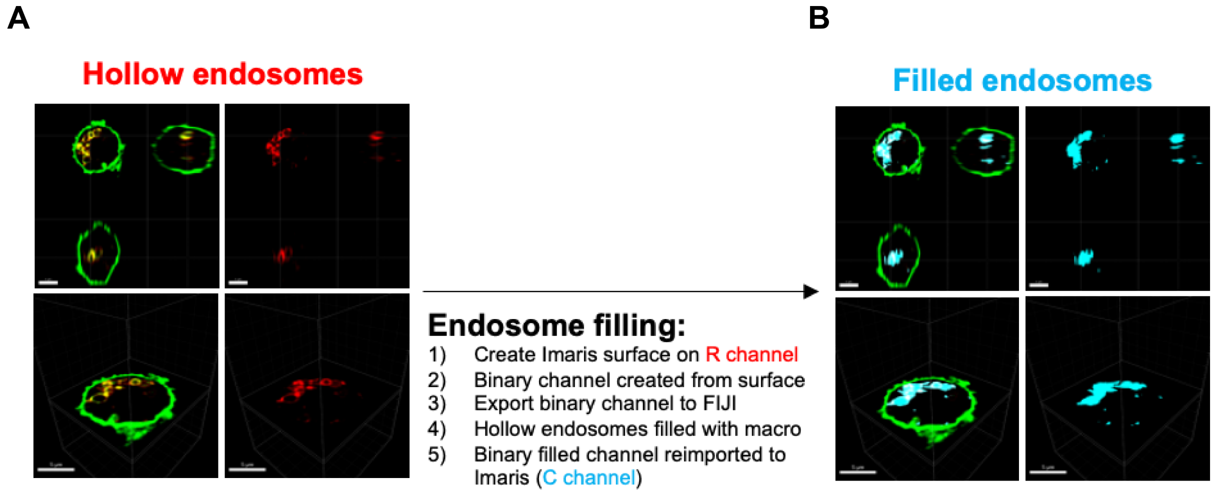

Endosome filling:

1) Create Imaris surface on R channel
2) Binary channel created from surface
3) Export binary channel to FIJI
4) Hollow endosomes filled with macro
5) Binary filled channel reimported to Imaris (C channel)

Figure 2.21 Workflow diagram demonstrating conversion of hollow endosomes to filled endosomes.

First, Imaris's "surface" tool was used to create a 3D object based on the R channel. Second, using the masking function, the 3D objects were used to create a binary data channel with the masked signal set as "255" (white) and the non-masked signal set as "0" (black). Third, the multi-channel images were exported to Fiji. Fourth, the hollow centers of constitutively active endosomes were filled with a custom macro. Fifth, the resulting data was transferred back to Imaris to create a 3D object on the now "filled" endosomes. (**A**) Hollow endosomes. (**B**) Filled endosomes after the endosome filling method. A more detailed protocol is provided in the methods section. This protocol was also applied to generate a 3D object that enclosed an entire cell to determine the percent volume of FN7-10–EGFP relative to the entire cell. Scale bars, 5 μm.

Custom Macro

Fiji macro “Blob filler” used for confocal imaging analysis of constitutively active endosomes written in IJ1 macro language.

```
//Blob filler

//Select dataset. Image file below is an example.
selectWindow("10_2h_Image 1 ws.czi.ims - 10_2h_Image 1 ws.czi.ims Resolution Level 1");

//Duplicate channel with endosome thresholded to 255 (macro assumes channel 3, but this can
be changed)
run("Duplicate...", "duplicate channels=3");

//Convert to 8 bit for compatibility with thresholding and speed
run("Conversions...", " "); //this will remove conversion scaling
run("8-bit");


//Note: Dilate will capture material both inside AND around Rabs. It will close "C" type structures.
run("Dilate (3D)", "iso=255"); //Iso settings at 255 to do Dilate on thresholded image.

//Generate ROIs that fill in holes
roiManager("reset"); //delete any ROIs from previous analysis
run("Analyze Particles...", "display exclude clear include summarize add stack");

//Get number of rois, select each one and fill in with white. Note that ones with holes will be filled,
other won't change
setForegroundColor(255, 255, 255);
for (i = 0; i < roiManager("count"); i++) {
	roiManager("Select", i);
	run("Fill", "slice");
}

//Erode back what was dilated, AFTER filling holes.
run("Erode (3D)", "iso=255");

//Convert to 32-bit, for compatibility with Imaris
run("32-bit");

//delete ROIs
roiManager("reset");
```

To determine the internalization of the fluorescently tagged FN7-10 (FN7-10–EGFP) in **Figure 2.7** and **Figure 2.8**, the following was measured at each experimental condition: (i) the volume of FN7-10–EGFP associated with the cell compared to the volume of the whole cell (**Figure 2.7**) to quantify FN7-10–EGFP internalization, (ii) the percentage of FN7-10–EGFP colocalized with α5 integrin–mCherry (**Figure 2.7**) to determine if the internalization of FN7-10–EGFP is mediated by α5 integrin, and (iii) the percentage of FN7-10–EGFP entering early endosomal compartments (**Figure 2.8**) to determine if endocytosed FN7-10–EGFP enters early endosomes at the indicated time points.

(i) To measure the volume of FN7-10–EGFP associated with the cell compared to the volume of whole cell in **Figure 2.7**, we first used automatic thresholding in the Imaris "surface" tool to create a 3D object based on the mCherry channel to recognize α5-integrin–mCherry (in some cases, manual adjustment was applied to ensure that the cell boundary was included in a blind manner). Then, using the masking function in Imaris, we generated a binary data channel on the 3D object created with the masked signal set as "255" (white) and the non-masked signal set as "0" (black). The custom ImageJ/Fiji macro described above was used to "fill" the hollow cell center in the binary data channel. The result was a channel where the inside and membrane of the cell had a constant value of 255. The resulting data was converted back into the Imaris file format using Imaris File Converter and imported into Imaris. Within Imaris, we used the "surface" tool to create a 3D object on the now "filled" (without hollow interior) cell binary channel created by the ImageJ/Fiji macro. The result was a 3D object that enclosed each cell (membrane and interior), which could be used to measure the whole cell volume and to mask the EGFP channel to determine the volume of FN7-10–EGFP associated with the cell. The percentage of volume of FN7-10–EGFP associated with the cell compared to the volume of whole cell was determined using the following equation:

$$V\% = \frac{V_{FN7-10-EGFP}}{V_{whole\ cell}} \times 100\% \quad (2)$$

where $V_{FN7-10-EGFP}$ is the volume of FN7-10–EGFP associated with the cell and $V_{whole\ cell}$ is the volume of 3D object created on the "filled" cell binary data channel. $V_{FN7-10-EGFP}$ and $V_{whole\ cell}$ were automatically determined by Imaris.

(ii) To measure the percentage of FN7-10–EGFP colocalized with α5 integrin–mCherry in **Figure 2.7**, a "colocalization result" channel was generated to represent the FN7-10–EGFP and α5 integrin–mCherry colocalized area, with automatic thresholding applied on the EGFP channel and the mCherry channel. The colocalization percentage was calculated by Imaris. Similarly, a "colocalization result" channel was generated to represent the percentage of α5 integrin–EGFP at early endosomes indicated by mCherry–Rab5, late endosomes indicated by mCherry–Rab5, and recycling endosomes indicated by mCherry–Rab11 in **Figure 2.5**, and the percentage of α5 integrin–EGFP or FN7-10–EGFP at early endosomes, as shown by mCherry–Rab5 in **Figure 2.11**.

(iii) To determine the percentage of FN7-10–EGFP entering early endosomal compartments in **Figure 2.8**, we first took a multi-step approach to create 3D objects that enclosed endosomes (membrane and interior) as described above. Then, a "colocalization result" channel was generated to represent the percentage of FN7-10–EGFP associated with "filled" endosomes with automatic thresholding applied on the EGFP channel and the "filled" endosome binary channel created by the ImageJ/Fiji macro channel. The colocalization percentage was calculated by Imaris.

To determine the percentage of EGFP–Nox2 (**Figure 2.14**) or Nox4–EGFP (**Figure 2.15**) colocalized with Alexa Fluor 647 immunolabelled Rab5 (Rab5^{+}) and α5 integrin–mCherry (α5 integrin^{+}) vesicles under each experimental condition, we used the colocalization module in Imaris. A "Rab5^{+}α5 integrin^{+} vesicle" surface was generated based on a "colocalization result/double-positive vesicle" channel with automatic thresholding applied to the mCherry channel and the Alexa Fluor 647 channel. The colocalization percentage between EGFP–Nox2 or Nox4–EGFP with Rab5$^+$α5 integrin$^+$ vesicles was determined by Imaris with automatic thresholding applied on the EGFP channel and "Rab5$^+$α5 integrin$^+$ vesicle".

To determine the percentage of endogenous Src colocalized with α5 integrin–EGFP associated with mCherry–Rab5CA(Q79L) in **Figure 2.18** under each experimental condition, we used the colocalization module in Imaris. A "colocalization result/α5 integrin–EGFP inside mCherry–Rab5CA(Q79L)" was generated with automatic thresholding applied to the EGFP channel and the "filled" endosome binary channel as described above. Then, the percentage of endogenous Src colocalized with α5 integrin–EGFP inside Rab5CA(Q79L) was determined by Imaris with automatic thresholding applied to the Alexa Fluor 647 channel and the "α5 integrin–EGFP associated with inside mCherry–Rab5CA(Q79L)" channel.

For the analysis of *z*-stacks of deconvolved images acquired using human cartilage tissues, the percentage of Src colocalized with Rab5 (**Figure 2.20**) and p67phox colocalized with Rab5 (**Figure 2.20**) was determined by Imaris with automatic thresholding applied or, in some cases, by manual adjustment to ensure that the generated surfaces did not exceed the cell boundary on the Alexa Fluor 568 and Alexa Fluor 647 channels. Image analysis was performed in a blind manner. Intensity profiling for multi-channel images was performed using ImageJ/Fiji.

2.4.12. Live cell imaging

Transfected human chondrocytes were seeded into glass-bottom dishes (Cellvis, Cat. No. D35-20-1.5H) in serum-containing media after nucleofection. 48 h later, the cells were serum starved in phenol red-free DMEM/F-12 (Thermo, Cat. No. 21041025) overnight before experiments. Images were acquired with reflection-based laser autofocus (Definite Focus) on a Zeiss LSM 710 confocal microscope system with a Plan-Apochromat 40 × NA1.4 Oil DIC M27 objective. Throughout the experiments, cells were maintained in a stage-top incubator (Pecon, Incubator PM 2000 RBT) that provided a humidified atmosphere of 5% CO_2 (Pecon, CO_2

Module S) at 37 °C (Pecon, TempModule S). For ratiometric HyPer3 imaging in **Figure 2.16** and **Figure 2.17**, scanning was performed at 2 min intervals, with FN7-10 (**Figure 2.16**) or intact fibronectin (FN) (**Figure 2.17**) being added after the fifth scan (10 min after the start of the experiment) and was recorded over the course of 120 min following treatment, for a total of 65 frames. Hyper3 fluorescence was sequentially excited at both 405 nm wavelength and 488 nm wavelength using the same emission filter (498-580 nm wavelength range) in 512 × 512 pixel format with 2 × line averaging. The pixel size of the *x-y* plane was set as 0.42 μm/pixel. Images in the same dataset were acquired with the same settings and at fixed intensity settings below saturation and recorded with 12-bit depth. HyPer3 was background-subtracted (by using ROIs at cell-free positions), and the ratio (F488/F405) was measured as the average emission intensity excited at 488 nm wavelength (F488) divided by the average emission intensity excited at 405 nm wavelength (F405) of the whole cell. The average intensities of F488 and F405 from the first five frames pretreatment were normalized as 1 in **Figure 2.16** and **Figure 2.17**. Then, the kymographs are demonstrated as fluorescence intensity along the line (*y*-axis) against time (*x*-axis). For other dual-color imaging to indicate early endosomal trafficking, indicated by mCherry–Rab5CA(Q79L), of EGFP fusion proteins, the EGFP signal was excited using the 488 nm laser (498-560 nm emission), and the mCherry fluorescence was excited using the 594 nm laser (604-700 nm emission), in 636 × 636 pixel format with 2 × line averaging. The pixel size of the *x-y* plane was set as 0.08 μm/pixel. Confocal scanning was performed at 5 min intervals, with PBS vehicle, FN7-10 or intact FN being added after the second scan (10 min after the start of the experiment) and was recorded over the course of 180 min following the treatment, resulting in a total of 38 frames. The ratiometric analysis in **Figure 2.2** and **Figure 2.9** was performed using ImageJ/Fiji by measuring the mean intensity of regions of interest (ROIs) of endosomes (indicated by mCherry–Rab5CA(Q79L)) and cell membranes across the 180 min imaging period. The ratiometric images were generated by Matlab scripts that calculate the ratio of intensities from pixels at same position. Pseudo colors and look up tables were then applied in ImageJ/Fiji. The average intensities of EFGP fusion proteins of ROIs of endosomes from the first two frames pretreatment were normalized as 1. Kymographs of time-lapse images were generated by drawing lines (shown as dashed lines) across the images and produced in ImageJ/Fiji using the “reslice” function. The kymographs show the fluorescence intensity along the line (*y*-axis) against time (*x*-axis).

2.4.13. Immunohistochemical staining of human cartilage and analysis

Osteoarthritic human cartilage was isolated from the femoral condyle obtained from adult donors who had knee replacement surgery at the University of North Carolina Hospitals Hillsborough Campus (Hillsborough, NC, USA). Full-thickness tissue samples were obtained from damaged and adjacent less damaged osteoarthritic areas, determined macroscopically and microscopically, from the same patient. Representative safranin orange and fast green (SOFG) staining is shown in **Figure 2.19**, indicating the difference in cartilage matrix loss between less damaged and damaged areas. Healthy human femoral condyles were provided by the Gift of Hope Organ and Tissue Donor Network (Itasca, IL, USA) through an agreement with Rush University Medical Center (Chicago, IL, USA), where cartilage tissue of the femoral condyle had been carefully inspected, and only those with normal appearance (grade = 0 or 1) were used in experiments as healthy controls. Processed full-thickness osteoarthritic or healthy cartilage tissue samples were cut into 6 μm sections, deparaffinized and rehydrated with xylene and ethanol gradients. Heat-induced antigen (epitope) retrieval (HIRE) was performed in sodium citrate buffer (pH = 6, Sigma-Aldrich, cat. no. W302600) at 90 °C for 30 min. Endogenous peroxidase activity was blocked with 3% H_2O_2 for 10 min, followed by a 1 h incubation with 5% donkey serum (Jackson ImmunoResearch, cat. no. 017-000-121) in 0.1% Triton/PBS to block non-specific IgG binding and a subsequent overnight incubation with primary antibodies in a humidified chamber at 4 °C. The following antibodies for immunochemistry staining were used at diluted concentrations: antibodies against Rab5(C8B1) (1:200, cat. no. 3547) and Src(36D10)

(1:200, cat. no. 2109) were purchased from Cell Signaling Technology; the antibody against p67phox (1:40, cat. no. PA5-52244) was purchased from Thermo Fisher, and the antibody against Nox4 (1:200, cat. ab109225) was purchased from Abcam. Secondary antibody incubation was thereafter performed using Biotin-SP (long spacer) AffiniPure Donkey Anti-Rabbit IgG (H+L) (1:200, Jackson ImmunoResearch, cat. no. 711-065-152) for 1 h, and then slides were incubated with VECTASTAIN™ Elite™ Avidin-Biotin Complex (ABC) solution (Vector laboratories, cat. no. PK-6100) for another hour before 1 × PBS washing followed by incubation with Vector™ DAB peroxidase substrate (Vector laboratories, cat. no. SK-4100). After counterstaining with hematoxylin (Cole-Parmer, cat. no. 3530-32) for 3 min, the slides were dehydrated, cleared in xylene and mounted with Fisher Chemical™ Permount™ Mounting Medium (Thermo Fisher, cat. no. SP15-100). Cell counts were performed using ImageJ/Fiji software. Image analysis was performed in a blind manner. There were nine randomly selected distinct fields at 10 × magnification per donor assessed for different conditions, across normal and less damaged or damaged osteoarthritic cartilage, from at least three sections (30 μm apart). The mean immune-positive cell percentage was reported based on nine assessments for each donor per applicable condition. Images were taken using an Olympus BX60 microscope (Olympus).

2.4.14. Publicly available data collection and processing

The bulk RNA-seq data were downloaded from GSE14007 and GSE168505 and analyzed using R v4.2.1 and GSEA v4.2.3 (*162*). The gene expression data was normalized by dividing the total number of reads for each sample. Then, GSEA analyses were conducted with standard weighted enrichment statistics and Signal2Noise was adopted as the metric for ranking genes. Finally, two-sided Student’s t-tests were performed for identifying differentially expressed genes. The scRNA-seq data was downloaded from GSE104782 and analyzed using Seurat (v 4.2.0) workflow (*163*). Genes expressed in less than three cells and cells expressing less than 300 genes were filtered to improve the accuracy of the analysis. Then, the top 2000 highly variable genes were identified. Principal component analysis (PCA) and uniform manifold approximation and projection (UMAP) were performed to reduce the high data dimensionality into two-dimensional space. R package harmony (*164*) was used to perform batch correction, and R package Nebulosa (*165*) was applied to recover signals of gene expression using weighted kernel density estimation. Cell type labels and stage information were assigned to cells based on the annotations provided by Ji et al. (*142*). Differentially expressed genes (DEGs) among different stages were identified and analyzed by Seurat v3 using the FindMarkers function (default a Wilcoxon Rank Sum test), with the log-scaled fold change threshold of 0.25 and P value threshold of 0.05. The bulk RNA-seq and single-cell RNA-seq data are available in the NCBI's Gene Expression Omnibus (GEO) data repository.

2.4.15. Statistics and reproducibility

Statistical analyses were performed using GraphPad Prism (8.0). Two-sided Student's t-test (paired or unpaired, as appropriate) was used when two datasets were compared. One-way or Two-way ANOVA (considering both time and treatment and their interaction as factors), followed with post hoc Tukey's test, was used for multiple comparisons (*166*). Boxplots show all data values in which the 25th and 75th percentiles are indicated, and whiskers show the minima and maxima. Densitometry data generated from immunoblotting, ratiometric data generated from live-cell imaging, and data generated from immunohistochemistry analyses are presented as the mean ± s.e.m. Analysis using bulk RNA-seq data from GSE14007 and GSE168505 and scRNA-seq data from GSE104782 were detailed above. A P value of less than 0.05 was considered significant. *$P < 0.05$, ** $P < 0.01$, *** $P < 0.001$, **** $P < 0.0001$; n.s, no significance. No statistical method was used to predetermine sample sizes. No data were excluded. Sample sizes and statistical analyses for each experiment are denoted in the figure legends. To ensure reproducibility, key experiments were repeated at least three times where possible. For certain confocal imaging studies where extensive data processing was required at the single cell level, results from n=30 or more cells from 2 independent donors were analyzed. All attempts were successful. To ensure randomization in the immunofluorescence and immunohistochemistry analyses, pictures were taken of different fields (tissue samples or individual cells) from independent donors at different locations. Analyses were performed in a blind manner. Immunoblots were performed at least three times with similar results, and a representative blot from independent donors is shown. Unprocessed blots and numerical source data with precise *P* values for each experiment are provided.

2.4.16. Study approval

Use of human tissues was determined to be exempt from full Institutional Review Board approval by the University of North Carolina at Chapel Hill (Chapel Hill, NC, USA) and the Rush University Medical Center (Chicago, IL, USA) Institutional Review Boards. Informed consent was not required, as human biological samples were provided in a de-identified fashion from surgical waste material or from deceased tissue donors.

3. CHAPTER 3. DISCUSSION AND FUTURE DIRECTIONS

3.1. Summary of Findings

Pathological changes observed in OA joints involve the progressive loss and destruction of articular cartilage, variable levels of synovial inflammation, the formation of osteophytes, subchondral bone thickening, and degeneration of the knee's menisci, ligaments, and joint capsule.(*5*, *112*) Regrettably, there are currently no therapies available to halt or reverse cartilage deterioration. Therefore, it is crucial to acquire a comprehensive understanding of the mechanisms by which chondrocytes function in both healthy and osteoarthritic cartilage.

The work presented in this dissertation demonstrates groundbreaking findings on the involvement of the α5β1 integrin in the utilization of redoxosomes for transmitting and maintaining signals that regulate MAP kinase and Src activation, ultimately leading to chondrocyte MMP production. Redoxosomes play a major role in generating hydrogen peroxide through Nox2, enabling spatial and temporal control. While previous studies have recognized the significance of integrin trafficking through endosomes in regulating various biological processes such as cell signaling, migration, and tissue development,(*103*, *108*) this study stands out as the first to demonstrate the formation of redoxosomes (redox-active endosomes) in response to integrin activation. These findings open up exciting possibilities for therapeutic interventions in OA and other degenerative diseases that conventional treatments cannot address. Selective delivery of antioxidants specific to endosomes or targeted disruption of endosomal signaling could potentially revolutionize treatment approaches for such conditions.

3.2. Future Directions and Outlook

3.2.1. Exploring the Diverse Characteristics of Fibronectin

Fibronectin, a crucial protein, exists in two distinct forms: soluble plasma fibronectin and insoluble cellular fibronectin.(*131*) Cellular fibronectin is found on cell surfaces and within the ECM of different tissues.(*167*) The generation of various isoforms through alternative splicing contributes to the functional variability of fibronectin. Various cell types in joint tissues, including chondrocytes, fibroblasts, fibroblast-like synoviocytes, endothelial cells, and myocytes, produce cellular fibronectin. In specific pathological conditions, certain isoforms of cellular fibronectin are synthesized to a greater extent.(*168*)

Alternative splicing is a significant process involved in wound healing and the development of conditions like OA that greatly impacts fibronectin.(*169*) This process introduces additional domains EIIIA and EIIIB, along with the type III connecting segment (IIICS) found between FnIII14 and FnIII15 exons. While soluble plasma fibronectin consists of a single subunit with the IIICS segment, alternative variants in EIIIA, EIIIB, and IIICS give rise to a considerably higher number of cellular fibronectin isoforms. These isoforms are specifically associated with certain pathological conditions. For instance, elevated levels of the EIIIA isoform in the synovial fluid of rheumatoid arthritis joints are linked to joint degradation. In the case of OA, the expression levels of different isoforms containing the IIICS segment vary, reflecting the extent of cartilage degeneration. The presence or absence of the EIIIA, EIIIB, or IIICS regions leads to structural changes that influence the conformation and signaling of fibronectin during the assembly of the ECM and its interactions with other molecules.(*167*, *170*, *171*) Despite the current understanding, the precise functions of these isoforms remain unclear and necessitate further investigation.

The fibrillary state of fibronectin represents its primary functional form in vivo. This state involves the assembly of fibronectin molecules into interconnected fibers, forming a network. Fibronectin possesses several binding sites, including those for cells, heparin or fibrin, and disulfide bridges involved in dimerization. The assembly process occurs in multiple stages and is dependent on the presence of cells.(*172*, *173*) Initially, fibronectin establishes connections with cells through surface receptors like integrins. Subsequently, fibronectin unfolds, exposing binding sites that facilitate interactions between fibronectin molecules, leading to the formation of the fibronectin-matrix assembly. The expression and assembly of fibronectin are regulated by various molecules specific to each cell type. This assembly process is particularly relevant during tissue remodeling, formation, or repair.(*174*, *175*)

FN-fs of various sizes are present in OA cartilage and synovial fluid. These fragments, including 29 kDa, 45 kDa, 120 kDa, and 200 kDa fragments, stimulate the production of pro-inflammatory cytokines. FN-fs exhibit different functions compared to the intact fibronectin molecule due to the loss of specific domains during proteolysis. Proteolysis alters the structure of the molecule, potentially exposing or creating active sites. Moreover, the reduction in size and conformational changes may enhance tissue penetration. These FN-fs possess unique properties that are absent in native fibronectin. They activate cellular responses by binding to surface receptors such as integrins, Toll-like receptors (TLRs), and CD44, initiating signaling pathways and transcription factors, thus establishing a feed-forward loop.(*129*, *168*, *176*, *177*)

To gain a comprehensive understanding of the specific roles and significance of these diverse biological processes, further research is essential.

3.2.2. Mechanisms of Protease Activity Regulation

MMP-13 is an enzyme that belongs to the metzincins superfamily and plays an important role in breaking down ECM proteins, particularly type II collagen and aggrecan.(*178*) Previous research has indicated that fibronectin matrikines like FN7-10 can stimulate chondrocytes to produce and secrete MMP-13. However, there is still a limited understanding of how MMP-13 functions in the extracellular environment and its regulation, which necessitates further investigation.(*179*)

MMPs are initially synthesized as inactive zymogens, also called pro-MMPs, by different tissues and cells. These pro-MMPs remain inactive due to a "cysteine switch" motif (PRCGXPD), where a cysteine residue coordinates with Zn2+ in the catalytic domain. The activation of pro-MMPs in the extracellular space occurs when other MMPs and proteases proteolytically cleave their pro-domains. In the case of MMP-13, it is first produced as a precursor form weighing 55 to 60 kDa (proMMP-13).(*180*, *181*) Activation of proMMP-13 takes place on the cell surface with the assistance of MT1-MMP, and its efficiency increases when MMP-2 is active.(*182*) The activated form of MMP-13 has a molecular weight ranging from 45 to 48 kDa, with most of the activation occurring outside the cells.(*41*, *183*, *184*)

Regulating the activity of metalloproteinases in the extracellular space involves multiple mechanisms, including binding to the ECM, activation through proteolysis and allosteric mechanisms, interaction with natural inhibitors, binding to molecules on the cell surface, and internalization via endocytosis.(*185*, *186*) Nevertheless, comprehending the precise regulation of metalloproteinase activity within the intricate pericellular environment poses substantial technical obstacles. Nonetheless, acquiring this understanding would greatly enhance our knowledge of the physiological interactions of these enzymes and their dysregulation in various diseases.

Similarly, while it is known that fibronectin matrikines induce chondrocytes to secrete ADAMTSs, which contribute to the degradation of aggrecan and type II collagen in degenerative cartilage, the specific details of this process remain unclear.(*43*) Encouragingly, preclinical studies and Phase I trials investigating inhibitors or nanobodies targeting ADAMTSs have shown promising effects in preclinical models of OA and have demonstrated acceptable safety profiles for further clinical development.(*187*, *188*) Therefore, it is important to gain a fundamental understanding of how chondrocytes generate ADAMTSs in response to disease-associated matrikines. This knowledge holds the potential to enhance sensitivity through tissue-specific cell-based therapeutics and accelerate research efforts towards finding effective cures for OA and related conditions.

3.2.3. Unlocking the Mysteries of Subcellular Redox and Signaling Relay

Redox modulation refers to an imbalance in the redox status of cellular reactions, characterized by the gain (reduction) or loss (oxidation) of electrons by atoms within reacting species. This reactivity plays a fundamental role in utilizing cysteine residues as redox-sensitive molecular sensors, enabling cells to effectively respond to extracellular stimuli.(*189*) One example involves the direct oxidation of cysteine residues near redox-active endosomes by H_2O_2, as demonstrated in this thesis study.

It is important to recognize that redox modulation is a complex process involving changes in the redox potential of organelles and the translocation of proteins between different redox environments.(*190*) This dynamic interplay enables cysteine oxidation to occur throughout the cell, expanding the scope of redox signaling. The propagation of redox signals, whether through direct oxidation or redox relay mechanisms, is influenced by various factors, including the mechanism of generation, duration, and subcellular location of H_2O_2 generation.(*191*)

While progress has been made in understanding redox modulation in chondrocytes, further exploration is needed to investigate redox relay initiation in other ROS-generating organelles, namely mitochondria, endoplasmic reticulum, and peroxisomes, collectively known as the "redox triangle" due to their involvement in ROS-generating biochemical reactions.(*192*, *193*) Additional research is necessary to understand how redox signaling is initiated and propagated in these organelles. Furthermore, membrane contact sites between these organelles play a critical role in ROS production, emphasizing the importance of investigating these contact sites to enhance our understanding of cellular regulation and the propagation of redox signaling.(*193*, *194*)

This thesis study has revealed a compelling interplay between redox and phospho-signaling, specifically mediated by MAP kinases. The oxidation of reactive cysteines governs the upstream regulation of this system, while phosphorylative chain reactions propagate the downstream signal. However, there is still much to be learned about the partners involved in redox modulation and the subsequent phosphorylative chain.(*195*) To delve deeper into these mechanisms, structural biology holds great potential. The improved accessibility and enhanced capabilities of structural biology now allow us to map the localization of cysteines and make precise predictions about the conformational changes induced by oxidatively modified thiols. This will offer invaluable insights into the influence of redox modulation on signaling pathways.(*191*, *196*, *197*)

Furthermore, advancements in redox proteomic detection and biochemical thiol-labeling methods are essential for understanding the redox status of cysteine residues under various conditions, particularly in specific tissues. These techniques will help evaluate and characterize the redox networks regulating cellular processes, intercellular communication, and tissue-specific functions.(*198*, *199*)

In redox biology, the mechanism by which PTPs (with slower reaction rates ranging from 10 to 10^3 M/s) can effectively compete with PRXs (with rate constants up to 2×10^7 M/s) despite their slower reaction rates with H_2O_2 remains an open question. It is highly unlikely that H_2O_2 directly reacts with most cellular protein cysteines, including PTP, in Nox-dependent redox signaling.(*81*, *125*, *191*)

Several explanations for indirect mechanisms have been put forward to address this question, and these explanations are not mutually exclusive. Firstly, H_2O_2 action may involve redox relays, where PRXs and/or peroxidases act as initial H_2O_2 sensors and subsequently oxidize the ultimate targets. This implies that the sensing of H_2O_2 occurs through intermediary proteins before reaching the intended targets.(*81*, *200*)

Secondly, during redox signaling, PRXs may undergo transient inactivation, allowing H_2O_2 to accumulate. This "floodgate hypothesis" suggests that the oxidation of less reactive H_2O_2 targets is facilitated by the conversion of PRXs into redox-inactive sulfinic and sulfonic forms, which enables the buildup of H_2O_2 levels for downstream signaling.(*201*, *202*)

Thirdly, localized intracellular H_2O_2 concentration gradients may exist, allowing for the selective oxidation of protein targets within specific microenvironments. This process relies on the formation of scaffolded macromolecular signaling complexes, which is further supported by the redoxosomes formation as found in this thesis study.(*125*)

Our observations revealed the formation of redoxosomes in chondrocytes in response to FN7-10 stimulation, and their formation correlated with the generation of H_2O_2, as measured using the HyPer-based ratiometric biosensor. These redoxosomes serve as specialized compartments where H_2O_2 can accumulate, creating localized concentrations that facilitate the oxidation of specific protein targets.

However, the exact role of redoxosomes in signaling protein oxidation remains uncertain, although it is highly probable. In our study, we observed the formation of redoxosomes in conjunction with the translocation of non-receptor tyrosine kinases, such as Src. Nevertheless, we did not specifically investigate whether Src undergoes oxidation within the subcellular environment, although based on our observations, it is likely to occur. Further research is necessary to unravel the specific mechanisms and targets of protein oxidation within redoxosomes and their impact on cellular signaling. The involvement of redox relay is highly plausible, as certain data in our thesis study indicated that overexpressing cytosolic PRX2 partially blocked FN7-10-induced MAP kinase signaling. This suggests the potential importance of redox relay in mediating the signaling effects of redoxosomes.

Therefore, we propose specific experiments to further investigate the characteristics of redoxosomes in response to FN7-10 activating α5β1 integrin. One such technique is the iodixanol density gradient isolation method. This method allows for the isolation and separation of redoxosomes resulting from the activation of α5β1 integrin by FN7-10, as determined in this thesis project. By leveraging the variations in size and density among organelles, we can effectively distinguish redoxosomes from other major subcellular components such as the lower-density plasma membrane, peroxisomes, and mitochondria.(*146*, *203*) Moreover, as the recruitment of Rac1 to receptor-activated redoxosomes has been observed. Another proposed experiment involves infecting cells with a recombinant adenovirus that expresses Rac1 fused with an HA-tag, prior to FN7-10 stimulation, enabling us to investigate the proteins associated with the recruitment of Rac1 to redoxosomes. To further analyze these proteins, mass spectrometry can be employed.(*146*, *203–205*)

We also propose investigating in vivo redoxosome activity, taking into account that cultured cells tend to generate higher levels of ROS compared to their in vivo counterparts.(*189*) In order to achieve this, we suggest employing adenovirus-mediated gene transfer to express two types of probes, namely Rab5 fused with roGFP2-Orp1 and HyPer, in an injury-induced OA mouse model.(*189*, *206*, *207*) These probes enable the measurement of redox activity in tissue sections. However, it is important to note that earlier versions of HyPer are susceptible to pH-related signal fluctuations. Consequently, incorporating the expression of a control probe becomes necessary to determine and assess such variations.(*189*) Additionally, cryosections of tissue samples should be promptly treated with N-ethylmaleimide, a fast-acting thiol blocker, to ensure result accuracy and eliminate potential interference from thiol oxidation, as elaborated in previous publications.(*206*, *207*) This approach can also be applied to study redoxosome activity under various physiological and pathological conditions.

By synergistically integrating these approaches, we can effectively identify the binding partners or signaling molecules linked to redoxosomes following pro-inflammatory stimuli, such as FN7-10 used in this thesis study. This comprehensive analysis will unveil the intricate interdependencies between redox and phospho-signaling and provide insights into the contribution of redoxosome activity to the development of OA. These significant discoveries will shed light on concealed mechanisms, paving the way for compelling therapeutic interventions and precise treatments targeting conditions like OA and other diseases marked by dysregulated redox and phosphorylation pathways.

In addition, the term "ROS" (including within this thesis!) should be more often replaced with more specific mentions of the chemical species responsible for the observed effect. This improvement will result in enhanced specificity when describing biological processes, especially in the context of future studies, as emphasized in the introductory chapter of the thesis.

3.2.4. Refocus on the Pathogenesis of Osteoarthritis: Exploring the Missing Pieces

Cartilage is primarily composed of a dense ECM along with specialized cells called chondrocytes. Recent research has revealed that articular cartilage comprises different subtypes of chondrocytes, each with unique characteristics.(*142*) These subtypes include proliferative chondrocytes, primarily found in the proliferative zone of growth plates, and hypertrophic chondrocytes, which play a decisive role in regulating cartilage matrix mineralization. Additionally, studies have identified two additional cell types in cartilage: senescent cells and cartilage progenitor cells.(*208–213*)

This groundbreaking redefinition challenges the long-held notion that chondrocytes are the sole cell type in cartilage. It illuminates the intricate complexity and remarkable heterogeneity within this tissue, encompassing diverse aspects such as morphology, localization, physical properties, and molecular functions.

In light of this emerging understanding, it is essential to explore the key features and roles of these chondrocyte subtypes and their interactions within the cartilage microenvironment. A critical knowledge gap related to this thesis study is whether the cellular heterogeneity present in cartilage contributes to the progression of OA. Considering the disruptive nature of the disease development when cellular interactions are compromised or molecular signals are misinterpreted, examining the impact of cellular heterogeneity on disease progression becomes even more important.

Thanks to remarkable advancements in the fields of bioinformatics and computational biology, there have been significant breakthroughs in analyzing intercellular signaling using gene expression data from both bulk and single-cell datasets. One approach involves studying the coordinated expression patterns of ligand-receptor pairs to infer intercellular communication. Furthermore, the incorporation of spatial measurements of specific genes allows the use of structured optimal transport to recover the spatial characteristics of scRNA-seq data. This innovative method establishes a spatial metric for individual cells based on a spatial map, enabling the estimation of cell-cell communication. As a result, spatial relationships between genes across cells can be inferred, facilitating the reconstruction of spatial dynamics within tissues.(*214–217*)

To fully comprehend the progression of OA, we must broaden our focus beyond articular cartilage alone. OA affects not only the cartilage but also induces pathological changes in adjacent structures such as bone, the synovial membrane, ligaments, and menisci.(*112*) Exploring the mechanisms of interaction and reciprocal communication among these tissues is essential for unraveling the complexities of disease progression. However, it remains unclear whether specific matrikines formed in other joint tissues can penetrate pathological changes. Do these matrikines primarily interact with cells within their tissue of origin, or do they exert their influence by engaging multiple cell types simultaneously? This intriguing question warrants further investigation and can shed light on the mechanisms underlying the progression of OA.

While much progress has been made in understanding cellular catabolic responses and morphological changes in cartilage, one critical aspect has been overlooked—the excruciating pain experienced by OA patients. To develop effective pain management strategies, we must unravel the intricate correlation between these mechanisms and pain perception. This paramount endeavor will provide us with a comprehensive understanding of how these mechanisms influence pain perception in OA patients, ultimately paving the way for advanced and more effective pain relief options that significantly enhance their quality of life.

3.2.5. Enhancing the Potential of Integrin Targeting: Advancing Therapeutic Strategies for Osteoarthritis

The remarkable potential of integrin targeting has captivated visionary researchers, sparking an extraordinary quest to unlock their full capabilities. These versatile proteins can be modulated through various mechanisms, such as activation as agonists or inactivation as silent antagonists or inhibitors.(*218*) These groundbreaking strategies hold immense promise for revolutionizing therapeutic approaches for OA, paving the way for significant advancements in treatment options. From the development of silent antagonists to functional inhibitors, initiatives focused on integrin targeting are poised to reshape the landscape of OA therapies.

A wide array of approaches are being employed in numerous drug discovery initiatives targeting integrins. These include the utilization of small molecules, synthetic mimic peptides, antibodies, peptide drug conjugates, antibody-drug conjugates, nanotherapeutic agents, chimeric antigen receptor (CAR) T-cell therapy, and imaging agents.(*218–221*) Despite the considerable attention that integrins have received in drug discovery projects and clinical studies, the number of approved therapies remains disappointingly low.(*218*, *219*) The translation of preclinical integrin data into clinically effective drugs poses a complex challenge, influenced by both general obstacles in drug development and those specific to the target class.

Historically, many tested integrin inhibitors have faced challenges related to suboptimal pharmacokinetics, resulting in inadequate target coverage and poor exposure due to unfavorable routes of administration and dosing regimens. Overcoming this hurdle is pivotal for the development of small-molecule drugs.(*222*) However, a glimmer of hope emerges from the exciting Phase I trial results of LNA043, which targets integrin α5β1 derived from the FBN-like domain of ANGPTL3, has an ability to induce chondrogenesis and regenerate hyaline articular cartilage when injected into the knee.(*67*)

While the therapeutic opportunities presented by integrin targeting continue to be unraveled, addressing the complex needs of OA patients remains an ongoing challenge. The clinical phenotype of osteoarthritis encompasses various molecular endotypes at different stages of pathogenesis, including cartilage-driven, bone-driven, and synovitis-driven pathways.(*188*) This complexity further complicates the task of identifying distinct subgroups within the OA population.

3.3. Concluding Remarks

In conclusion, this thesis research provides valuable insights into the intricate mechanisms underlying the pathogenesis of OA and highlights the potential for innovative therapeutic strategies. While advancements in disease-modifying drugs for OA show promise for therapeutic interventions, there are challenges in translating preclinical data into clinically effective drugs.

A significant breakthrough in this research is the identification of redoxosomes as a novel signaling entity and their role in transmitting and maintaining redox signals related to protease production, particularly MMPs. This discovery opens up exciting possibilities for targeted interventions that can modulate redox balance and signaling pathways, thereby offering potential avenues for more effective treatment approaches in OA.

Given the complexity of OA pathogenesis, it is essential to continue comprehensive research to unravel the underlying mechanisms. By deepening our understanding of these mechanisms, we can pave the way for the development of even more precise and targeted therapeutic strategies that have the potential to significantly improve the lives of OA patients. These advancements have the potential to alleviate pain, enhance joint function, and ultimately enhance the overall quality of life for individuals living with OA.

REFERENCES

1. Y. Zhang, J. M. Jordan, Epidemiology of osteoarthritis. *Clin. Geriatr. Med.* **26**, 355–369 (2010).

2. T. M. Gill, Do the tenets of late-life disability apply to middle age? *Ann. Intern. Med.* **167**, 818–819 (2017).

3. L. Sharma, Osteoarthritis of the knee. *N. Engl. J. Med.* **384**, 51–59 (2021).

4. D. J. Hunter, L. March, M. Chew, Osteoarthritis in 2020 and beyond: a Lancet commission. *Lancet*. **396**, 1711–1712 (2020).

5. D. Chen, J. Shen, W. Zhao, T. Wang, L. Han, J. L. Hamilton, H.-J. Im, Osteoarthritis: toward a comprehensive understanding of pathological mechanism. *Bone Res.* **5**, 16044 (2017).

6. D. J. Hunter, J. J. McDougall, F. J. Keefe, The symptoms of osteoarthritis and the genesis of pain. *Rheum. Dis. Clin. North Am.* **34**, 623–643 (2008).

7. G. Peat, Knee pain and osteoarthritis in older adults: a review of community burden and current use of primary health care. *Ann. Rheum. Dis.* **60**, 91–97 (2001).

8. J. Cibere, Do we need radiographs to diagnose osteoarthritis? *Best Pract. Res. Clin. Rheumatol.* **20**, 27–38 (2006).

9. J. R. Hochman, L. Gagliese, A. M. Davis, G. A. Hawker, Neuropathic pain symptoms in a community knee OA cohort. *Osteoarthr. Cartil.* **19**, 647–654 (2011).

10. W. H. Robinson, C. M. Lepus, Q. Wang, H. Raghu, R. Mao, T. M. Lindstrom, J. Sokolove, Low-grade inflammation as a key mediator of the pathogenesis of osteoarthritis. *Nat. Rev. Rheumatol.* **12**, 580–592 (2016).

11. A. Mahmoudian, L. S. Lohmander, A. Mobasheri, M. Englund, F. P. Luyten, Early-stage symptomatic osteoarthritis of the knee — time for action. *Nat. Rev. Rheumatol.* **17**, 621–632 (2021).

12. M. C. Hochberg, A. Guermazi, H. Guehring, A. Aydemir, S. Wax, P. Fleuranceau-Morel, A. Reinstrup Bihlet, I. Byrjalsen, J. Ragnar Andersen, F. Eckstein, Effect of intra-articular sprifermin vs placebo on femorotibial joint cartilage thickness in patients with osteoarthritis: the FORWARD randomized clinical trial. *JAMA*. **322**, 1360–1370 (2019).

13. P. G. Conaghan, M. A. Bowes, S. R. Kingsbury, A. Brett, G. Guillard, B. Rizoska, N. Sjögren, P. Graham, Å. Jansson, C. Wadell, R. Bethell, J. Öhd, Disease-modifying effects of a novel cathepsin K inhibitor in osteoarthritis. *Ann. Intern. Med.* **172**, 86–95 (2020).

14. J. Sokolove, C. M. Lepus, Role of inflammation in the pathogenesis of osteoarthritis: Latest findings and interpretations. *Ther. Adv. Musculoskelet. Dis.* **5**, 77–94 (2013).

15. R. Liu-Bryan, R. Terkeltaub, Emerging regulators of the inflammatory process in osteoarthritis. *Nat. Rev. Rheumatol.* **11**, 35–44 (2015).

16. T. Hodgkinson, D. C. Kelly, C. M. Curtin, F. J. O'Brien, Mechanosignalling in cartilage: an emerging target for the treatment of osteoarthritis. *Nat. Rev. Rheumatol.* **18**, 67–84 (2022).

17. K. Bacon, M. P. Lavalley, S. R. Jafarzadeh, D. Felson, Does cartilage loss cause pain in osteoarthritis and if so, how much? *Ann. Rheum. Dis.* **79**, 1105–1110 (2020).

18. N. Asgari, H. P. B. Skejoe, S. T. Lillevang, T. Steenstrup, E. Stenager, K. O. Kyvik, Modifications of longitudinally extensive transverse myelitis and brainstem lesions in the course of neuromyelitis optica (NMO): a population-based, descriptive study. *BMC Neurol.* **13**, 33 (2013).

19. M. Favero, R. Ramonda, M. B. Goldring, S. R. Goldring, L. Punzi, Early knee osteoarthritis. *RMD Open*. **1**, 1–7 (2015).

20. X. Ayral, E. H. Pickering, T. G. Woodworth, N. Mackillop, M. Dougados, Synovitis: a potential predictive factor of structural progression of medial tibiofemoral knee osteoarthritis -- results of a 1 year longitudinal arthroscopic study in 422 patients. *Osteoarthr. Cartil.* **13**, 361–367 (2005).

21. M. Maldonado, J. Nam, The role of changes in extracellular matrix of cartilage in the presence of inflammation on the pathology of osteoarthritis. *Biomed Res. Int.* **2013**, 284873 (2013).

22. A. D. Pearle, R. F. Warren, S. A. Rodeo, Basic science of articular cartilage and osteoarthritis. *Clin. Sports Med.* **24**, 1–12 (2005).

23. H. Nagase, M. Kashiwagi, Aggrecanases and cartilage matrix degradation. *Arthritis Res. Ther.* **5**, 94–103 (2003).

24. J. Martel-Pelletier, C. Boileau, J.-P. Pelletier, P. J. Roughley, Cartilage in normal and osteoarthritis conditions. *Best Pract. Res. Clin. Rheumatol.* **22**, 351–384 (2008).

25. M. W. Lark, E. K. Bayne, J. Flanagan, C. F. Harper, L. A. Hoerrner, N. I. Hutchinson, I. I. Singer, S. A. Donatelli, J. R. Weidner, H. R. Williams, R. A. Mumford, L. S. Lohmander, Aggrecan degradation in human cartilage. Evidence for both matrix metalloproteinase and aggrecanase activity in normal, osteoarthritic, and rheumatoid joints. *J. Clin. Invest.* **100**, 93–106 (1997).

26. K. Gelse, E. Pöschl, T. Aigner, Collagens—structure, function, and biosynthesis. *Adv. Drug Deliv. Rev.* **55**, 1531–1546 (2003).

27. N. Verzijl, J. DeGroot, C. Ben Zaken, O. Braun-Benjamin, A. Maroudas, R. A. Bank, J. Mizrahi, C. G. Schalkwijk, S. R. Thorpe, J. W. Baynes, J. W. J. Bijlsma, F. P. J. G. Lafeber, J. M. TeKoppele, Crosslinking by advanced glycation end products increases the stiffness of the collagen network in human articular cartilage: A possible mechanism through which age is a risk factor for osteoarthritis. *Arthritis Rheum.* **46**, 114–123 (2002).

28. M. B. Goldring, S. R. Goldring, Articular cartilage and subchondral bone in the pathogenesis of osteoarthritis. *Ann. N. Y. Acad. Sci.* **1192**, 230–237 (2010).

29. P. M. van der Kraan, W. B. van den Berg, Osteophytes: relevance and biology. *Osteoarthr. Cartil.* **15**, 237–244 (2007).

30. H. Akkiraju, A. Nohe, Role of chondrocytes in cartilage formation, progression of osteoarthritis and cartilage regeneration. *J. Dev. Biol.* **3**, 177–192 (2015).

31. L. J. Sandell, T. Aigner, Articular cartilage and changes in arthritis: cell biology of osteoarthritis. *Arthritis Res. Ther.* **3**, 107 (2001).

32. G. E. Davis, K. J. Bayless, M. J. Davis, G. A. Meininger, Regulation of tissue injury responses by the exposure of matricryptic sites within extracellular matrix molecules. *Am. J. Pathol.* **156**, 1489–1498 (2000).

33. L. E. de Castro Brás, N. G. Frangogiannis, Extracellular matrix-derived peptides in tissue remodeling and fibrosis. *Matrix Biol.* **91–92**, 176–187 (2020).

34. A. E. Rapp, F. Zaucke, Cartilage extracellular matrix-derived matrikines in osteoarthritis. *Am. J. Physiol. Physiol.* **324**, C377–C394 (2023).

35. F. Guilak, L. G. Alexopoulos, M. L. Upton, I. Youn, J. B. Choi, L. Cao, L. A. Setton, M. A. Haider, The pericellular matrix as a transducer of biomechanical and biochemical signals in articular cartilage. *Ann. N. Y. Acad. Sci.* **1068**, 498–512 (2006).

36. M. D. Zack, E. C. Arner, C. P. Anglin, J. T. Alston, A.-M. Malfait, M. D. Tortorella, Identification of fibronectin neoepitopes present in human osteoarthritic cartilage. *Arthritis Rheum.* **54**, 2912–2922 (2006).

37. G. A. Homandberg, R. Meyers, J. M. Williams, Intraarticular injection of fibronectin fragments causes severe depletion of cartilage proteoglycans in vivo. *J. Rheumatol.* **20**, 1378–1382 (1993).

38. K. S. M. Reed, V. Ulici, C. Kim, S. Chubinskaya, R. F. Loeser, D. H. Phanstiel, Transcriptional response of human articular chondrocytes treated with fibronectin fragments: an in vitro model of the osteoarthritis phenotype. *Osteoarthr. Cartil.* **29**, 235–247 (2021).

39. S. T. Wood, D. L. Long, J. A. Reisz, R. R. Yammani, E. A. Burke, C. Klomsiri, L. B. Poole, C. M. Furdui, R. F. Loeser, Cysteine-mediated redox regulation of cell signaling in chondrocytes stimulated with fibronectin fragments. *Arthritis Rheumatol.* **68**, 117–126 (2016).

40. A. S. Lee, M. B. Ellman, D. Yan, J. S. Kroin, B. J. Cole, A. J. van Wijnen, H.-J. Im, A current review of molecular mechanisms regarding osteoarthritis and pain. *Gene*. **527**, 440–447 (2013).

41. H. Li, D. Wang, Y. Yuan, J. Min, New insights on the MMP-13 regulatory network in the pathogenesis of early osteoarthritis. *Arthritis Res. Ther.* **19**, 248 (2017).

42. J. Martel-Pelletier, A. J. Barr, F. M. Cicuttini, P. G. Conaghan, C. Cooper, M. B. Goldring, S. R. Goldring, G. Jones, A. J. Teichtahl, J.-P. Pelletier, Osteoarthritis. *Nat. Rev. Dis. Prim.* **2**, 16072 (2016).

43. R. F. Loeser, Integrins and chondrocyte–matrix interactions in articular cartilage. *Matrix Biol.* **39**, 11–16 (2014).

44. J. Tian, F.-J. Zhang, G.-H. Lei, Role of integrins and their ligands in osteoarthritic cartilage. *Rheumatol. Int.* **35**, 787–798 (2015).

45. F. Iannone, G. Lapadula, The pathophysiology of osteoarthritis. *Aging Clin. Exp. Res.* **15**, 364–372 (2003).

46. A. A. Ansari, S. N. Byrareddy, The role of integrin expressing cells in modulating disease susceptibility and progression. *Int. trends Immun.* **4**, 11–27 (2016).

47. C. Margadant, A. Sonnenberg, Integrin-TGF-beta crosstalk in fibrosis, cancer and wound healing. *EMBO Rep.* **11**, 97–105 (2010).

48. A. C. Finney, K. Y. Stokes, C. B. Pattillo, A. W. Orr, Integrin signaling in atherosclerosis. *Cell. Mol. Life Sci.* **74**, 2263–2282 (2017).

49. R. Zaidel-bar, S. Itzkovitz, A. Ma, R. Iyengar, B. Geiger, Functional atlas of the integrin adhesome. *Nat. Cell Biol.* **9**, 858–867 (2007).

50. R. F. Loeser, Chondrocyte integrin expression and function. *Biorheology*. **37**, 109–116 (2000).

51. C. Woltersdorf, M. Bonk, B. Leitinger, M. Huhtala, J. Käpylä, J. Heino, C. Gil Girol, S. Niland, J. A. Eble, P. Bruckner, R. Dreier, U. Hansen, The binding capacity of α1β1-, α2β1- and α10β1-integrins depends on non-collagenous surface macromolecules rather than the collagens in cartilage fibrils. *Matrix Biol.* **63**, 91–105 (2017).

52. R. F. Loeser, S. Sadiev, L. Tan, M. B. Goldring, Integrin expression by primary and immortalized human chondrocytes: evidence of a differential role for α1β1 and α2β1 integrins in mediating chondrocyte adhesion to types II and VI collagen. *Osteoarthr. Cartil.* **8**, 96–105 (2000).

53. P. Roca-Cusachs, T. Iskratsch, M. P. Sheetz, Finding the weakest link: exploring integrin-mediated mechanical molecular pathways. *J. Cell Sci.* **125**, 3025–3038 (2012).

54. I. P. Geoghegan, D. A. Hoey, L. M. McNamara, Integrins in osteocyte biology and mechanotransduction. *Curr. Osteoporos. Rep.* **17**, 195–206 (2019).

55. K. W. Jang, J. A. Buckwalter, J. A. Martin, Inhibition of cell-matrix adhesions prevents cartilage chondrocyte death following impact injury. *J. Orthop. Res. Off. Publ. Orthop. Res. Soc.* **32**, 448–454 (2014).

56. F. Kong, Z. Li, W. M. Parks, D. W. Dumbauld, A. J. García, A. P. Mould, M. J. Humphries, C. Zhu, Cyclic mechanical reinforcement of integrin–ligand interactions. *Mol. Cell*. **49**, 1060–1068 (2013).

57. A. E. Rapp, F. Zaucke, Cartilage extracellular matrix-derived matrikines in osteoarthritis. *Am. J. Physiol. Physiol.* **324**, C377–C394 (2022).

58. M. Kapoor, J. Martel-Pelletier, D. Lajeunesse, J.-P. Pelletier, H. Fahmi, Role of proinflammatory cytokines in the pathophysiology of osteoarthritis. *Nat. Rev. Rheumatol.* **7**, 33–42 (2011).

59. E. C. Arner, M. D. Tortorella, Signal transduction through chondrocyte integrin receptors induces matrix metalloproteinase synthesis and synergizes with interleukin-1. *Arthritis Rheum.* **38**, 1304–1314 (1995).

60. G. A. Homandberg, Potential regulation of cartilage metabolism in osteoarthritis by fibronectin fragments. *Front. Biosci.* **4**, D713-730 (1999).

61. C. B. Forsyth, J. Pulai, R. F. Loeser, Fibronectin fragments and blocking antibodies to α2β1 and α5β1 integrins stimulate mitogen-activated protein kinase signaling and increase collagenase 3 (matrix metalloproteinase 13) production by human articular chondrocytes. *Arthritis Rheum.* **46**, 2368–2376 (2002).

62. T. Gemba, J. Valbracht, S. Alsalameh, M. Lotz, Focal adhesion kinase and mitogen-activated protein kinases are involved in chondrocyte activation by the 29-kDa amino-terminal fibronectin fragment. *J. Biol. Chem.* **277**, 907–911 (2002).

63. M. C. Castaño Betancourt, F. Cailotto, H. J. Kerkhof, F. M. F. Cornelis, S. A. Doherty, D. J. Hart, A. Hofman, F. P. Luyten, R. A. Maciewicz, M. Mangino, S. Metrustry, K. Muir, M. J. Peters, F. Rivadeneira, M. Wheeler, W. Zhang, N. Arden, T. D. Spector, A. G. Uitterlinden, M. Doherty, R. J. U. Lories, A. M. Valdes, J. B. J. van Meurs, Genome-wide association and functional studies identify the DOT1L gene to be involved in cartilage thickness and hip osteoarthritis. *Proc. Natl. Acad. Sci. U. S. A.* **109**, 8218–8223 (2012).

64. J. Bernhard, J. Ferguson, B. Rieder, P. Heimel, T. Nau, S. Tangl, H. Redl, G. Vunjak-Novakovic, Tissue-engineered hypertrophic chondrocyte grafts enhanced long bone repair. *Biomaterials*. **139**, 202–212 (2017).

65. D. Sheppard, In vivo functions of integrins: lessons from null mutations in mice. *Matrix Biol.* **19**, 203–209 (2000).

66. M. E. Candela, C. Wang, A. T. Gunawardena, K. Zhang, L. Cantley, R. Yasuhara, Y. Usami, N. Francois, M. Iwamoto, A. Van Der Flier, Y. Zhang, L. Qin, L. Han, M. Enomoto-Iwamoto, Alpha 5 integrin mediates osteoarthritic changes in mouse knee joints. *PLoS One*. **11**, 1–14 (2016).

67. N. Gerwin, C. Scotti, C. Halleux, M. Fornaro, J. Elliott, Y. Zhang, K. Johnson, J. Shi, S. Walter, Y. Li, C. Jacobi, N. Laplanche, M. Belaud, J. Paul, G. Glowacki, T. Peters, K. A. J. Wharton, I. Vostiar, F. Polus, I. Kramer, S. Guth, A. Seroutou, S. Choudhury, D. Laurent, J. Gimbel, J. Goldhahn, M. Schieker, S. Brachat, R. Roubenoff, M. Kneissel, Angiopoietin-like 3-derivative LNA043 for cartilage regeneration in osteoarthritis: a randomized phase 1 trial. *Nat. Med.* **28**, 2633–2645 (2022).

68. Q. Wang, K. Onuma, C. Liu, H. Wong, M. S. Bloom, E. E. Elliott, R. R. L. Cao, N. Hu, N. Lingampalli, O. Sharpe, X. Zhao, D. H. Sohn, C. M. Lepus, J. Sokolove, R. Mao, C. T. Cisar, H. Raghu, C. R. Chu, N. J. Giori, S. B. Willingham, S. S. Prohaska, Z. Cheng, I. L. Weissman, W. H. Robinson, Dysregulated integrin αVβ3 and CD47 signaling promotes joint inflammation, cartilage breakdown, and progression of osteoarthritis. *JCI Insight*. **4**,

e128616 (2019).

69. F. Song, X. Mao, J. Dai, B. Shan, Z. Zhou, Y. Kang, Integrin αVβ3 signaling in the progression of osteoarthritis induced by excessive mechanical stress. *Inflammation*. **46**, 739–751 (2023).

70. M. G. Attur, M. N. Dave, R. M. Clancy, I. R. Patel, S. B. Abramson, A. R. Amin, Functional genomic analysis in arthritis-affected cartilage: yin-yang regulation of inflammatory mediators by alpha 5 beta 1 and alpha V beta 3 integrins. *J. Immunol.* **164**, 2684–2691 (2000).

71. D. M. Sumsuzzman, Z. A. Khan, J. Choi, Y. Hong, Assessment of functional roles and therapeutic potential of integrin receptors in osteoarthritis: A systematic review and meta-analysis of preclinical studies. *Ageing Res. Rev.* **81**, 101729 (2022).

72. Q. Yao, X. Wu, C. Tao, W. Gong, M. Chen, M. Qu, Y. Zhong, T. He, S. Chen, G. Xiao, Osteoarthritis: pathogenic signaling pathways and therapeutic targets. *Signal Transduct. Target. Ther.* **8**, 56 (2023).

73. T. K. Rudolph, B. A. Freeman, Transduction of redox signaling by electrophile-protein reactions. *Sci. Signal.* **2**, re7 (2009).

74. P. Sharma, A. B. Jha, R. S. Dubey, M. Pessarakli, Reactive oxygen species, oxidative damage, and antioxidative defense mechanism in plants under stressful conditions. *J. Bot.* **2012**, 1–26 (2012).

75. J. Zhang, X. Wang, V. Vikash, Q. Ye, D. Wu, Y. Liu, W. Dong, ROS and ROS-mediated cellular signaling. *Oxid. Med. Cell. Longev.* **2016**, 4350965 (2016).

76. L. B. Poole, K. J. Nelson, Discovering mechanisms of signaling-mediated cysteine oxidation. *Curr. Opin. Chem. Biol.* **12**, 18–24 (2008).

77. N. Di Marzo, E. Chisci, R. Giovannoni, The role of hydrogen peroxide in redox-dependent signaling: homeostatic and pathological responses in mammalian cells. *Cells*. **7**, 156 (2018).

78. G. Svineng, C. Ravuri, O. Rikardsen, N.-E. Huseby, J.-O. Winberg, The role of reactive oxygen species in integrin and matrix metalloproteinase expression and function. *Connect. Tissue Res.* **49**, 197–202 (2008).

79. T.-C. Meng, T. Fukada, N. K. Tonks, Reversible oxidation and inactivation of protein tyrosine phosphatases in vivo. *Mol. Cell*. **9**, 387–399 (2002).

80. C. Lennicke, J. Rahn, R. Lichtenfels, L. A. Wessjohann, B. Seliger, Hydrogen peroxide – production, fate and role in redox signaling of tumor cells. *Cell Commun. Signal.* **13**, 39 (2015).

81. R. D. M. Travasso, F. Sampaio Dos Aidos, A. Bayani, P. Abranches, A. Salvador, Localized redox relays as a privileged mode of cytoplasmic hydrogen peroxide signaling. *Redox Biol.* **12**, 233–245 (2017).

82. C. C. Winterbourn, Reconciling the chemistry and biology of reactive oxygen species. *Nat. Chem. Biol.* **4**, 278–286 (2008).

83. H. Sies, V. V Belousov, N. S. Chandel, M. J. Davies, D. P. Jones, G. E. Mann, M. P. Murphy, M. Yamamoto, C. Winterbourn, Defining roles of specific reactive oxygen species (ROS) in cell biology and physiology. *Nat. Rev. Mol. Cell Biol.* **23**, 499–515 (2022).

84. M. Schieber, N. S. Chandel, ROS function in redox signaling and oxidative stress. *Curr. Biol.* **24**, R453-462 (2014).

85. J. Checa, J. M. Aran, Reactive oxygen species: drivers of physiological and pathological processes. *J. Inflamm. Res.* **13**, 1057–1073 (2020).

86. D. I. Brown, K. K. Griendling, Regulation of signal transduction by reactive oxygen species in the cardiovascular system. *Circ. Res.* **116**, 531–549 (2015).

87. N. Apostolova, V. M. Victor, Molecular strategies for targeting antioxidants to mitochondria: therapeutic implications. *Antioxid. Redox Signal.* **22**, 686–729 (2015).

88. N. M. Mishina, P. A. Tyurin-Kuzmin, K. N. Markvicheva, A. V. Vorotnikov, V. A. Tkachuk, V. Laketa, C. Schultz, S. Lukyanov, V. V. Belousov, Does cellular hydrogen peroxide diffuse or act locally? *Antioxid. Redox Signal.* **14**, 1–7 (2011).

89. G. Pizzino, N. Irrera, M. Cucinotta, G. Pallio, F. Mannino, V. Arcoraci, F. Squadrito, D. Altavilla, A. Bitto, Oxidative stress: harms and benefits for human health. *Oxid. Med. Cell. Longev.* **2017**, 8416763 (2017).

90. C. Espinosa-Diez, V. Miguel, D. Mennerich, T. Kietzmann, P. Sánchez-Pérez, S. Cadenas, S. Lamas, Antioxidant responses and cellular adjustments to oxidative stress. *Redox Biol.* **6**, 183–197 (2015).

91. B. Perillo, M. Di Donato, A. Pezone, E. Di Zazzo, P. Giovannelli, G. Galasso, G. Castoria, A. Migliaccio, ROS in cancer therapy: the bright side of the moon. *Exp. Mol. Med.* **52**, 192–203 (2020).

92. S. J. Forrester, D. S. Kikuchi, M. S. Hernandes, Q. Xu, K. K. Griendling, Reactive oxygen species in metabolic and inflammatory signaling. *Circ. Res.* **122**, 877–902 (2018).

93. A. R. Bourgonje, M. Feelisch, K. N. Faber, A. Pasch, G. Dijkstra, H. van Goor, Oxidative stress and redox-modulating therapeutics in inflammatory bowel disease. *Trends Mol. Med.* **26**, 1034–1046 (2020).

94. D. F. Patel, T. Peiró, A. Shoemark, S. Akthar, S. A. Walker, A. M. Grabiec, P. L. Jackson, T. Hussell, A. Gaggar, X. Xu, J. L. Trevor, J. Li, C. Steele, G. Tavernier, J. E. Blalock, R. M. Niven, L. G. Gregory, A. Simpson, C. M. Lloyd, R. J. Snelgrove, An extracellular matrix fragment drives epithelial remodeling and airway hyperresponsiveness. *Sci. Transl. Med.* **10**, eaaq0693 (2018).

95. C. S. Hahn, D. W. Scott, X. Xu, M. A. Roda, G. A. Payne, J. M. Wells, L. Viera, C. J. Winstead, P. Bratcher, R. W. Sparidans, F. A. Redegeld, P. L. Jackson, G. Folkerts, J. E.

Blalock, R. P. Patel, A. Gaggar, The matrikine N-α-PGP couples extracellular matrix fragmentation to endothelial permeability. *Sci. Adv.* **1**, e1500175 (2015).

96. N. G. Frangogiannis, The extracellular matrix in myocardial injury, repair, and remodeling. *J. Clin. Invest.* **127**, 1600–1612 (2017).

97. G. A. Rosenberg, Matrix metalloproteinases and their multiple roles in neurodegenerative diseases. *Lancet Neurol.* **8**, 205–216 (2009).

98. S. Ricard-Blum, R. Salza, Matricryptins and matrikines: Biologically active fragments of the extracellular matrix. *Exp. Dermatol.* **23**, 457–463 (2014).

99. M. L. Barilla, S. E. Carsons, Fibronectin fragments and their role in inflammatory arthritis. *Semin. Arthritis Rheum.* **29**, 252–265 (2000).

100. P. Lu, K. Takai, V. M. Weaver, Z. Werb, Extracellular matrix degradation and remodeling in development and disease. *Cold Spring Harb. Perspect. Biol.* **3**, a005058 (2011).

101. M. Larsen, V. V. Artym, J. A. Green, K. M. Yamada, The matrix reorganized: extracellular matrix remodeling and integrin signaling. *Curr. Opin. Cell Biol.* **18**, 463–471 (2006).

102. S. Ricard-Blum, S. D. Vallet, Fragments generated upon extracellular matrix remodeling: Biological regulators and potential drugs. *Matrix Biol.* **75–76**, 170–189 (2019).

103. P. Moreno-Layseca, J. Icha, H. Hamidi, J. Ivaska, Integrin trafficking in cells and tissues. *Nat. Cell Biol.* **21**, 122–132 (2019).

104. N. Jariwala, M. Ozols, M. Bell, E. Bradley, A. Gilmore, L. Debelle, M. J. Sherratt, Matrikines as mediators of tissue remodelling. *Adv. Drug Deliv. Rev.* **185**, 114240 (2022).

105. J. Alanko, A. Mai, G. Jacquemet, K. Schauer, R. Kaukonen, M. Saari, B. Goud, J. Ivaska, Integrin endosomal signalling suppresses anoikis. *Nat. Cell Biol.* **17**, 1412–1421 (2015).

106. G. P. F. Nader, E. J. Ezratty, G. G. Gundersen, FAK, talin and PIPKI 3 regulate endocytosed integrin activation to polarize focal adhesion assembly. *Nat. Cell Biol.* **18**, 491–503 (2016).

107. H. Hamidi, J. Ivaska, Every step of the way: Integrins in cancer progression and metastasis. *Nat. Rev. Cancer*. **18**, 533–548 (2018).

108. J. Z. Kechagia, J. Ivaska, P. Roca-Cusachs, Integrins as biomechanical sensors of the microenvironment. *Nat. Rev. Mol. Cell Biol.* **20**, 457–473 (2019).

109. J. D. Humphrey, E. R. Dufresne, M. A. Schwartz, Mechanotransduction and extracellular matrix homeostasis. *Nat. Rev. Mol. Cell Biol.* **15**, 802–812 (2014).

110. P. Kanchanawong, D. A. Calderwood, Organization, dynamics and mechanoregulation of integrin-mediated cell–ECM adhesions. *Nat. Rev. Mol. Cell Biol.* **24**, 142–161 (2023).

111. D. Heinegård, T. Saxne, The role of the cartilage matrix in osteoarthritis. *Nat. Rev. Rheumatol.* **7**, 50–56 (2011).

112. R. F. Loeser, S. R. Goldring, C. R. Scanzello, M. B. Goldring, Osteoarthritis: A disease of the joint as an organ. *Arthritis Rheum.* **64**, 1697–1707 (2012).

113. M. B. Goldring, The role of the chondrocyte in osteoarthritis. *Arthritis Rheum.* **43**, 1916–1926 (2000).

114. D. Xie, R. Meyers, G. A. Homandberg, Fibronectin fragments in osteoarthritic synovial fluid. *J. Rheumatol.* **19**, 1448–1452 (1992).

115. G. A. Homandberg, C. Wen, F. Hui, Cartilage damaging activities of fibronectin fragments derived from cartilage and synovial fluid. *Osteoarthr. Cartil.* **6**, 231–244 (1998).

116. S. Grau, P. J. Richards, B. Kerr, C. Hughes, B. Caterson, A. S. Williams, U. Junker, S. A. Jones, T. Clausen, M. Ehrmann, The role of human HtrA1 in arthritic disease. *J. Biol. Chem.* **281**, 6124–6129 (2006).

117. H. A. Wieland, M. Michaelis, B. J. Kirschbaum, K. A. Rudolphi, Osteoarthritis - An untreatable disease? *Nat. Rev. Drug Discov.* **4**, 331–344 (2005).

118. A. Latourte, M. Kloppenburg, P. Richette, Emerging pharmaceutical therapies for osteoarthritis. *Nat. Rev. Rheumatol.* **16**, 673–688 (2020).

119. D. Gregg, D. D. de Carvalho, H. Kovacic, Integrins and coagulation: a role for ROS/redox signaling? *Antioxid. Redox Signal.* **6**, 757–764 (2004).

120. Z. Xu, Y. Liang, M. K. Delaney, Y. Zhang, K. Kim, J. Li, Y. Bai, J. Cho, M. Ushio-Fukai, N. Cheng, X. Du, Shear and integrin outside-in signaling activate NADPH-oxidase 2 to promote platelet activation. *Arterioscler. Thromb. Vasc. Biol.* **41**, 1638–1653 (2021).

121. K. M. Holmström, T. Finkel, Cellular mechanisms and physiological consequences of redox-dependent signalling. *Nat. Rev. Mol. Cell Biol.* **15**, 411–421 (2014).

122. R. Tsutsumi, J. Harizanova, R. Stockert, K. Schröder, P. I. H. Bastiaens, B. G. Neel, Assay to visualize specific protein oxidation reveals spatio-temporal regulation of SHP2. *Nat. Commun.* **8**, 466 (2017).

123. J. B. Behring, S. van der Post, A. D. Mooradian, M. J. Egan, M. I. Zimmerman, J. L. Clements, G. R. Bowman, J. M. Held, Spatial and temporal alterations in protein structure by EGF regulate cryptic cysteine oxidation. *Sci. Signal.* **13**, eaay7315 (2020).

124. D. E. Heppner, C. M. Dustin, C. Liao, M. Hristova, C. Veith, A. C. Little, B. A. Ahlers, S. L. White, B. Deng, Y.-W. Lam, J. Li, A. van der Vliet, Direct cysteine sulfenylation drives activation of the Src kinase. *Nat. Commun.* **9**, 4522 (2018).

125. D. E. Heppner, Y. M. W. Janssen-Heininger, A. van der Vliet, The role of sulfenic acids in cellular redox signaling: Reconciling chemical kinetics and molecular detection strategies. *Arch. Biochem. Biophys.* **616**, 40–46 (2017).

126. M. Obara, M. S. Kang, K. M. Yamada, Site-directed mutagenesis of the cell-binding domain of human fibronectin: Separable, synergistic sites mediate adhesive function. *Cell*. **53**, 649–657 (1988).

127. S. Schumacher, D. Dedden, R. V. Nunez, K. Matoba, J. Takagi, C. Biertümpfel, N. Mizuno, Structural insights into integrin α5β1 opening by fibronectin ligand. *Sci. Adv.* **7**, eabe9716 (2021).

128. T. Pap, A. Korb-Pap, Cartilage damage in osteoarthritis and rheumatoid arthritis - Two unequal siblings. *Nat. Rev. Rheumatol.* **11**, 606–615 (2015).

129. X. Zhang, C. T. Chen, M. Bhargava, P. A. Torzilli, A comparative study of fibronectin cleavage by MMP-1, -3, -13, and -14. *Cartilage*. **3**, 267–277 (2012).

130. E. E. To, R. Vlahos, R. Luong, M. L. Halls, P. C. Reading, P. T. King, C. Chan, G. R. Drummond, C. G. Sobey, B. R. S. Broughton, M. R. Starkey, R. van der Sluis, S. R. Lewin, S. Bozinovski, L. A. J. O'Neill, T. Quach, C. J. H. Porter, D. A. Brooks, J. J. O'Leary, S. Selemidis, Endosomal NOX2 oxidase exacerbates virus pathogenicity and is a target for antiviral therapy. *Nat. Commun.* **8**, 69 (2017).

131. R. Pankov, K. M. Yamada, Fibronectin at a glance. *J. Cell Sci.* **115**, 3861–3863 (2002).

132. B. D. Grant, J. G. Donaldson, Pathways and mechanisms of endocytic recycling. *Nat. Rev. Mol. Cell Biol.* **10**, 597–608 (2009).

133. M. Shafaq-Zadah, C. S. Gomes-Santos, S. Bardin, P. Maiuri, M. Maurin, J. Iranzo, A. Gautreau, C. Lamaze, P. Caswell, B. Goud, L. Johannes, Persistent cell migration and adhesion rely on retrograde transport of β1 integrin. *Nat. Cell Biol.* **18**, 54–64 (2016).

134. M. Del Carlo, D. Schwartz, E. A. Erickson, R. F. Loeser, Endogenous production of reactive oxygen species is required for stimulation of human articular chondrocyte matrix metalloproteinase production by fibronectin fragments. *Free Radic. Biol. Med.* **42**, 1350–1358 (2007).

135. D. I. Brown, K. K. Griendling, Nox proteins in signal transduction. *Free Radic. Biol. Med.* **47**, 1239–1253 (2009).

136. K. Bedard, K. H. Krause, The NOX family of ROS-generating NADPH oxidases: Physiology and pathophysiology. *Physiol. Rev.* **87**, 245–313 (2007).

137. K. Kasahara, Y. Nakayama, A. Kihara, D. Matsuda, K. Ikeda, T. Kuga, Y. Fukumoto, Y. Igarashi, N. Yamaguchi, Rapid trafficking of c-Src, a non-palmitoylated Src-family kinase, between the plasma membrane and late endosomes/lysosomes. *Exp. Cell Res.* **313**, 2651–2666 (2007).

138. E. Sandilands, M. C. Frame, Endosomal trafficking of Src tyrosine kinase. *Trends Cell Biol.* **18**, 322–329 (2008).

139. E. Sandilands, C. Cans, V. J. Fincham, V. G. Brunton, H. Mellor, G. C. Prendergast, J. C. Norman, G. Superti-Furga, M. C. Frame, RhoB and actin polymerization coordinate Src activation with endosome-mediated delivery to the membrane. *Dev. Cell*. **7**, 855–869 (2004).

140. K. M. Fisch, R. Gamini, O. Alvarez-Garcia, R. Akagi, M. Saito, Y. Muramatsu, T. Sasho, J. A. Koziol, A. I. Su, M. K. Lotz, Identification of transcription factors responsible for

dysregulated networks in human osteoarthritis cartilage by global gene expression analysis. *Osteoarthr. Cartil.* **26**, 1531–1538 (2018).

141. W. Fu, A. Hettinghouse, Y. Chen, W. Hu, X. Ding, M. Chen, Y. Ding, J. Mundra, W. Song, R. Liu, Y. S. Yi, M. Attur, J. Samuels, E. Strauss, P. Leucht, R. Schwarzkopf, C. J. Liu, 14-3-3 epsilon is an intracellular component of TNFR2 receptor complex and its activation protects against osteoarthritis. *Ann. Rheum. Dis.* **80**, 1615–1627 (2021).

142. Q. Ji, Y. Zheng, G. Zhang, Y. Hu, X. Fan, Y. Hou, L. Wen, L. Li, Y. Xu, Y. Wang, F. Tang, Single-cell RNA-seq analysis reveals the progression of human osteoarthritis. *Ann. Rheum. Dis.* **78**, 100–110 (2019).

143. A. Arjonen, J. Alanko, S. Veltel, J. Ivaska, Distinct recycling of active and inactive β1 integrins. *Traffic*. **13**, 610–625 (2012).

144. F. D. Oakley, D. Abbott, Q. Li, J. F. Engelhardt, Signaling components of redox active endosomes: The redoxosomes. *Antioxidants Redox Signal.* **11**, 1313–1333 (2009).

145. Q. Li, M. M. Harraz, W. Zhou, L. N. Zhang, W. Ding, Y. Zhang, T. Eggleston, C. Yeaman, B. Banfi, J. F. Engelhardt, Nox2 and Rac1 regulate H2O2 -dependent recruitment of TRAF6 to endosomal interleukin-1 receptor complexes. *Mol. Cell. Biol.* **26**, 140–154 (2006).

146. N. Y. Spencer, J. F. Engelhardt, The basic biology of redoxosomes in cytokine-mediated signal transduction and implications for disease-specific therapies. *Biochemistry*. **53**, 1551–1564 (2014).

147. N. Müller-Calleja, D. Manukyan, A. Canisius, D. Strand, K. J. Lackner, Hydroxychloroquine inhibits proinflammatory signalling pathways by targeting endosomal NADPH oxidase. *Ann. Rheum. Dis.* **76**, 891–897 (2017).

148. K. Li, Y. Zhang, Y. Zhang, W. Jiang, J. Shen, S. Xu, D. Cai, J. Shen, B. Huang, M. Li, Q. Song, Y. Jiang, A. Liu, X. Bai, Tyrosine kinase Fyn promotes osteoarthritis by activating the β-catenin pathway. *Ann. Rheum. Dis.* **77**, 935–943 (2018).

149. M. N. Ferrao Blanco, H. Domenech Garcia, L. Legeai-Mallet, G. J. V. M. van Osch, Tyrosine kinases regulate chondrocyte hypertrophy: promising drug targets for Osteoarthritis. *Osteoarthr. Cartil.* **29**, 1389–1398 (2021).

150. T. Tao, D. Luo, C. Gao, H. Liu, Z. Lei, W. Liu, C. Zhou, D. Qi, Z. Deng, X. Sun, J. Xiao, Src homology 2 domain-containing protein tyrosine phosphatase promotes inflammation and accelerates osteoarthritis by activating β-catenin. *Front. Cell Dev. Biol.* **9**, 646386 (2021).

151. F. Shi, J. Sottile, MT1-MMP regulates the turnover and endocytosis of extracellular matrix fibronectin. *J. Cell Sci.* **124**, 4039–4050 (2011).

152. R. Joshi, E. Goihberg, W. Ren, M. Pilichowska, P. Mathew, Proteolytic fragments of fibronectin function as matrikines driving the chemotactic affinity of prostate cancer cells to human bone marrow mesenchymal stromal cells via the α5β1 integrin. *Cell Adhes. Migr.* **11**, 305–315 (2017).

153. G. A. Homandberg, V. Costa, C. Wen, Fibronectin fragments active in chondrocytic chondrolysis can be chemically cross-linked to the alpha5 integrin receptor subunit. *Osteoarthr. Cartil.* **10**, 938–949 (2002).

154. C. Bonnans, J. Chou, Z. Werb, Remodelling the extracellular matrix in development and disease. *Nat. Rev. Mol. Cell Biol.* **15**, 786–801 (2014).

155. T. M. Dankovich, R. Kaushik, L. H. M. Olsthoorn, G. C. Petersen, P. E. Giro, V. Kluever, P. Agüi-Gonzalez, K. Grewe, G. Bao, S. Beuermann, H. A. Hadi, J. Doeren, S. Klöppner, B. H. Cooper, A. Dityatev, S. O. Rizzoli, Extracellular matrix remodeling through endocytosis and resurfacing of Tenascin-R. *Nat. Commun.* **12**, 7129 (2021).

156. D. J. Huey, J. C. Hu, K. a Athanasiou, Unlike bone, cartilage regeneration remains elusive. *Science.* **6933**, 917–921 (2012).

157. X. Chevalier, Fibronectin, cartilage, and osteoarthritis. *Semin. Arthritis Rheum.* **22**, 307–318 (1993).

158. C. Zhou, H. Zheng, J. A. Buckwalter, J. A. Martin, Enhanced phagocytic capacity endows chondrogenic progenitor cells with a novel scavenger function within injured cartilage. *Osteoarthr. Cartil.* **24**, 1648–1655 (2016).

159. D. D. Jensen, T. Lieu, M. L. Halls, N. A. Veldhuis, W. L. Imlach, Q. N. Mai, D. P. Poole, T. Quach, L. Aurelio, J. Conner, C. K. Herenbrink, N. Barlow, J. S. Simpson, M. J. Scanlon, B. Graham, A. McCluskey, P. J. Robinson, V. Escriou, R. Nassini, S. Materazzi, P. Geppetti, G. A. Hicks, M. J. Christie, C. J. H. Porter, M. Canals, N. W. Bunnett, Neurokinin 1 receptor signaling in endosomes mediates sustained nociception and is a viable therapeutic target for prolonged pain relief. *Sci. Transl. Med.* **9**, eaal3447 (2017).

160. N. N. Jimenez-Vargas, J. Gong, M. J. Wisdom, D. D. Jensen, R. Latorre, A. Hegron, S. Teng, J. J. DiCello, P. Rajasekhar, N. A. Veldhuis, S. E. Carbone, Y. Yu, C. Lopez-Lopez, J. Jaramillo-Polanco, M. Canals, D. E. Reed, A. E. Lomax, B. L. Schmidt, K. W. Leong, S. J. Vanner, M. L. Halls, N. W. Bunnett, D. P. Poole, Endosomal signaling of delta opioid receptors is an endogenous mechanism and therapeutic target for relief from inflammatory pain. *Proc. Natl. Acad. Sci. U. S. A.* **117**, 15281–15292 (2020).

161. C. Muehleman, D. Bareither, K. Huch, A. A. Cole, K. E. Kuettner, Prevalence of degenerative morphological changes in the joints of the lower extremity. *Osteoarthr. Cartil.* **5**, 23–37 (1997).

162. A. Subramanian, P. Tamayo, V. K. Mootha, S. Mukherjee, B. L. Ebert, M. A. Gillette, A. Paulovich, S. L. Pomeroy, T. R. Golub, E. S. Lander, J. P. Mesirov, Gene set enrichment analysis: A knowledge-based approach for interpreting genome-wide expression profiles. *Proc. Natl. Acad. Sci. U. S. A.* **102**, 15545–15550 (2005).

163. T. Stuart, A. Butler, P. Hoffman, C. Hafemeister, E. Papalexi, W. M. Mauck, Y. Hao, M. Stoeckius, P. Smibert, R. Satija, Comprehensive Integration of Single-Cell Data. *Cell.* **177**, 1888–1902 (2019).

164. I. Korsunsky, N. Millard, J. Fan, K. Slowikowski, F. Zhang, K. Wei, Y. Baglaenko, M. Brenner, P. ru Loh, S. Raychaudhuri, Fast, sensitive and accurate integration of single-

cell data with Harmony. *Nat. Methods*. **16**, 1289–1296 (2019).

165. J. Alquicira-Hernandez, J. E. Powell, Nebulosa recovers single-cell gene expression signals by kernel density estimation. *Bioinformatics*. **37**, 2485–2487 (2021).

166. A. Dean, D. Voss, Eds., *Design and Analysis of Experiments* (Springer-Verlag, New York, 1999; http://link.springer.com/10.1007/b97673), *Springer Texts in Statistics*.

167. W. S. To, K. S. Midwood, Plasma and cellular fibronectin: distinct and independent functions during tissue repair. *Fibrogenesis Tissue Repair*. **4**, 21 (2011).

168. S. Pérez-García, M. Carrión, I. Gutiérrez-Cañas, R. Villanueva-Romero, D. Castro, C. Martínez, I. González-Álvaro, F. J. Blanco, Y. Juarranz, R. P. Gomariz, Profile of matrix-remodeling proteinases in osteoarthritis: impact of fibronectin. *Cells*. **9**, 40 (2019).

169. E. S. White, A. F. Muro, Fibronectin splice variants: understanding their multiple roles in health and disease using engineered mouse models. *IUBMB Life*. **63**, 538–546 (2011).

170. T. Yasuda, Cartilage destruction by matrix degradation products. *Mod. Rheumatol.* **16**, 197–205 (2006).

171. L. M. Maurer, W. Ma, D. F. Mosher, Dynamic structure of plasma fibronectin. *Crit. Rev. Biochem. Mol. Biol.* **51**, 213–227 (2015).

172. E. Cukierman, R. Pankov, K. M. Yamada, Cell interactions with three-dimensional matrices. *Curr. Opin. Cell Biol.* **14**, 633–640 (2002).

173. J. K. Mouw, G. Ou, V. M. Weaver, Extracellular matrix assembly: a multiscale deconstruction. *Nat. Rev. Mol. Cell Biol.* **15**, 771–785 (2014).

174. Y. Mao, J. E. Schwarzbauer, Fibronectin fibrillogenesis, a cell-mediated matrix assembly process. *Matrix Biol.* **24**, 389–399 (2005).

175. I. Wierzbicka-Patynowski, J. E. Schwarzbauer, The ins and outs of fibronectin matrix assembly. *J. Cell Sci.* **116**, 3269–3276 (2003).

176. H. S. Hwang, S. J. Park, E. J. Cheon, M. H. Lee, H. A. Kim, Fibronectin fragment-induced expression of matrix metalloproteinases is mediated by MyD88-dependent TLR-2 signaling pathway in human chondrocytes. *Arthritis Res. Ther.* **17**, 320 (2015).

177. M. Shakibaei, C. Csaki, A. Mobasheri, Diverse roles of integrin receptors in articular cartilage. *Adv. Anat. Embryol. Cell Biol.* **197**, 1–60 (2008).

178. T. Klein, R. Bischoff, Physiology and pathophysiology of matrix metalloproteases. *Amino Acids*. **41**, 271–290 (2011).

179. Q. Hu, M. Ecker, Overview of MMP-13 as a promising target for the treatment of osteoarthritis. *Int. J. Mol. Sci.* **22**, 1742 (2021).

180. N. Cui, M. Hu, R. A. Khalil, in *Progress in molecular biology and translational science* (Netherlands, 2017; https://linkinghub.elsevier.com/retrieve/pii/S1877117317300327), vol. 147, pp. 1–73.

181. H. Laronha, J. Caldeira, Structure and function of human matrix metalloproteinases. *Cells*. **9**, 1076 (2020).

182. R. Visse, H. Nagase, Matrix metalloproteinases and tissue inhibitors of metalloproteinases: structure, function, and biochemistry. *Circ. Res.* **92**, 827–839 (2003).

183. M. F. Leeman, S. Curran, G. I. Murray, The structure, regulation, and function of human matrix metalloproteinase-13. *Crit. Rev. Biochem. Mol. Biol.* **37**, 149–166 (2002).

184. G. Tardif, P. Reboul, J.-P. Pelletier, J. Martel-Pelletier, Ten years in the life of an enzyme: the story of the human MMP-13 (collagenase-3). *Mod. Rheumatol.* **14**, 197–204 (2004).

185. K. Yamamoto, G. Murphy, L. Troeberg, Extracellular regulation of metalloproteinases. *Matrix Biol.* **44–46**, 255–263 (2015).

186. E. Hadler-Olsen, B. Fadnes, I. Sylte, L. Uhlin-Hansen, J.-O. Winberg, Regulation of matrix metalloproteinase activity in health and disease. *FEBS J.* **278**, 28–45 (2011).

187. O. McClurg, R. Tinson, L. Troeberg, Targeting cartilage degradation in osteoarthritis. *Pharmaceuticals*. **14**, 126 (2021).

188. W. M. Oo, D. J. Hunter, Repurposed and investigational disease-modifying drugs in osteoarthritis (DMOADs). *Ther. Adv. Musculoskelet. Dis.* **14**, 1759720X221090297 (2022).

189. M. P. Murphy, H. Bayir, V. Belousov, C. J. Chang, K. J. A. Davies, M. J. Davies, T. P. Dick, T. Finkel, H. J. Forman, Y. Janssen-Heininger, D. Gems, V. E. Kagan, B. Kalyanaraman, N.-G. Larsson, G. L. Milne, T. Nyström, H. E. Poulsen, R. Radi, H. Van Remmen, P. T. Schumacker, P. J. Thornalley, S. Toyokuni, C. C. Winterbourn, H. Yin, B. Halliwell, Guidelines for measuring reactive oxygen species and oxidative damage in cells and in vivo. *Nat. Metab.* **4**, 651–662 (2022).

190. F. Q. Schafer, G. R. Buettner, Redox environment of the cell as viewed through the redox state of the glutathione disulfide/glutathione couple. *Free Radic. Biol. Med.* **30**, 1191–1212 (2001).

191. C. Lennicke, H. M. Cochemé, Redox metabolism: ROS as specific molecular regulators of cell signaling and function. *Mol. Cell*. **81**, 3691–3707 (2021).

192. C. Giorgi, S. Missiroli, S. Patergnani, J. Duszynski, M. R. Wieckowski, P. Pinton, Mitochondria-associated membranes: composition, molecular mechanisms, and physiopathological implications. *Antioxid. Redox Signal.* **22**, 995–1019 (2015).

193. E. D. Yoboue, R. Sitia, T. Simmen, Redox crosstalk at endoplasmic reticulum (ER) membrane contact sites (MCS) uses toxic waste to deliver messages. *Cell Death Dis.* **9**, 331 (2018).

194. B. S. C. Silva, L. DiGiovanni, R. Kumar, R. E. Carmichael, P. K. Kim, M. Schrader, Maintaining social contacts: The physiological relevance of organelle interactions. *Biochim. Biophys. acta. Mol. cell Res.* **1867**, 118800 (2020).

195. G. Filomeni, G. Rotilio, M. R. Ciriolo, Disulfide relays and phosphorylative cascades: partners in redox-mediated signaling pathways. *Cell Death Differ.* **12**, 1555–1563 (2005).

196. C. E. Paulsen, K. S. Carroll, Cysteine-mediated redox signaling: chemistry, biology, and tools for discovery. *Chem. Rev.* **113**, 4633–4679 (2013).

197. D. Garrido Ruiz, A. Sandoval-Perez, A. V. Rangarajan, E. L. Gunderson, M. P. Jacobson, Cysteine oxidation in proteins: structure, biophysics, and simulation. *Biochemistry*. **61**, 2165–2176 (2022).

198. S. E. Leonard, K. S. Carroll, Chemical "omics" approaches for understanding protein cysteine oxidation in biology. *Curr. Opin. Chem. Biol.* **15**, 88–102 (2011).

199. P. Eaton, Protein thiol oxidation in health and disease: Techniques for measuring disulfides and related modifications in complex protein mixtures. *Free Radic. Biol. Med.* **40**, 1889–1899 (2006).

200. S. Stöcker, K. Van Laer, A. Mijuskovic, T. P. Dick, The conundrum of hydrogen peroxide signaling and the emerging role of peroxiredoxins as redox relay hubs. *Antioxid. Redox Signal.* **28**, 558–573 (2018).

201. Z. A. Wood, L. B. Poole, P. A. Karplus, Peroxiredoxin evolution and the regulation of hydrogen peroxide signaling. *Science.* **300**, 650–653 (2003).

202. H. A. Woo, S. H. Yim, D. H. Shin, D. Kang, D.-Y. Yu, S. G. Rhee, Inactivation of peroxiredoxin I by phosphorylation allows localized H(2)O(2) accumulation for cell signaling. *Cell.* **140**, 517–528 (2010).

203. W. S. Shahin, J. F. Engelhardt, Isolation of redox-active endosomes (redoxosomes) and assessment of NOX activity. *Methods Mol. Biol.* **1982**, 461–472 (2019).

204. M. Daugaard, R. Nitsch, B. Razaghi, L. McDonald, A. Jarrar, S. Torrino, S. Castillo-Lluva, B. Rotblat, L. Li, A. Malliri, E. Lemichez, A. Mettouchi, J. N. Berman, J. M. Penninger, P. H. Sorensen, Hace1 controls ROS generation of vertebrate Rac1-dependent NADPH oxidase complexes. *Nat. Commun.* **4**, 2180 (2013).

205. Y. Liu, C. Collins, W. B. Kiosses, A. M. Murray, M. Joshi, T. R. Shepherd, E. J. Fuentes, E. Tzima, A novel pathway spatiotemporally activates Rac1 and redox signaling in response to fluid shear stress. *J. Cell Biol.* **201**, 863–873 (2013).

206. Y. Fujikawa, L. P. Roma, M. C. Sobotta, A. J. Rose, M. B. Diaz, G. Locatelli, M. O. Breckwoldt, T. Misgeld, M. Kerschensteiner, S. Herzig, K. Müller-Decker, T. P. Dick, Mouse redox histology using genetically encoded probes. *Sci. Signal.* **9**, rs1 (2016).

207. S. C. Albrecht, A. G. Barata, J. Grosshans, A. A. Teleman, T. P. Dick, In vivo mapping of hydrogen peroxide and oxidized glutathione reveals chemical and regional specificity of redox homeostasis. *Cell Metab.* **14**, 819–829 (2011).

208. H. Chen, X.-N. Tan, S. Hu, R.-Q. Liu, L.-H. Peng, Y.-M. Li, P. Wu, Molecular mechanisms of chondrocyte proliferation and differentiation. *Front. cell Dev. Biol.* **9**, 664168 (2021).

209. G. Yang, L. Zhu, N. Hou, Y. Lan, X.-M. Wu, B. Zhou, Y. Teng, X. Yang, Osteogenic fate of hypertrophic chondrocytes. *Cell Res.* **24**, 1266–1269 (2014).

210. K. Y. Tsang, D. Chan, K. S. E. Cheah, Fate of growth plate hypertrophic chondrocytes: death or lineage extension? *Dev. Growth Differ.* **57**, 179–192 (2015).

211. S. Ashraf, B.-H. Cha, J.-S. Kim, J. Ahn, I. Han, H. Park, S.-H. Lee, Regulation of senescence associated signaling mechanisms in chondrocytes for cartilage tissue regeneration. *Osteoarthr. Cartil.* **24**, 196–205 (2016).

212. R. F. Loeser, J. A. Collins, B. O. Diekman, Ageing and the pathogenesis of osteoarthritis. *Nat. Rev. Rheumatol.* **12**, 412–420 (2016).

213. P. R. Coryell, B. O. Diekman, R. F. Loeser, Mechanisms and therapeutic implications of cellular senescence in osteoarthritis. *Nat. Rev. Rheumatol.* **17**, 47–57 (2021).

214. Z. Cang, Q. Nie, Inferring spatial and signaling relationships between cells from single cell transcriptomic data. *Nat. Commun.* **11**, 2084 (2020).

215. S. K. Longo, M. G. Guo, A. L. Ji, P. A. Khavari, Integrating single-cell and spatial transcriptomics to elucidate intercellular tissue dynamics. *Nat. Rev. Genet.* **22**, 627–644 (2021).

216. A. Rao, D. Barkley, G. S. França, I. Yanai, Exploring tissue architecture using spatial transcriptomics. *Nature*. **596**, 211–220 (2021).

217. E. Armingol, A. Officer, O. Harismendy, N. E. Lewis, Deciphering cell-cell interactions and communication from gene expression. *Nat. Rev. Genet.* **22**, 71–88 (2021).

218. R. J. Slack, S. J. F. Macdonald, J. A. Roper, R. G. Jenkins, R. J. D. Hatley, Emerging therapeutic opportunities for integrin inhibitors. *Nat. Rev. Drug Discov.* **21**, 60–78 (2022).

219. X. Pang, X. He, Z. Qiu, H. Zhang, R. Xie, Z. Liu, Y. Gu, N. Zhao, Q. Xiang, Y. Cui, Targeting integrin pathways: mechanisms and advances in therapy. *Signal Transduct. Target. Ther.* **8**, 1 (2023).

220. K. Ley, J. Rivera-Nieves, W. J. Sandborn, S. Shattil, Integrin-based therapeutics: biological basis, clinical use and new drugs. *Nat. Rev. Drug Discov.* **15**, 173–183 (2016).

221. D. Cox, M. Brennan, N. Moran, Integrins as therapeutic targets: lessons and opportunities. *Nat. Rev. Drug Discov.* **9**, 804–820 (2010).

222. M. N. Martinez, M. G. Papich, G. L. Drusano, Dosing regimen matters: the importance of early intervention and rapid attainment of the pharmacokinetic/pharmacodynamic target. *Antimicrob. Agents Chemother.* **56**, 2795–2805 (2012).